COMPARISON OF THERMODYNAMIC
EQUILIBRIUM AND NON-EQUILIBRIUM
REPRESENTATIONS OF MATERIALS

THESIS

Michael J. Vanderhyde, CAPT, USAF

AFIT/GAE/ENY/07-M25

DEPARTMENT OF THE AIR FORCE
AIR UNIVERSITY

AIR FORCE INSTITUTE OF TECHNOLOGY

Wright-Patterson Air Force Base, Ohio

AFIT/GAE/ENY/07-M25

Comparison of Thermodynamic Equilibrium and Non-Equilibrium Representations of Materials

THESIS

Presented to the Faculty

Department of Aeronautics and Astronautics

Graduate School of Engineering and Management

Air Force Institute of Technology

Air University

Air Education and Training Command

In Partial Fulfillment of the Requirements for the

Degree of Master of Science in Aeronautical Engineering

Michael J. Vanderhyde, BS

CAPT, USAF

22 March 2007

COMPARISON OF THERMODYNAMIC
EQUILIBRIUM AND NON-EQUILIBRIUM
REPRESENTATIONS OF MATERIALS

Michael J. Vanderhyde, BS

CAPT, USAF

Approved:

/signed/	22 Mar 2005
Dr. Anthony N. Palazotto (Chairman)	date
/signed/	22 Mar 2005
Dr. William P. Baker (Member)	date
/signed/	22 Mar 2005
Dr. Robert A. Brockman (Member)	date
/signed/	22 Mar 2005
Dr. Theodore Nicholas (Member)	date

AFIT/GAE/ENY/07-M25

Abstract

Hydrocodes are valuable tools in the modeling of shock wave propagation through solids due to high speed impact phenomena. To model high speed impacts, hydrocodes use the conservation equations of mass, momentum and energy, constitutive equations to model the materials response and equations of state (EOS). CTH is a hydrocode built with the ability to use multiple EOSs, including the semi-emperical Mie-Gruneisen EOS and tabular Sesame EOS. Modeling high speed impacts necessitates modeling the non-equilibrium thermodynamic states caused by these impacts. A discussion of the non-equilibrium thermodynamics that may be applied to the region directly behind a shock wave is presented, including details of recent attempts to model non-equilibrium impact phenomena in solids. Also, in order to better determine the applicability of the Mie-Gruneisen EOS and the Sesame EOS in situations that include non-equilibrium thermodynamics, the high speed, uniaxial impacts between two iron bars are modeled in CTH. These impacts are modeled using the Mie-Gruneisen EOS, Sesame EOS and a two state EOS called PTRAN. The results generated using these different EOS are then compared to experimental data to determine how well the different EOS model the thermodynamic non-equilibrium physics of the high speed impacts. The differences between the Mie-Gruneisen EOS and the Sesame EOS are established. A finite volume uniaxial hydrocode is validated. Finally, CTH is shown to be able to model some irreversibilities occurring in impact phenomena.

Acknowledgements

Michael J. Vanderhyde

Table of Contents

List of Figures

ix

Comparison of Thermodynamic Equilibrium and Non-Equilibrium Representations of Materials

I. Introduction

1.1 Introduction

A hydrocode is a computer code that is able to model the waves caused by high speed impacts as they travel through solid materials. As Zukas [43] explains in his hydrocode book, early hydrocodes were given the name because they relied on the hydrodynamic assumption. The hydrodynamic assumption states that if the pressures generated in a high speed impact are much greater than the strength of the materials involved in the impact, then the strength may be ignored and the materials may be modeled as fluids. Modern hydrocodes are able to account for the strength of the materials by using constitutive equations in these impact scenarios, however the name hydrocode has stuck.

Today, hydrocodes are used to model an array of different hypervelocity impact scenarios. These scenarios may include debris striking a space vessel, or flying debris from an explosion striking a hardened target. Cinnamon [9], Szmerekovsky [35] and Laird [24] used the Sandia National Labortories hydrocode CTH to model the gouging caused by impact between the shoes of the sleds used at the Holloman High Speed Test Track (HHSTT) and the railing of the track itself.

Hydrocodes use three different types of equations to model impacts. These time dependent equations include conservation equations, the previously mentioned constitutive equations and equations of state [43].

According to continuum theory, the conservation equations include the conservation of mass, momentum and energy. These equations give us the variables of

velocity (v), density (ρ), pressure (P), and internal energy (e). Temperature (T), may also be determined using these equations, but is not necessary. In isothermal systems the temperature and internal energy of the system remain constant. Then the conservation equations and an isothermal relationship between two thermodynamic variables, excluding temperature and internal energy may act as a complete system of equations and thus are the only equations necessary to solve for desired material properties [30].

The previously mentioned impact conditions are not isothermal, requiring an additional equation to close the system of equations, hence the need for an equation of state (EOS). EOS act as a bridge between the macroscopic continuum mechanics represented by the conservation equations and the microscopic thermodynamics of the system [43]. Also, the extremely high pressures generated in the aforementioned impact scenarios cause the EOS used to dominate the answers generated by hydrocodes. This necessitates that the EOS accurately model the thermodynamics.

Unlike in the study of gas dynamics, where a general EOS can be applied to a wide range of gasses, the EOS of solids tend to be specific to a material or material type (metals, ceramics, etc...). Also, depending on the origin of the EOS (empirical, semi-empirical, theoretical, etc...), said EOS may have a limited range of applicability [43]. For example, empirical based equations of state may mean nothing when used in conditions far from the experiments used to generate them. The applicability of a theoretical EOS will depend on the thermodynamics used to derive it. In the area immediately behind a shock wave, for example, conditions are changing at an extremely high rate, so there exists a state of non-equilibrium necessitating the use of non-equilibrium thermodynamics (NET). Conversely, in regions where the conditions are not changing as fast, a state of local equilibrium may be assumed allowing for the use of equilibrium thermodynamics [26].

Equilibrium based thermodynamics were used in the generation of the popular Mie-Gruneisen EOS and in the generation of the tabular EOS such as the Sesame EOS [22].

In the 1930's work began in Classical Irreversible Thermodynamics (CIT), which used thermodynamic fluxes in addition to the classic thermodynamic state variables in the description of a system in an assumed local equilibrium state. The assumption of a local equilibrium state allows CIT to extend beyond the range of equilibrium thermodynamics, but still requires a system to remain "near" an equilibrium state [26].

In the 1960's another form of irreversible thermodynamics referred to as rational dynamics (RT) was introduced. RT assumes materials have memories and that complimentary variables (entropy, internal energy, heat flux, etc...) are functions of the histories of the independent state variables [27].

Two branches of modern irreversible thermodynamics are referred to as extended irreversible thermodynamics (EIT) and internal variable theory (IVT). EIT uses macroscopic thermodynamic fluxes as non-equilibrium state variables to complement the use of classical equilibrium state variables in the description of a local non-equilibrium state [18]. IVT identifies additional variables that describe the microscopic effects of a system.

Today researchers such as Lu and Hanagud [26] [27]are able to use a mixture of irreversible thermodynamic theories to model the non-equilibrium thermodynamics of a solid material's response to impact loading.

1.2   Procedure

There are several portions to the numerical investigation in this investigation. These parts include the comparison of the results generated using the Mie-Gruneisen and PTRAN EOS to those produced using the Sesame EOS, the validation of the finite volume Eulerian hydrocode and a comparison of the results generated using CTH to

those generated using the Non-Equilibrium Thermodynamic hydrocode developed by Lu and Hanagud.

Each portion of the numerical investigation composes its own chapter to avoid confusion. Each chapter consists of a description of the numerical procedure followed immediately by the results generated. Chapter 2 discusses the theories behind the modeling of equilibrium and non-equilibrium thermodynamic impact systems. Chapter 3 provides the procedures and results from comparing the Mie-Gruneisen and PTRAN EOS to the Sesame EOS using uniaxial impacts of aluminum and iron, a reversibility test to determine if the Sesame EOS can model irreversibilites in the regions of a phase change, and a recreation of the flyer plate experiments performed by Cinnamon [9] using 1080 steel. Chapter 4 explains how the finite volume hydrocode is validated comparing the results generated by the finite volume hydrocode to those generated by CTH. Chapter 5 compares the results generated by CTH to those produced by Lu and Hanagud's non-equilibrium hydrocode. Finally, Chapter 6 presents any conclusions made and provides recommendations for the further study of non-equilibrium thermodynamics and the development of the finite volume Eulerian hydrocode.

II. Theory

This chapter discusses the basic concepts behind the numerical modeling of dynamic impact phenomena. A general overview of the numerics behind the hydrocodes is provided along with the basic form of the equations used in these hydrocodes. A Thermodynamics review is then presented followed by the development of equations of state. This will be followed by an introduction to current methods used to model the non-equilibrium thermodynamics in impact scenarios. All the numeric simulations in this investigation are performed using a uniaxial strain solver in CTH, therefore all the equations in this theory section are written in uniaxial form where applicable.

2.1   Numerical Modeling

Two programs, the hydrocode CTH and a finite volume code written in Fortran 90, are used to compare the abilities of different equations of state to model high speed impact phenomena. A brief description of how each program works is presented here to familiarize the reader with these two programs.

2.1.1   Numeric Terminology. Two terms used while analyzing a code's ability to numerically model discontinuities such as a shock wave (defined in Section 2.3) are dissipation and dispersion. Dissipation refers to the process of taking a discontinuity and spreading it out over several numerical grid cell widths. Dispersion refers to oscillations in the numerical solution caused by discontinuities, and is often located around the discontinuity itself. Figure 2.1 illustrates the difference between the types of numerical errors compared to an "ideal" representation of a numerical discontinuity [36].

a. Dissipation   b. Discontinuity   c. Dispersion
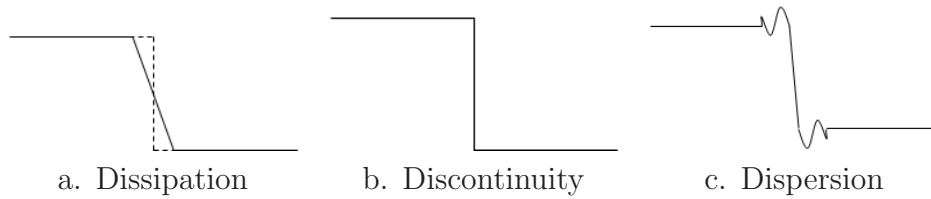
Figure 2.1:   Illustration of Dissipation and Dispersion Error

2.1.2 CTH. Hertel et al. [15] provide a concise explanation of how CTH works. CTH is an Eulerian based hydrocode that uses a two step process to solve the conservation equations. The first step is the Lagrangian step, in which the mesh is deformed and the governing equations are integrated through time. Mass, momentum, energy and volume are conserved during the Lagrangian step. Mass is conserved, due to the movement of the mesh, which stops all matter from moving across the cell boundaries. The rest of the conservation equations are replaced by explicit finite volume forms of the original integral equations.

The Lagrangian step is followed by a remap step in which, the distorted mesh is re-mapped onto the original Eulerian mesh. During the remap step mass, momentum, energy and volume are transported from the deformed mesh to the original mesh using advection algorithms [6]. To do this, CTH first calculates the flux of the volume between the old and new cells. Then, an interface tracking algorithm decides which materials from the old cells get moved with the volume flux. The mass and energy of materials being moved are then transferred from the old cells to the new ones. Finally information from the interface tracker is used to move the momentum and kinetic energy of the cells [15].

Benson [6] provides a good illustration of what is happening numerically when the operator split is being used. When modeling a continuum, the conservation equations equations take the form:

$$\frac{\partial \phi}{\partial t} + c\frac{\partial \phi}{\partial x} = f \tag{2.1}$$

This equation is referred to as the linear advection equation, where ϕ is the field variable, c is the constant flow velocity and f is a source term. The operator split divides this equation into two parts. The Langrangian equation, which is solved by moving the mesh is:

$$\frac{\partial \phi}{\partial t} = f \tag{2.2}$$

and the Eulerian equation solved during the remap step has the form:

$$\frac{\partial \phi}{\partial t} + c\frac{\partial \phi}{\partial x} = 0 \qquad (2.3)$$

In order to control the discontinuity caused by shock waves in the Lagrangian time step, a three term "artificial viscosity" is utilized. Artificial viscosities are numerical tools, added to the pressures, that smear the discontinuities in continuum based codes over several mesh widths, allowing hydrocodes to handle any discontinuities that may arise. Though the artificial viscosity distorts the area around discontinuities, the solution is only affected in the area of the shock front and the accuracy of the calculations are preserved. [43]

In CTH, a vector subset of the full viscosity tensor including linear and quadratic terms is used. In three dimensions, the vector includes xx, yy and zz terms. A third linear term controling a singular point during the update of the stress deviators along the axis of symmetry when the two-dimensional cylindrical geometry is also used [15].

2.1.3   The Vanderhyde Finite Volume Code (VFVC).   A finite volume, Eulerian hydrocode that utilizes the Mie-Gruneisen EOS is also used to model uniaxial impacts. This code, refered to as the Vanderhyde Finite Volume Code (VFVC), was adopted from a computational fluid dynamics (CFD) shock tube code. It solves the partial differential equation, shown in finite difference form, of [38]:

$$\frac{\partial Q_{vec}}{\partial t} + \frac{\partial F_{vec}}{\partial x} = f(Q_{vec}) \qquad (2.4)$$

where Q_{vec} is the vector of conserved variables, F_{vec} is the flux vector and $f(Q_{vec})$ is a source term vector.

For clarification, a finite volume solver applies the conservation equations to a fixed region of space, called a control volume [36]. In finite volume form this is written
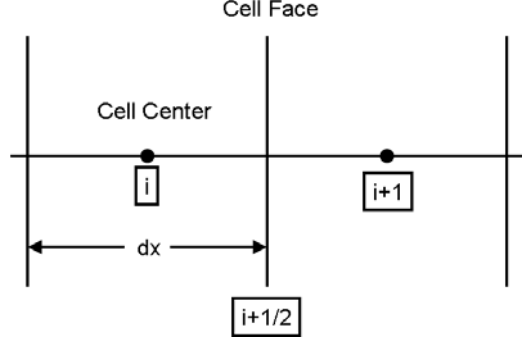
Figure 2.2:   One Dimensional Grid

as:

$$\int_{Vol} \frac{\partial Q_{vec}}{\partial t}\, dVol \;+\; \int_{A} F_{vec} \cdot dA \;=\; \int_{Vol} f(Q_{vec}) \tag{2.5}$$

where A is referred to as an area vector and Vol is the volume of the cell, which in one dimension is the width of the cell, or dx. Upon integrating Equation 2.5 becomes:

$$\frac{\partial Q_{vec}}{\partial t} \;=\; \frac{1}{Vol} \sum F_{vec} \cdot dA \;+\; f(Q_{vec}) \tag{2.6}$$

The flux vector numerically represents the flux of the conservation variables (mass, momentum, energy, etc) at the boundary of the control volume, and is used in the spatial integration of the conservation equations. Finally, the source term refers to the non-hyperbolic portion (the right side) of Equations (2.4)and (2.5). An example of a one dimensional grid is shown in Figure 2.2.

The VFVC uses a flux routine to solve for the flux variables moving through the mesh and to handle any discontinuities that may present themselves. $F_i - F_{i+1}$ represents the flux through the faces of individual cells where i represents the node numbers of the cell. The flux routine used in the VFVC is referred to as the Lax-Friedrichs flux routine [38]. Equation (2.7) gives the form of the Lax-Friecrichs flux. Lax-Friedrichs is a first order approximation of the flux vector values at the cell face and works by taking the average values of the flux vector at the cell boundaries and adds a dissipation term, $\alpha_{i+\frac{1}{2}}(q(x_i) - q(x_{i+1}))$, to the average, allowing the code to handle discontinuities.

$$F_{i+\frac{1}{2}} = \frac{1}{2}\left[f(q(x_i)) + f(q(x_{i+1})) + \alpha_{i+\frac{1}{2}}(q(x_i) - q(x_{i+1}))\right] \qquad (2.7)$$

A second order MUSCL Scheme [36] is used to remove excess dissipation introduced by the Lax-Friedrich flux routine and provides second order spatial accuracy with the use of numerical limiters that remove non-physical dispersion error.

After the flux routines solve for the flux vector values, the flux vector values are inserted into the right side of Equation (2.6), also called the right hand vector, $R(Q_{vec})$, which becomes:

$$R(Q_{vec}) = \frac{F_i - F_{i+1}}{dx} + D(Q_{vec}) \qquad (2.8)$$

where dx is the cell width and D is the source term operator [38].

Explicit time integration schemes are used to integrate the following PDE with respect to time. [38]:

$$\frac{\partial Q_{vec}}{\partial t} = R(Q_{vec}) \qquad (2.9)$$

Three different time integration schemes are used to integrate through time: a first order Euler Explicit Scheme [36], a third order Runge-Kutta scheme [38] and a fourth order Runge-Kutta scheme [36]. The Euler Explicit Scheme used is given in Equation (2.10), while the other integration schemes are contained in Appendix 1. The Euler Explicit method uses first order forward difference schemes in space (i) and time (n), to integrate through time. A more detailed development of the uniaxial code is available in Appendix 1.

$$\frac{Q_i^{n+1} - Q_i^n}{\Delta t} + c\frac{Q_{i+1}^n - Q_i^n}{\Delta x} = 0 \qquad (2.10)$$

2.2 Equations of Motion

In the numerical modeling of a dynamic system several classes of the equations of motion equations are needed. These equations of motion include the conservation

equations, an equation of state (EOS) and when modeling systems where the strength of materials needs to be taken into account, a set of constitutive equations.

2.2.1   Conservation Equations.   The conservation equations typically are used to solve for the values of the mass, momentum and energy. Since all the numerical simulations being considered are uniaxial, the conservation equations below are written one dimensionally in the x direction. CTH and the FVC are both Eulerian based hydrocodes, meaning they track matter as it proceeds through a fixed mesh. Eulerian hydrocodes are typically used when the distortions caused by an event are very large, something pure Langrangian codes have trouble modeling because cell volumes may approach zero, or the cells become inverted producing negative volumes [43]. Since both hydrocodes are Eulerian, the conservation equations are presented here in Eulerian form.

2.2.1.1   Conservation of Mass.   Simply stated the conservation of mass dictates that mass can neither be created or destroyed as a system undergoes changes. [1]

The mathematical form of the conservation of mass is written as [37]:

$$\frac{\partial \rho}{\partial t} + \frac{\partial (\rho v)}{\partial x} = 0 \qquad (2.11)$$

The first term of the conservation of mass accounts for compressibility. Compressibility effects refer to a changes, over time, in the density of a material at a given point in space, or a change of the entire volume of a system. The second term accounts for the change in the amount of material flowing through a control volume with respect to spatial position.

2.2.1.2   Conservation of Momentum.   Conservation of momentum can be stated as: the time rate of change of momentum of a body equals the net force exerted on said body. This is also Newton's second law stating that force exerted on a

10

body is equal to the product of the mass of the body and the amount of acceleration the body is undergoing, or $F = ma$ [1].

The Eulerian form of the conservation of momentum is written as [37]:

$$\rho F = \frac{\partial(\rho v)}{\partial t} + \frac{\partial(\rho v^2 - \sigma)}{\partial x} \qquad (2.12)$$

where F is the force per unit mass acting on the system and σ represents the stress being applied to the system. In the conservation of momentum, the ρF term represents the entire force acting on the system. The first component of the right hand side of Equation (2.12), accounts for changes in the amount of mass flowing through a control volume over time. The second term accounts for changes of the total momentum inside a control volume, with respect to spatial position, by taking the difference in net flow of momentum, ρv^2, and the total stress, σ, applied to the system.

2.2.1.3 *Conservation of Energy.*   The conservation of energy dictates that energy can neither be created or destroyed; it can only change form. The conservation of energy incorporates the thermodynamics of a system with the systems motion, by relating a system's kinetic energy with other forms of energy.

The Eulerian form of the conservation of energy is [37]:

$$\rho(q + Fv) = \frac{\partial \rho \left(e + \frac{1}{2}v^2\right)}{\partial t} + \frac{\partial\left(v\rho\left[e + \frac{1}{2}v^2\right] - \sigma v\right)}{\partial x} \qquad (2.13)$$

where q represents heat diffusion. In English, the conservation of energy states the total work done, $\rho(q + Fv)$, equals the time rate of change of energy, $\rho\left(e + \frac{1}{2}v^2\right)$, plus the flow of energy across a specified area, $v\rho\left[e + \frac{1}{2}v^2\right]$, minus the materials resistance to the energy flow, σv, in that area [1].

2.2.2 *Constitutive Equations.*   When modeling impact dynamics, the responses of the materials need to be taken into consideration. The material response is often represented in two components, the hydrodynamic response and the deviatoric

11

response. The hydrodynamic stress makes up the diagonal of the stress tensor, is related to pressure and is calculated from the EOS [43].

$$\sigma_{hydro} = -P\delta_{ij} \qquad (2.14)$$

The deviatoric or shear stress of the material is designated as, σ_{ij}^D. The total material response is the sum of the hydrodynamic and deviatoric stresses. [38]

$$\sigma_{ij} = \sigma_{ij}^D - P\delta_{ij} \qquad (2.15)$$

In high speed phenomena, hydrostatic stresses are typically orders of magnitude greater than the deviatoric stress. This justifies the hydrodynamic assumption discussed in the introduction. It also explains why the magnitude of stress produced by a very high speed impact is approximately equal to the pressures produced. Throughout this investigation, constitutive relationships are used to describe the material response in impacts. However, due to high magnitudes of pressure typically generated, this response is assumed negligible.

Two common constitutive equations used by CTH are the Johnson-Cook (JC) and Zerilli-Armstrong (ZA) models. In this investigation the availability of predefined material coefficients in CTH dictates which constitutive relationship is used to model different materials.

2.2.2.1 Johnson-Cook Constitutive Equations. The Johnson-Cook constitutive model is an empirical based relationship that takes the form:

$$\sigma = (A + B\epsilon^n)(1 + C\,ln\dot{\epsilon})(1 - T^{*m}) \qquad (2.16)$$

where ϵ represents strain, $\dot{\epsilon}$ represents strain rate, and A,B,n,C and m are experimentally determined material specific constants. The value of T^* is found by the ratio $(T - T_{room})/(T_{melt} - T_{room})$ where T is the absolute temperature of the ma-

terial. The material constants are determined experimentally. The first expression in this equation represents the stress as a function of strain. The second and third expressions represent strain rate and temperature effects, respectively [17].

2.2.2.2 Zerilli-Armstrong Constitutive Equations. The Zerilli-Armstrong constitutive relationship was developed for the purpose of improving the numerical results generated using the Johnson-Cook relationship. Zerilli-Armstrong model has a strong empirical basis, but also takes into account effects caused by the microscopic properties of the materials such as grain size and lattice structure. The dependence on the type of lattice structure a material is made of requires different forms of the Zerilli-Armstrong relationships [41]. The face centered cubic (fcc) form of the Zerilli-Armstong relationship is:

$$\sigma = \Delta\sigma'_G + c_2\epsilon^{1/2} * e^{(-c_3 T + c_4 T ln\dot{\epsilon})} + kl^{-\frac{1}{2}} \tag{2.17}$$

The body centered cubic (bcc) form of the Zerilli-Armstrong model is:

$$\sigma = \Delta\sigma'_G + c_1 e^{(-c_3 T + c_4 T ln\dot{\epsilon})} + c_5\epsilon^n + kl^{-\frac{1}{2}} \tag{2.18}$$

For both the bcc and fcc equations $\Delta\sigma'_G$ represents an additional component of stress, k is the microstructural stress intensity, $l^{\frac{-1}{2}}$ is the inverse of the square root of the average grain diameter and c_1, c_2, c_3, c_4, c_5 and n are experimentally determined values [41].

2.2.2.3 Material Values. In this investigation, the material response of aluminum will be described using the Johnson-Cook relationship, while iron's responses will be described using the Zerilli-Armstrong constitutive relationship. CTH's internal coefficients are used to describe both materials, however these coefficients are not available. Publicly available material properties are given here for use in pro-

grams needing these input parameters. The Johnson-Cook coefficients are given in Table 2.1 [40]. The Zerilli-Armstrong coefficients are given in Table 2.2 [41].

Table 2.1: Johnson-Cook Coefficients of 99.5% Aluminum

Coefficient	Value	Units
A	265.0	MPa
B	426.0	MPa
C	0.015	
m	1	
n	0.34	

Table 2.2: Zerilli-Armstrong Coefficients of Iron

Coefficient	Value	Units
$\Delta\sigma'_G$	0.0	MPa
c_1	1033	MPa
c_2	na	MPa
c_3	0.00698	k^{-1}
c_4	0.000415	k^{-1}
c_5	266.0	MPa
n	0.284	
k	22.0	MPa $mm^{\frac{1}{2}}$
$l^{\frac{1}{2}}$	3.0	$mm^{\frac{-1}{2}}$

2.3 Wave Propagation in Solids

This work depends heavily on the propagation of waves through solids, thus a brief description of wave propagation through solids is presented.

When an object is struck by another, a compression or stress wave is produced. The type of stress wave depends on the velocity of the impactor and on the strength of the material being struck. Three different wave scenarios are possible. If the amount of strain produced due to the applied stress is below a material value called the Hugoniot Elastic Limit (HEL), a single elastic wave will propagate through the material. If the amount of strain produced by the stress is above the HEL an elastic "precursor" will precede at a velocity of c_E, which is faster than the wave speed of the plastic wave, c_P. Figure 2.3 [43] shows this second scenario. If a high enough
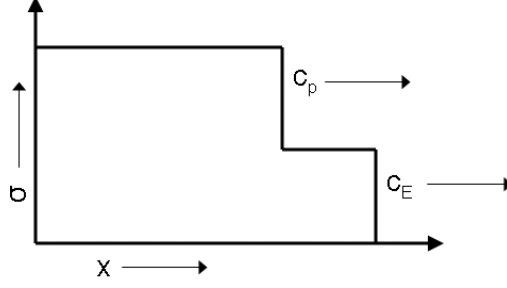
Figure 2.3:   Stress Wave Profile

value of stress is generated by the impact, the plastic wave will overtake the elastic wave and become a shockwave. At this amount of stress, the material exhibits plastic behavior and displays fluid like characteristics. The material particles behind a stress wave move with a velocity particle velocity, v_i [43].

When a propagating compression wave reaches a boundary, how it reacts is a property of the boundary condition. There are two conditions that must be met at the boundary: 1) The forces on both sides of the boundary must be equal, and 2) the particle velocities at the boundary must be continuous. Figure 2.4 illustrates these two conditions. The first condition leads to [43]:

$$A_1(\sigma_I + \sigma_R) = A_2\sigma_T \tag{2.19}$$

where A represents the cross-sectional area of the objects on both sides of the boundary, and the subscripts T and R, represent transmitted and reflected waves, respectively. The second condition states:

$$v_I - v_R = v_T \tag{2.20}$$

Assuming that $\sigma = \rho c v$ [43], the values of the transmitted and reflected stresses can be shown to be:

$$\sigma_T = \sigma_I \frac{2A_1\rho_2 c_2}{A_1\rho_1 c_1 + A_2\rho_2 c_2} \tag{2.21}$$

15
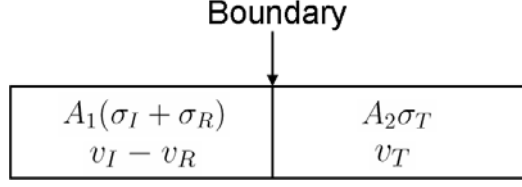
Figure 2.4:   Boundary Conditions Between Two Materials
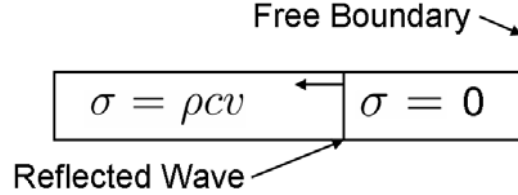
Figure 2.5:   Reflection of a Stress Wave

and

$$\sigma_R = \sigma_I \frac{A_2\rho_2 c_2 - A_1\rho_1 c_1}{A_1\rho_1 c_1 + A_2\rho_2 c_2} \qquad (2.22)$$

At a free surface, $\frac{A_2}{A_1}$ approaches 0 and $\rho_2 c_2 = 0$ so there is no transmitted wave and $\sigma_R = -\sigma_I$. This means that a compression wave reflects as a tensile or rarefaction wave (and vice versa), and that the particle velocity is doubled at the free surface [43]. Figure 2.5 shows how this wave reflection affects the stress due to the compression wave, and is included because free boundaries are used in this investigation.

At a fixed surface, $\frac{A_2}{A_1}$ approaches infinity, $\sigma_R = \sigma_I$ and $\sigma_T = 0$. This means that a compression wave reflects as a compression wave, and that the particle velocity is zero at the free surface [43].

If $A_2\rho_2 c_2 = A_1\rho_1 c_1$ then $\sigma_R = 0$ (there is no reflected wave) and the value of the transmitted stress wave is:

$$\sigma_T = \sigma_I \sqrt{\frac{\mathcal{E}_2\rho_2}{\mathcal{E}_1\rho_1}} \qquad (2.23)$$

where $\mathcal{E}$ is the modulus of elasticity [43].

2.4 Equilibrium and Non-Equilibrium Thermodynamics

A good understanding of thermodynamics in necessary to follow the development the EOS used in this investigation. In this section, the laws of thermodynamics are presented. Key assumptions made in the use of equilibrium and non-equilibrium thermodynamics are also presented with an explanation of what each type of thermodynamics each. An introduction to non-equilibrium thermodynamics is also presented here.

2.4.1 The Laws of Thermodynamics. Anderson [1] simply defines thermodynamics as "the science of energy (and entropy)." The users of thermodynamics use it to approximate the thermodynamic properties of systems, in other words, the known thermodynamic properties of a system are used to calculate its unknown properties at equilibrium states. [13]

The thermodynamic state of a system may be described by a set of physical values called state variables. It is important to note that the values of these state variables of a system are independent of how the system arrived at a particular state. When one of the state variables changes, the thermodynamic state also changes [34].

The first law of thermodynamics states: "Energy cannot be created or destroyed, only converted from one form to another." [13] Mathematically this law becomes [39]:

$$de = dQ - P * dV \qquad (2.24)$$

Where de is the total change in internal energy, dQ is the amount of heat the system receives from its surroundings and P and V are the pressure and specific volume of the system. If a system is in a state of equilibrium thermodynamics P and e are state functions that are related to the state variables, specific volume, V, and absolute temperature T using equations of the form [39]:

$$P = P(V, T) \qquad (2.25)$$

and

$$e = e(V, T) \tag{2.26}$$

If the system is in a state of non-equilibrium, additional state variables that do not appear in the equations of conservation are needed to model the system. In a state of non-equilibrium thermodynamics, Equations (2.4.1) and (2.4.1) become [39]:

$$P = P(V, T, N_1.....N_n) \tag{2.27}$$

and

$$e = e(V, T, N_1.....N_n) \tag{2.28}$$

where N_i represent the additional state variables needed to describe the system. Additional equations are also needed to solve for these variables [39]. There are several irreversible thermodynamic theories used to identify and define these additional variables. Two of these theories, Internal Variable Theory and Extended Irreversible Thermodynamics are described in Section 2.4.3.

The second law of thermodynamics deals with the state function of entropy. Gasser and Richards, among others, define entropy as "a measure of the chaos or disorder of the system" [13], in other words it quantifies the amount of unknown information in a thermodynamic system. The statement of the second law varies between equilibrium thermodynamics and non-equilibrium thermodynamics. In equilibrium thermodynamics, the second law is stated in two parts. The first part applies to reversible processes, while the second part may be applied to irreversible process.

In equilibrium thermodynamics, when a reversible process affects a closed system, the change in entropy is given by [39]:

$$S_B - S_A = \int_A^B \left(\frac{dQ}{T} \right)_{rev} \tag{2.29}$$

and when the same system is affected by a irreversible process the change in entropy is given by [39]:

$$S_B - S_A > \int_A^B \left(\frac{dQ}{T}\right)_{irrev} \tag{2.30}$$

The first part explains how to calculate the difference in entropy caused by a reversible process changing equilibrium state A into an equilibrium state B. The second part mandates that in an irreversible process, the value of the integral, $\int \frac{dQ}{T}$, is less than the change of entropy as calculated for a reversible process.

In non-equilibrium thermodynamics, the first part of the second law states that the change in entropy can be divided into two parts, shown in Equation (2.31) [39]:

$$dS = d_e S + d_i S \tag{2.31}$$

where $d_s E$ is entropy lost from the system to its surroundings and $d_i S$ is the entropy produced by the irreversible process within the system.

The second law also states, for a non-equilibrium system, the amount of entropy produced is never less than zero, if the entropy produced equals zero the process affecting the system is reversible, and if the amount of entropy produced is greater than zero the process affecting the system is irreversible [39].

$$\begin{cases} d_i S &= 0 \quad (reversible\ process) \\ d_i S &> 0 \quad (irreversible\ process) \end{cases} \tag{2.32}$$

The discerning reader will notice the entropy produced in an irreversible, or non-equilibrium, process, is calculated using only equilibrium thermodynamics in Equation (2.30). This is possible because in equilibrium thermodynamics, the entropy production is found using the difference between two equilibrium states. In non-equilibrium thermodynamics, the entropy production is found at an instantaneous point in time.

19

The third part of the second law states that d_eS of a closed system affected by either a reversible or an irreversible process can be calculated with the relationship [39]:

$$d_eS = \frac{dQ}{T} \quad (closed\ system, any\ process) \tag{2.33}$$

The differential forms of the second law in Equations (2.31 and 2.33) indicate the system is in a state of non-equilibrium, opposed to the equilibrium form of the second law comparing two equilibrium end states. Also note, in non-equilibrium thermodynamics, the irreversible statement assumes that meaningful values of the temperatures and entropy exist and that their values can be explicitly solved for. This condition limits the applicability of the irreversible statement to certain problems [39].

The third law of thermodynamics states, "The entropy of any system in a state of stable equilibrium tends to a finite value as the absolute temperature tends to zero [34]." The third law indicates you don't need to know that absolute values of the entropy in a system at end states A and B, it is only the change in entropy between the end states that is important. The third law also reduces the amount of needed data necessary to calculate the thermodynamic properties of the system after it has undergone changes. Also, if the chemical composition of the system remains constant as the system undergoes a change, the third law allows for thermodynamic calculations when only the respective values of entropy above a reference state are known.

2.4.2 Equilibrium Thermodynamics. According to equilibrium thermodynamics when a system is in an equilibrium state, the state variables are mathematically related to each other through equations of state (EOS). An EOS consists of independent state variables and dependent state variables, or state functions. With an EOS it is only necessary to know the value of a few of the state variables in order to be able to describe the thermodynamic state of the system [34].

A static system can be considered to be in thermodynamic equilibrium when several criteria are met. These criteria consist of mechanical equilibrium, thermal equilibrium and chemical equilibrium. A state of mechanical equilibrium indicates there are no unbalanced forces, internally or externally, in the system. A state of thermal equilibrium indicates the whole system is at the same temperature matching the temperature of the environment. Finally, a state of chemical equilibrium indicates there are no spontaneous changes to the internal structure of the system [30]. A dynamic system may also be considered to be in a state of equilibrium if it proceeds slow enough the system consists of multiple stable equilibrium states. After a shockwave passes, the value of the thermodynamic variables will continue to change for a specified period of time in a process called relaxation. If the order of the time between the equilibrium states is greater than the order of the relaxation time the, process may be considered slow, allowing the use of equilibrium thermodynamics. When a process proceeds such that it cannot be considered as a set of equilibrium states of a system, it is considered to be a non-equilibrium process. These equilibrium states generally do not happen in nature, however the effort of considering all the complexities of non-equilibrium systems may not be worth the effort, justifying the use of equilibrium thermodynamics. [34]

According to the previous conditions for equilibrium, the region directly behind a shockwave, due to the relaxation times, cannot be considered to be in a state of equilibrium. In order to describe the thermodynamics conditions behind a shock wave, however, equilibrium based thermodynamics and some irreversible thermodynamic theories have introduced the assumption of a local equilibrium. The local equilibrium assumption allows state functions to be described in a "local" region using the same state variables necessary to describe an equilibrium state. Even though a state of local equilibrium is assumed, the overall system still produces entropy, the change in entropy of a system in local-equilibrium is described using the Gibbs equation for entropy production:

$$dS = \frac{1}{T}de + \frac{1}{T}PdV \qquad (2.34)$$

The terms on the right hand side of Equation (2.34) refer to the contributions of temperature and pressure to the production of entropy [18].

The thermodynamic state of a system can also be described using Statistical Mechanics, in which the behavior of behavior of many molecules and atoms are considered. The collective behavior of the microscopic particles are then averaged, producing statistical concepts of pressure, temperature, internal energy and entropy [34]. For example entropy is found by relating the distribution of the microscopic particles to the macroscopic thermodynamics using Boltzmann's relation. [39]:

$$S = k \ln \Omega \tag{2.35}$$

where k is Boltzman's constant and Ω is the number of ways to distribute the particles in a system [13]. Also, in statistical mechanics atoms are modeled as quantized oscillators, with each oscillator containing three directions of vibration and possessing a mean energy $\bar{\varepsilon}$ [29].

When a system is in either global equilibrium, meaning the entire system is in equilibrium, or local equilibrium, meaning only an isolated part of a system is in equilibrium, the frequencies atoms oscillate at, g_{eq}, are described by the Maxwell-Boltzman distribution function [18]:

$$g_{eq} = n \left(\frac{2\pi kT}{m} \right)^{\frac{3}{2}} e^{\left(\frac{-mC^2}{2kT} \right)} \tag{2.36}$$

where n is the number of atoms per unit volume, m is the mass of the atom and C is the relative velocity of the atom with respect to the mean velocity of the system [39].

2.4.3 *Non-Equilibrium Thermodynamics (NET).* If a system undergoes a change, and the rate of said change is relatively slow when compared to the time required for a system to relax to an equilibrium state, the applicability of the local equilibrium assumption is no longer valid and the system is considered to be in a state

of non-equilibrium. A shock wave traveling through a solid is an example of such a non-equilibrium process [18].

The study of non-equilibrium thermodynamics (NET) puts a great emphasis on the determination of the amount of entropy produced in a irreversible or non-equilibrium system. The second law introduced in equation 2.31, introduces entropy as a system variable and states entropy is produced when a system undergoes an irreversible or non-equilibrium process. This law can also be written in terms of equilibrium and non-equilibrium entropy [18]:

$$S_{eq,f} = S_{neq,i} + S_{prod} \tag{2.37}$$

where the subscripts i and f indicate the initial and final states respectively, and S_{prod} represents the entropy produced when the system goes from the initial to the final state.

In equilibrium thermodynamics entropy is considered a characteristic state function. This means it is able to describe all the conceivable thermodynamic information about a system, if the entropy is expressed using the system's extensive natural variables [19]. For example Callen [8] use Equation (2.34) and differentiate it to produce equations of state for temperature and pressure, $T^{-1}(e, V) = \frac{\partial S}{\partial e}$ and $T^{-1}P(e, V) = \frac{\partial S}{\partial V}$, respectively. In NET it is assumed that non-equilibrium entropy and temperature exist and that they have the potential to be useful in the description of systems in non-equilibrium.

As discussed in in Section 2.4.1 the determination of the entropy being produced differs between equilibrium and non-equilibrium thermodynamics. In equilibrium thermodynamics, the production of entropy in an irreversible process is calculated between two equilibrium states, as shown in Equation (2.30):

$$S_B - S_A > \int_A^B \left(\frac{dQ}{T} \right)_{irrev}$$

However, if any relaxation is occurring and the order of the relaxation time is equal to or greater than the order of the time between equilibrium states, Equation (2.30) will be unable to capture the relaxation process. When this is the case, the entropy production needs to be described instantaneously. A term capturing the non-equilibrium relaxation is also needed. Equation (2.31) shown here:

$$dS = d_eS + d_iS$$

accounts for both conditions necessary to solve for the amount of entropy production by being written in differential form, allowing an instantaneous description of the entropy generation, and including a non-equilibrium term accounting for the relaxation time.

Due to the local equilibrium assumption's lack of applicability, both classic thermodynamic state variables and non-equilibrium state variables are used to describe the irreversible processes of a system in NET. The nature of these extra variables depends on the system being studied. Theories of irreversible thermodynamics allow for the identification of these variables. Modern irreversible thermodynamics include, extended irreversible thermodynamics (EIT) and internal variable theory (IVT) [19].

2.4.3.1 Extended Irreversible Thermodynamics (EIT). EIT incorporates dissipative fluxes with the use of the classical state variables to describe the thermodynamics of a system. Dissipative fluxes refer to irreversible and dissipative process used to describe the interaction of a material with its surroundings [26]. For example Jou et al [18] [19] use the heat flux $\mathbf{q}$, bulk viscous pressure p^v and the deviatoric part of the viscous pressure tensor $\mathbf{P}_0^v$, with corresponding evolution equations, to describe fluid consisting of one component.

The heat flux refers to the flow of heat into and out of a system. The bulk viscosity pressure and the deviatoric part of the viscous pressure make up the viscous pressure tensor, $\mathbf{P}^v$, through the relationship, $\mathbf{P}^v = p^v I + \mathbf{P}_0^v$. In this relationship I

is identity tensor. The total pressure tensor, $\mathbf{P}$ is then composed of the pressure, P, and the viscous pressure tensor, $\mathbf{P}^v$, using the relationship, $\mathbf{P} = PI + \mathbf{P}^v$.

Using these evolution equations the linear generalized Gibbs equation for entropy production, in vector notation, becomes [19]:

$$dS = \Theta^{-1}de + \Theta^{-1}\pi dV - \frac{V\tau_1}{\lambda T^2}\mathbf{q} \cdot d\mathbf{q} - \frac{V\tau_0}{\zeta T}p^v dp^v - \frac{V\tau_2}{2\eta T}\mathbf{P}_0^v : d\mathbf{P}_0^v \qquad (2.38)$$

where Θ is the absolute temperature, π is the thermodynamic pressure, λ, ζ and η are the transport coefficients of thermal conductivity, bulk viscosity and shear viscosity, respectively, and τ_1, τ_o and τ_2 are the respective relaxation times of the fluxes. The right side of Equation (2.38) is composed of a temperature contribution, a pressure contribution, the contribution of the heat flux, the contribution of the bulk viscous pressure and the contribution of the viscous pressure tensor.

The evolution for the heat flux, the bulk viscous pressure and the deviatoric part of the stress tensor are governed using the following equations respectively [19]:

$$\tau_1\dot{\mathbf{q}} = -(\mathbf{q} + \lambda\Delta T) + \beta''\lambda T^2\Delta \cdot \mathbf{P}_0^v + \beta'\lambda T^2\Delta p^v \qquad (2.39)$$

$$\tau_0\dot{p}^v = -(p^v + \zeta\Delta \cdot \mathbf{v}) + \beta'\zeta T\Delta \cdot \mathbf{q} \qquad (2.40)$$

$$\tau_2(\dot{\mathbf{P}}_0^v) = -(\mathbf{P}_0^v + 2\eta\mathbf{v}_0) + 2\beta''\eta T(\Delta_0\mathbf{q})^S \qquad (2.41)$$

where the dots above the variables represent time derivatives of the variables, $\mathbf{v}$ is the barycentric velocity and $\mathbf{v}_0$ is the deviatoric traceless part of the symmetric velocity gradient. The material coefficients of β' and β'' are functions of the internal energy and specific volume.

2.4.3.2 Internal Variable Theory (IVT). In internal variable theory, internal variables are used to compliment the equilibrium state variables in the description of a system, for example Maugin and Muschik [28] define a constitutive

equation in the form of:

$$\sigma = \bar{\sigma}(\chi, \alpha) \tag{2.42}$$

where χ represents the equilibrium state variables and α represents any internal variables used. Complimenting the classic thermodynamic variables with internal variables produces a better description of the fast changing non-equilibrium system. Internal variables, such as microscopic dislocation density, are used to describe microscopic effects that are not easily observed. Also, unlike the macroscopic equilibrium state variables and EIT fluxes, internal variables cannot be controlled, only measured. Internal variables are also subject to evolution laws, for example α in equation 2.42 follows an evolution law of the form:

$$\dot{\alpha} = f(\chi, \alpha) + g(\chi, \alpha)\dot{\chi} \tag{2.43}$$

The use of IVT indicates the assumption of a local equilibrium state [26]. This allows IVT to extend beyond equilibrium thermodynamics, but requires that the thermodynamic system stay near an equilibrium state.

There are three main differences between EIT and IVT. These differences include the selection of different non-equilibrium variables, differences in the evolution equations of said variables and the ability to control the non-equilibrium state variables. The internal variables used in IVT describe microscopic features of the systems being described, while the flux variables used in EIT are invariably independent of the system. The equations describing how internal variables change with time, or evolution equations, are relaxation equations with no divergence term opposed to the flux of the EIT field variables, which are part of the balance equation themselves. Finally, the flux variables used in EIT can be controlled externally, whereas internal variables cannot [19].

2.5 Equations of State

CTH is capable of using several different equations of state in its calculations, which makes this particular hydrocode so useful in investigating the differences between different EOS. The equations of state being investigated are the Mie-Gruneisen EOS, and the Sesame EOS. The development of non-equilibrium equations of state are also presented here.

2.5.0.3 Mie-Gruneisen EOS.   The use of the Mie-Gruneisen EOS begins with the Hugoniot curve. The Hugoniot curve is an experimentally determined relationship that relates two of the following variables: pressure (P), speed of sound (c), particle velocity (v) and volume (V). Of the six potential relationships (P-c, P-v, P-V, c-v, v-V and c-V), the c-v, P-V and P-v are particularly useful. In this derivation the c-v relationship is very important. The graph of the c-v relationship typically results in a straight line. The vertical intercept (c) is referred to as the bulk speed of sound and is denoted by the variable C_0. The slope of the line, S, is also an important quantity to know. Figure 2.6 illustrates how C_0 and S are determined from the c-v Hugoniot [43].
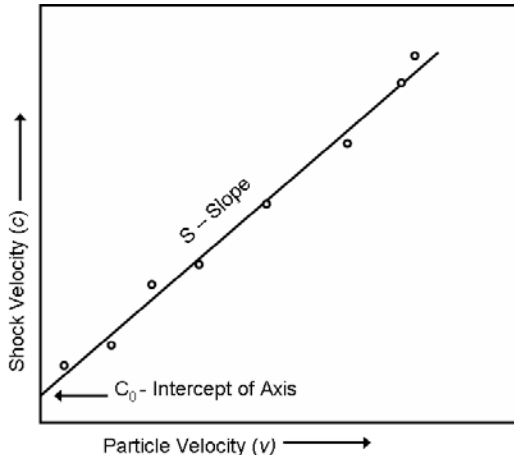
Figure 2.6:   The c-v Hugoniot

Modern methods of statically producing pressure cannot be used in the experimental determination of the shock Hugoniots for pressures greater than 10 GPa. This is where the Mie-Gruneisen EOS becomes valuable. Meyers [29] presents a derivation of the Mie-Gruneisien EOS, which is included here to give the reader an understanding of the assumptions made. The Gruneisen parameter, Γ, is derived using statistical mechanics. In statistical mechanics, the total mean vibrational energy of the crystals making up a material is equal to the sum of the product of the number of energy levels, n, the frequencies of the quantized oscillators, ν, and Plank's constant, h, over each of the 3N number of oscillators [29]:

$$\overline{E} = \sum_{j=1}^{3N} n_j h \nu_j = \sum_{j=1}^{3N} \overline{\varepsilon}_j \qquad (2.44)$$

The summation on the right side of the equation states the total mean vibrational energy is equal to the summation of the mean energies of the total oscillators, $\overline{\varepsilon}_j$. Equation(2.44) also indicates the mean energy of a harmonic oscillator is equal to the product of the number of possible energy levels, the frequencies of the quantized oscillators and Plank's constant, $\varepsilon = nh\nu$ [29].

By assuming discrete energy levels, the mean energy of an oscillator can be determined. In statistical mechanics, an energy level with more than one possible state is considered to be degenerate. Degeneracy is the number of states with a common energy level contained in a state. The relative probability of finding a system with specified levels of degeneracy, g, and energy, ε_i, in the ith level of the system is:

$$P_i = g_i e^{-\frac{\varepsilon_i}{kT}} \qquad (2.45)$$

where k is Boltzmann's constant. The absolute probability of finding a system with the specified energy levels in its ith level is found by dividing Equation (2.45) by the

total number of events, $\sum_j g_j e^{-\frac{\varepsilon_j}{kT}}$, where j is summed over all energy levels [29]:

$$P_i = \frac{g_i e^{-\frac{\varepsilon_i}{kT}}}{\sum_j g_j e^{-\frac{\varepsilon_j}{kT}}} \tag{2.46}$$

The system's mean energy, $\overline{\varepsilon}$ is found by summing the total probability and the mean energies of the oscillators over i number of energy levels [29]:

$$\overline{\varepsilon} = \sum_i P_i \varepsilon_i = \frac{\sum_i \varepsilon_i g_i e^{-\frac{\varepsilon_i}{kT}}}{\sum_j g_j e^{-\frac{\varepsilon_j}{kT}}} = -\frac{d}{d\left(\frac{1}{kT}\right)} log \left(\sum_j g_i e^{-\frac{-\varepsilon_i}{kT}}\right) \tag{2.47}$$

The summation term, $\sum_i g_i e^{-\frac{\varepsilon_i}{kT}}$, is refereed to as the partition function and is designated by Q. The partition function is the ratio of the total number of molecules present to the number of molecules on the lowest energy level. In other words Q is the population spread among the available energy levels. The partition function contains the information necessary to describe equilibrium states, meaning if Q and its temperature dependence is known, Q may be used to calculate the thermodynamic properties of a system in thermodynamic equilibrium. This is accomplished by relating the statistical description of the system (using Q) to macroscopic thermodynamics through Boltzman's relationship, Equation (2.35), to determine the entropy in the system. As discussed in Section 2.4.3 entropy is a characteristic function that may be used to describe the thermodynamic information of a system. This process allows the partition function to act as a tool in the description of the thermodynamics in a system [13].

By assuming each energy level contains only one energy state, g_i becomes one, meaning the levels are not degenerate. This causes the partition function to become [29]:

$$Q = \frac{1}{1 - e^{-\frac{h\nu}{kT}}} \tag{2.48}$$

29

Invoking this in Equation(2.47), the value of the mean energy becomes [29]:

$$\bar{\varepsilon} = -\frac{d}{d\left(\frac{1}{kT}\right)} log\left(1 - e^{-\frac{h\nu}{kT}}\right) = \frac{h\nu}{e^{\frac{h\nu}{kT}} - 1} \tag{2.49}$$

The total mean energy is then determined by summing $\bar{\varepsilon}$ over 3N number of energy levels [29]:

$$\overline{E} = \sum_{j=1}^{3N} \frac{h\nu_j}{e^{\frac{h\nu_j}{kT}} - 1} \tag{2.50}$$

In one gram-atom of material, the total energy is given by the sum of the vibrational energy, including the energy at the ground state, and the potential energy of the atoms, ϕ, where [29]:

$$\phi = \frac{1}{2}h\nu \tag{2.51}$$

The total energy of one gram-atom of material becomes [29]:

$$E = \phi(\nu) + \sum_{j=1}^{3N} \frac{1}{2}h\nu_j + \sum_{j=1}^{3N} n_j h\nu_j = \phi(\nu) + \sum_{j=1}^{3N} \left[\frac{1}{2}h\nu_j + \frac{h\nu_j}{e^{\frac{h\nu_j}{kT}} - 1}\right] \tag{2.52}$$

If the system is assumed to be at chemical equilibrium and constant temperature, the entropy will tend to reach a maximum, while the energy tends to reach a minimum. Free energy is a state function that describes the balance between these two state variables. There are two types of free energy, the Helmholtz free energy and the Gibbs Free Energy. If a constant volume is assumed, the type of free energy is defined as the Helmholtz free energy, A, which is calculated using the following relationship [13]:

$$A = e - TS \tag{2.53}$$

If a constant pressure is assumed, the Gibbs Free energy is used [13]:

$$G = H - TS \tag{2.54}$$

where H is the thermodynamic function of enthalpy equal to the sum of internal energy and the product of pressure and specific volume, $H = e + PV$.

Assuming a constant volume and inserting the total energy from Equation (2.52) into the Helmholtz free energy produces the following equation [13]:

$$A = -kT \ln \sum e^{-\frac{E_j}{kT}} = \phi(\nu) + \sum_{j=1}^{3N} \frac{1}{2} h\nu_j + kT \sum_{j=1}^{3N} \ln \left(1 - e^{-\frac{h\nu_j}{kT}}\right) \qquad (2.55)$$

By differentiating Equation (2.55) with respect to volume at a constant temperature, the equilibrium value of pressure can be found [13]:

$$P = -\left(\frac{\partial A}{\partial V}\right)_T = -\frac{d\phi}{dV} + \frac{1}{V} \sum_{j=1}^{3N} \Gamma_j \left[\frac{1}{2} h\nu_j + \frac{h\nu_j}{e^{\frac{h\nu_j}{kT}} - 1}\right] \qquad (2.56)$$

A relationship between pressure and volume has now been established, thus completing the relationship between microscopic statistical mechanics and the thermodynamics of the macroscopic system. The term Γ_j is [13]:

$$\Gamma_j = -\frac{V}{\nu_j} \left(\frac{\partial \nu_j}{\partial V}\right)_T = -\left(\frac{\partial \ln \nu_j}{\partial \ln V}\right)_T \qquad (2.57)$$

A crystal's resistance to compression causes the frequency the particles are vibrating at to increase with an increase in the pressure applied to the crystal. Since the vibrational frequency increases as volume decreases, $\Gamma > 0$. Gruneisen assumed all oscillators in a system have the same Γ, named the Gruneisen constant [13]:

$$\Gamma = -\left(\frac{\partial \ln \nu}{\partial \ln V}\right)_T \qquad (2.58)$$

Making all Γ equal in the pressure equation allows for the removal of the summation term from Equation (2.56), thus [13]:

$$P = -\frac{d\phi}{dV} + \frac{\Gamma}{V} E_{VIB} \qquad (2.59)$$

When this pressure equation is applied atS a temperature of 0 K it becomes [13]:

$$P_{0K} = -\frac{d\phi}{dV} + \frac{\Gamma}{V}E_{0K} \tag{2.60}$$

Subtracting Equation (2.60) from Equation (2.59) yields [13]:

$$P - P_{0K} = \frac{\Gamma}{V}(E - E_{0K}) \tag{2.61}$$

This equation is a form of the Mie-Gruneisen EOS that relates P, V and E to the pressure and internal energy at 0 K. A point on the Hugoniot plot may also be used in which case the Mie-Gruneisen EOS becomes [13]:

$$P - P_H = \frac{\Gamma}{V}(E - E_H) \tag{2.62}$$

Equations (2.61) and (2.62) can each be divided into two parts [10]. The first is either a Hugoniot or a zero-Kelvin isotherm, defined in Section 2.5.0.4, which represents the pressure at a known state. The second part of the equations is the contribution of vibrational, or thermal energy of the crystal lattices. In other words the Mie-Gruneisen EOS can be represented mathematically as [22]:

$$P = P_0 + P_{vib} \tag{2.63}$$

2.5.0.4 Sesame EOS. CTH also contains the Sesame tabular equation of state in which the thermodynamic state of the system is described using tables within CTH. This allows CTH to reach solutions for conditions where materials are present in various phases due to extreme pressures and temperatures. Kerley [20] [21] provides detailed descriptions on how the Sesame EOS tables are built for iron and aluminum respectively. The methods used to built both tables are contained in this section.

The Sesame EOS for iron was developed by first constructing the EOS for the α, γ and ϵ phases of iron using the PANDA code, which provides the capability to model materials with complex phase diagrams. These solid phases include contributions from the zero-Kelvin isotherm, lattice vibrations, and thermal electronic excitations. The α phase also includes a magnetic contribution. Thus the thermodynamic functions of pressure, internal energy and Helmholtz free energy are assumed to have the following forms [20]:

$$P(\rho, T) = P_c(\rho) + P_l(\rho, T) + P_m(\rho, T) + P_e(\rho, T), \tag{2.64}$$

$$e(\rho, T) = e_c(\rho) + e_l(\rho, T) + e_m(\rho, T) + e_e(\rho, T) + \Delta e_b, \tag{2.65}$$

and

$$A(\rho, T) = e_c(\rho) + A_l(\rho, T) + A_m(\rho, T) + A_e(\rho, T) + \Delta e_b, \tag{2.66}$$

Where the subscripts c, l, m and e represent the contributions from the zero-Kelvin curve, lattice vibrations (including the zero point term), magnetic excitations (contribute to the α phase only) and thermal electronic excitations, respectively. ΔE_b represents cohesive energy, which is used to correct for the zero-point lattice energy.

The zero-Kelvin curves are also referred to as cold curves, and account for materials in ground states with the nuclei of the atoms arranged in perfect crystal lattices. This partition of the EOS accounts for the cohesive forces leading to condensed phases of materials and the repulsive forces that determine a materials response to compression. This term is also the largest contributor to the EOS over much of the density-temperature regions commonly studied. [22]

The zero-Kelvin curves are developed by taking the experimentally determined compression curves for the α and ϵ phases developed similarly to the Hugoniot curves mentioned in Section 2.5.0.3, and subtracting the contributions from P_l and P_e as they are calculated in the subsequent paragraphs. The remaining pressure is then fit to the Birch-Murnaghan isothermal EOS, which defines pressure in terms of the ratio of the density to the reference density, $\eta = \rho/\rho_0$ and the isothermal bulk modulus,

β_0 [42]:

$$P_c(p) = \frac{2}{3}\beta_0 \left(\eta^{\frac{7}{3}} - \eta^{\frac{5}{3}} \right) \left[1 + \frac{3}{4} \left(\eta^{\frac{2}{3}} - 1 \right) (\beta_0' - 4) \right] \tag{2.67}$$

For the γ phase, ρ_0 is fixed by fitting the thermal expansion data, and the values of β_0 and β_0' are taken as intermediate values between the values of the α and ϵ phases. Panda is then used to compute a thermodynamically consistent energy. [20]

The Lattice vibration, or nuclear degree of freedom (DOF) contribution, is calculated using the popular Debye model. Debye hypothesized the strong bonds in a solid dictate the oscillations of one atom affects those of other atoms, and an idealized frequency distribution of these vibrations is required to model these effects. The Debye distribution is built defining a maximum frequency vibration of ν_m that acts as an upper limit, and then assigns values to the rest of the frequencies [14]:

$$\begin{cases} g(\nu) & = \frac{12\pi E_p \nu^2}{c^3} \ (if \ \nu < \nu_m) \\ g(\nu) & = 0 \ (if \ \nu > \nu_m) \end{cases} \tag{2.68}$$

where E_p is the potential energy, ν is the vibration frequency, ν_m is an upper limit of vibration frequency and c is the wave velocity. The use of the Debye distribution allows for the description of the principle features of the lattice vibration term by using simple select parameters. The parameters used to find the lattice vibration contribution to the overall EOS includes the Debye temperature, $\Theta_{ref} = \frac{h\nu_m}{k}$ [14], the Gruneisen parameter at room temperature, Γ_{ref}, the density ρ_{ref}, and a constant, τ which helps define the Gruneisen function's dependence on density. The lattice contribution to the Sesame EOS is calculated using the Sandia code Panda, the inner workings of which are unavailable, however a simple form of the energy contribution is found using [22]:

$$e_l(\rho, T) = Nk \left[\frac{9\Theta_{ref}}{8} + 3TD(x_m) \right] \tag{2.69}$$

34

where D represents the Debye function [42]:

$$D(x_m) = \frac{3}{x_m^3} \int_0^{x_m} \frac{x^3 dx}{e^x - 1} \qquad (2.70)$$

and $x_m = \frac{\Theta_{ref}}{T}$. The pressure contribution, P_l is found using by multiplying the density, Gruneisen parameter and Equation (2.69) [22]:

$$P_l(\rho, T) = \rho \Gamma(\rho) e_l \qquad (2.71)$$

This assumes the Gruneisen parameter is a function of density and is found using the relationship [20]:

$$\Gamma(\rho) = (\Gamma_{ref} - 0.5) \left(\frac{\rho_{ref}}{\rho} \right)^\tau - 0.5 \qquad (2.72)$$

Note that when the EOS accounts for only the zero-Kelvin curve and the lattice vibration term, it can be shown that the EOS will reduce to the Mie-Gruneisen EOS. For example, without the electronic contribution term the pressure equation looks like [22]:

$$P(\rho, T) = P_c(\rho) + P_l(\rho, T) \qquad (2.73)$$

which is similar to Eqn (2.63).

The magnetic contribution to the Sesame EOS, was handled similarly to that of Andrews [3] and is included because it provides a significant contribution to the specific heat of α iron allowing for the determination of temperature and internal energy. The magnetic contribution to the α phase of iron relies heavily on the noted behavior of the Curie temperature of α iron. The Curie temperature is the temperature above which a material loses its ferromagnetic properties [33]. The Curie temperature for iron has been observed to be independent of pressure, which leads to the ability to approximate the magnetic contribution to the EOS as independent of density. This leads to the conclusion that the magnetic contribution to the pressure term is negligible ($P_m = 0$). Below the Curie temperature, the heat capacity is found using the

35

empirical formula [20]:

$$C_{V_m}(T) = \frac{kT^{1.5}}{(T_0 - T)} \tag{2.74}$$

where T_0 is the Curie temperature and k is an empirical constant, both of which were adjusted to match experimental data. In a departure from Andrews, at temperatures above the Curie point $C_{V_m} = 0$. Equation (2.74) is numerically integrated to determine E_m and A_m.

Impact phenomena, among other phenomena (thermal gradients, explosions, etc...), may cause the material to become hot enough the electrons become very excited and consequently leave their ground energy states. This electronic excitation may have a significant effect on the thermodynamic properties of materials at high temperatures, and if the temperature is high enough, the electronic excitation term may dominate the EOS. For iron, the Sesame EOS model predicts that thermal electronic contribution begins to take effect at temperatures above 500K. Electronic excitation also makes a significant contribution to the thermal expansion, which agrees well with experimental data [20] [22].

Two separate models are used to calculate the contribution of electronic excitation to the Sesame EOS. For densities above $6\frac{g}{cm^3}$ the INFERNO model of Liberman [25] is used, and for densities below $1\frac{g}{cm^3}$ the ionization equilibrium (IONEQ) is used. An average of the two models is used in the intermediate densities. [20]

The INFERNO model, models the potential of an atom by taking an ion sphere and surrounding it with a positive charge and an electron gas simulating the neighboring atoms. Then uses statistical and quantum mechanics to develop the desired EOS. The energies and wave functions for the discrete and continuum electronic levels are obtained by solving the Dirac equation for kinetic energy of electrons [20]. The INFERNO model simplifies the computation of the electronic excitation term at high densities [22].

Ionization equilibrium theory handles a system as a mixture of free electrons and ions at its simplest form [22]. The free electrons are treated as an ideal gas,

while the ionic contributions are modeled using partition functions. The state of ionization is described using temperature and density, and is determined by either minimizing the free energy or balancing the rates of ionization and recombination of the atoms involved. Both methods assume thermodynamic equilibrium, thus the name ionization equilibrium theory. The calculation of the electronic excitation term using IONEQ is numerically expensive, limiting its use to low densities.

A table of iron's fluid phase was built with the thermal electronic term and fluid perturbation theory, which treats the atomic motions of the material. The fluid phase EOS also describes the material in the vapor and supercritical regimes [20].

The Sesame tables for the different phases of iron are built using the theories listed above. Then, where possible, experimental data are used to match the material parameters used in iron's Sesame EOS [20].

A Sesame EOS also exists for aluminum, in which the equations for pressure, internal energy and Helmholtz free energy are given by [21]:

$$P(\rho, T) = P_c(\rho) + P_l(\rho, T) + P_e(\rho, T) \tag{2.75}$$

$$e(\rho, T) = e_c(\rho) + e_l(\rho, T) + e_e(\rho, T) \tag{2.76}$$

and

$$A(\rho, T) = e_c(\rho) + A_l(\rho, T) + A_e(\rho, T) \tag{2.77}$$

The subscript c stands for the contributions of the zero-Kelvin curve, represented by the analytic formula [21]:

$$e_c(\rho) = -E_0 \left(1 + \xi + 0.05\xi^3\right) e^{-\xi} \tag{2.78}$$

where

$$\xi = \left(\frac{9\beta_0}{\rho_0 E_0}\right)^{\frac{1}{2}} \left[\left(\frac{\rho_0}{\rho}\right)^{\frac{1}{3}} - 1\right] \tag{2.79}$$

and ρ_0 is the density, E_0 is the cohesive energy, and β_0 is the solid bulk modulus, all taken at zero pressure.

The subscript l indicates the contribution from the lattice vibrations, and the subscript e indicates the contribution of electronic excitation. Both of which are computed in the same way the respective iron contributions are calculated.

The fluid phase of Aluminum is calculated using the CRIS [23], model which includes contributions from the ground state electronic degrees of freedom and the contribution of the nuclear degrees of freedom. The contribution from the CRIS model is added to the electronic contribution to describe the thermodynamic state of the fluid [21]:

$$A_{fluid}(\rho, T) = A_n(\rho, T) + A_e(\rho, T) \tag{2.80}$$

where n indicates the contribution of the CRIS model.

2.5.0.5 Multi-Phase Equations of State. The numerical modeling of impacts involving iron present unique numerical difficulties due to the fact that at pressures of approximately 13 MPa, iron undergoes a solid-solid phase change from its original α phase to the ϵ phase [5]. In order to model these different phases accurately, two different sets of Mie-Gruneisen parameters are needed. In CTH you are only able to use the parameters for one phase at a time. This means great care is needed in selecting which set of Mie-Gruneisen parameters to use. However, CTH has a composite EOS named Phase Transition Reactive Burn (PTRAN) that enables a material exhibiting multiple phases to be modeled. PTRAN is referred to as a composite model, because it is constructed from basic EOS models such as Sesame and the Mie-Gruneisen EOS. The PTRAN EOS uses a phase boundary to assist in describing the pressure of iron in the phase transition region using the formula [7]:

$$P(\rho, T, \lambda) = P_T + \beta_T \left(1 - \frac{\rho_T}{\rho} \right) + A_T \left(T - T_0 \right) + A_\lambda \lambda \tag{2.81}$$

where P_T and ρ_T are the pressure of the transition and the density of phase 1 or α phase of iron, λ is the mass fraction of phase 2 or ϵ phase of iron, T_0 denotes room temperature, β_T in the bulk modulus in the transition region and A_T and A_λ are the derivatives of the transition pressure with respect to T and λ. PTRAN has the option to be run in either reversible or irreversible mode, though the documentation does not specify the theory behind either. Unfortunately there is limited documentation on this EOS, hindering the ability to understand what it is doing. The PTRAN EOS is also capable of incorporating some non-equilibrium thermodynamic effects into an equation of state around a phase change region using λ as an additional internal variable.

The Sesame equation of state is able to model the thermodynamic properties of impacts involving iron much better as it has tables on three different solid phases of iron. The multiphase EOS table is constructed from the EOS tables of the individual phases. In a phase transition, more than one phase is present. In equilibrium thermodynamics when two phases are present the Gibbs free energy of the two phases must be equal. When only one phase is present, it is the one with the lower value of the Gibbs free energy [2]. For this reason in the iron Sesame table, the phase exhibiting the lower value of Gibbs free energy, at a given temperature and pressure, is considered to be the more stable phase and its thermodynamic properties are used [20]. The use of the Gibbs free energy indicates a constant pressure is assumed and is used because the thermodynamic description of the phase used is specified using temperature and more importantly, pressure. The Helmholtz free energy, which assumes constant volume, would be used if temperature and density were specified.

CTH allows cells in the mesh to be divided into subcells, with each subcell representing different materials. This allows for the ϵ phase of the iron to be present in the same cells as the original α phase. CTH is also capable of modelling the different phases of iron contained in a cell at different temperatures and pressures [15]. To determine the cells final temperature and pressure a weighted average is used. This thermodynamic setting is not able to account for pressure relaxation.

Table 2.3:   EIT Variable Definitions

Variable	Definition
$\mathbf{q}$	Heat Flux
S	Entropy
p^v	Viscous Pressure
$\mathbf{P}_0^v$	Viscous Pressure Tensor
π	Thermodynamic Pressure
Θ	Absolute Temperature
λ	Thermal Conductivity Transport Coefficient
ζ	Bulk Viscosity Transport Coefficient
η	Shear Viscosity Transport Coefficient
τ_n	Relaxation Time of Respective Fluxes

2.5.0.6   Non-Equilibrium Equations of State.   The development of an EOS that can describe how solid materials act behind shock waves is of great interest and the irreversible thermodynamic theories discussed in Section 2.4.3.2 may be used to help model such phenomena. Non-equilibrium EOS for a one component fluid and developed with the use of EIT are given below as an example of how irreversible thermodynamic theories may be utilized in the modeling of non-equilibrium systems. For convenience Table 2.3 includes the variables used in these EOS, first introduced in Section 2.4.3.1.

In their review of EIT, Jou et al [19] integrate the Gibbs equation in the form of Equation (2.38):

$$dS = \Theta^{-1}de + \Theta^{-1}\pi dV - \frac{V\tau_1}{\lambda T^2}\mathbf{q} \cdot d\mathbf{q} - \frac{V\tau_0}{\zeta T}p^v dp^v - \frac{V\tau_2}{2\eta T}\mathbf{P}_0^v : d\mathbf{P}_0^v$$

to develop non-equilibrium equations of state for the thermodynamic pressure and absolute temperature. The EOS for Θ is found by integrating Equation (2.38) with respect to internal energy [19]:

$$\Theta^{-1} = T^{-1} - \frac{1}{2}\left[\frac{\partial\left(\frac{V\tau_1}{\lambda T^2}\right)}{\partial e}\mathbf{q}\cdot q + \frac{\partial\left(\frac{V\tau_0}{\zeta T}\right)}{\partial e}(p^v)^2 + \frac{\partial\left(\frac{V\tau_2}{2\eta T}\right)}{\partial e}\mathbf{P}_0^v : \mathbf{P}_0^v\right] \tag{2.82}$$

and the EOS for π is found by integrating Equation (2.38) with respect to specific volume [19]:

$$\Theta^{-1}\pi = T^{-1}p - \frac{1}{2}\left[\frac{\partial\left(\frac{V\tau_1}{\lambda T^2}\right)}{\partial V}\mathbf{q}\cdot q + \frac{\partial\left(\frac{V\tau_0}{\zeta T}\right)}{\partial V}(p^v)^2 + \frac{\partial\left(\frac{V\tau_2}{2\eta T}\right)}{\partial V}\mathbf{P}_0^v:\mathbf{P}_0^v\right] \qquad (2.83)$$

The use of these expressions assumes that non-equilibrium definitions of Θ and π exist. Third order terms in these equations of state are considered to be negligible and therefor are not included. Had second order flux terms been included in Equation 2.38, a third order term would be present.

Another method of producing a quasi non-equilibrium EOS, is including an equilibrium EOS, such as the Mie-Gruneisen or Sesame EOS, inside a rate equation enabling it to describe the thermodynamics of a system away from equilibrium . Lu and Hanagud [27] [26] use this method in their works detailed in the following section. Although this method allows the EOS to describe the system instantaneously, the equilibrium EOS are still limited by the equilibrium thermodynamic assumptions used in the development of the respective EOS. An example of such equilibrium assumptions is the use of the ionization equilibrium theory in the Sesame EOS, which assumes the rates of ionization and recombination occurring are equal and frozen. In reality, the rates of ionization and recombination are not equal to each other and change over time. Thus, this assumption limits the ability of the Sesame EOS to describe a system in non-equilibrium, even when used in a rate equation.

2.6 *Modeling of Non-Equilibrium Thermodynamic Systems*

Lu and Hanagud [27] [26] model an impact loading scenario in the framework of continuum mechanics and non-equilibrium thermodynamics by combining the use of classical equilibrium state variables and selected non-equilibrium state variables, with their evolution equations, in the framework of EIT and IVT.

The set of governing equations used in the modeling of the non-equilibrium system requires 12 equations consisting of the conservation equations (Equations 2.95, 2.96 and 2.97), equilibrium constitutive equations (Equations 2.91, 2.92 and 2.86), non-equilibrium constitutive equations (Equations 2.89, 2.90 and 2.88), a kinematic equation (Equation 2.84), a geometric equation (Equation 2.85) and some additional equations (Equations 2.93 and 2.94). The governing equations used are given below as an example of how non-equilibrium thermodynamics may be used to model impact phenomena. For brevity, just the governing equations previously listed and some evolution equations are included here, sources [27] [26] may be consulted to determine how supporting variables are calculated.

The non-equilibrium components of the governing equations are developed using IVT and EIT. IVT is used to describe the microscopic dislocation of segments in the crystal lattice in an active slip system, α. The orientation of the slip system is described by the internal variable tensor, Z_{ij}^α and is referred to as the Schmidt orientation tensor. The other internal variable utilized is the dislocation density, ρ_d^α, is a scalar density describing the collective length of dislocation segments in α.

The rate of plastic deformation, $U_{ij}^{plastic}$ is a kinematic relationship used to help describe the NET system. It is a function of ρ_d^α, the magnitude of the vector describing the motion of the slip system, or gliding velocity, v^α, the magnitude of the Burgers vector, b^α and Z_{ij}^α. It is determined using the following equation:

$$U_{ij}^{plastic} = \frac{1}{2} \sum_\alpha \rho_d^\alpha b^\alpha v^\alpha (Z_{ij}^\alpha + Z_{ji}^\alpha) \qquad (2.84)$$

To account for lattice rotations, the spin vector, $\omega_i = -e_{ijk}\Omega$ and the angle of Z_{ij}^α, $\Gamma_i = -e_{ijk}Z_{ij}^\alpha$ are utilized. By combining these terms the evolution of Z_{ij}^α is determined using the geometric description:

$$\frac{\partial \Omega_i}{\partial t} = \omega_i \qquad (2.85)$$

where Ω is the angle of orientation, and ω_i represents the rate of change of Ω and is refered to as the spin vector.

As the material undergoes deformation, the number of dislocations in a system are going to change, affecting the value to the dislocation density. The evolution equation governing the change of ρ_d^α is described using the following differential equation:

$$\frac{\partial \rho_d^\alpha}{\partial t} + \frac{\partial (\rho_d^\alpha v_k)}{\partial x_k} = K^\alpha \tag{2.86}$$

where K^α is a source term made of contribution of the dislocation nucleation by shock loading, K_n^α the dislocation multiplication, K_m^α and the dislocation reaction, K_j^α:

$$K^\alpha = K_n^\alpha + K_m^\alpha + K_j^\alpha \tag{2.87}$$

The thermodynamic fluxes derived from EIT include the dislocation motion, v_i^α, the non-equilibrium stress, σ_{ij}^{ne} and the heat flux, q_i. The dislocation motion describes the motion of the slip system and is made of the magnitude of the velocity, v^α and the gliding direction, m_i^α. The evolution of the dislocation motion is described using:

$$\begin{cases} \tau_d^\alpha \frac{Dv^\alpha}{Dt} &= -v^\alpha + \frac{\sigma_{eff}}{k_d^\alpha T} \quad (if\ \sigma_{ext}^\alpha > \sigma_{ext,cr}) \\ v^\alpha &= 0 \quad (otherwise) \end{cases} \tag{2.88}$$

where σ_{eff}^α is the local resolved shear stress, σ_{ext}^α is the external shear stress, $\sigma_{ext,cr}^\alpha$ is the critical stress, k_d^α is the resistance to dislocation motion and $\frac{Dv^\alpha}{Dt}$ is referred to as the substantial derivative of dislocation motion, which in one-dimension consists of the local derivative, $\frac{\partial v^\alpha}{\partial t}$ and the convective derivative, $v \frac{\partial v^\alpha}{\partial x}$. As Equation (2.88) indicates, the dislocation motion in a system is zero until a critical stress, $\sigma_{ext,cr}$ is reached.

The non-equilibrium stress, σ_{ij}^{ne}, is a function of the elastic strain rate, U_{kl}^e and the relaxation time of the viscous process, τ_ν. In solid metallic materials viscous processes include the viscous slip of the phase and grain boundaries or viscous lattice

stretching. In liquid metals the viscous process refers to the viscous flow of the material. Using the aforemention processes the evolution of the non-equilibrium stress is governed by the following differential equation:

$$\tau_\nu(\ddot{\sigma_{ij}^{ne}}) = -\sigma_{ij}^{ne} + \eta_{ijkl}\, U_{kl}^{e} \tag{2.89}$$

in which ¨ represents the material time derivative.

The evolution of the heat flux, q_i, is also found using a differential equation:

$$\tau_q \ddot{q}_i = -q_i - k_{ij}\frac{\partial T}{\partial x_j} \tag{2.90}$$

where τ_q is the relaxation time of the heat flux.

In order to instantaneously define the value of pressure, the equilibrium EOS, $P^e = P^e(\rho, T)$, is found using the differential equation:

$$\dot{P^e} = A(\rho, T)\left(\frac{1}{3}U_{ii}^e\right) + B(\rho, T)\dot{T} \tag{2.91}$$

This is an example of using an equilibrium EOS in a rate equation to give the NET hydrocode the ability to instantaneously describe the thermodynamics of the system.

The deviatoric stress, σ_{ij}^{ed}, is a function of the elastic modulus, G_{ijkl}, and the deviatoric portion of the deformation tensor, U_{kl}^{ed}. It is found using the rate equation:

$$\ddot{\sigma_{ij}^{ed}} = G_{ijkl}U_{kl}^{ed} \tag{2.92}$$

The total deformation and stress tensors are found by summing their equilibrium and non-equilibrium components, as shown in Equations (2.93) and (2.94).

$$\sigma_{ij} = \sigma_{ij}^{e} + \sigma_{ij}^{ne} \tag{2.93}$$

and

$$U_{ij} = U_{ij}^e + U^n e_{ij} \qquad (2.94)$$

Finally, the equilibrium based governing equations consists of the familiar conservation equations [26]:

$$\frac{D\rho}{Dt} + \bar{\rho}\frac{\partial v_k}{\partial x_k} = 0 \qquad (2.95)$$

$$\rho\frac{Du_i}{Dt} - \frac{\partial \sigma_{ij}}{\partial x_k} = \rho F_i \qquad (2.96)$$

$$\rho\frac{De}{Dt} - \frac{\partial q_i}{\partial x_i} - \sigma_{ij}U_{ij} = 0 \qquad (2.97)$$

III. Comparison of Sesame and Mie-Gruneisen Based EOS

This portion of the numerical investigation compares the ability of different EOS to model impact phenomena. The EOS being compared consist of the Mie-Gruneisen EOS for aluminum, the PTRAN EOS for iron, which includes the Mie-Gruneisen EOS of α and ϵ iron, and the Sesame EOS for both aluminum and iron. The comparison of these EOS will be performed in four different parts. The first part compares the ability of the Mie-Gruneisen and Sesame EOS to model uniaxial impacts of aluminum over a range of impact velocities. The second part consists of simulating uniaxial iron plate impact experiments with the PTRAN and Sesame EOS. The third part consists of comparing the Sesame EOS to both the reversible and irreversible PTRAN EOS to determine the Sesame EOS's ability to model irreversible systems. The fourth and final part compares the answers generated using all three EOS to flyer plate data gathered by Cinnamon [9] while investigating gouging phenomena for the HHSTT.

Non-equilibrium thermodynamic theories build upon equilibrium thermodynamics. This requires a thorough understanding of equilibrium thermodynamic theories. By comparing the equilibrium thermodynamics contained in the Mie-Gruneisen EOS to those of the Sesame EOS, a thorough understanding of how CTH models impact phenomena is built. Understanding these differences also assists in determining the physics the currently equilibrium VFVC may fail to capture.

The uniaxial mesh cell width used in all the CTH simulations is 0.002 cm. This size concurs with what Szmerkovsky [35] found to best model the continuum mechanics of the system. The uniaxial mesh used in each simulation is also designed to be wider than the combined width of the flyer and target plates, with empty space next to the outside of each plate. This allows the outside boundaries of both plates to act as free surfaces allowing for the appropriate reflection of the shock waves.

The equilibrium thermodynamic values in each run are measured off the wave history generated using tracer points. In each impact scenario, the tracer point used is located in the center of the target. This allows the compression waves to fully form in a region free from the interference and wave reflections seen at the edges

46
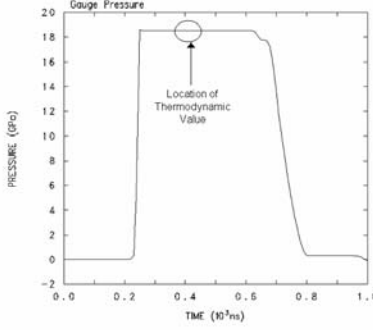
Figure 3.1:   Position of Captured Thermodynamic Values

of the targets. The values of the thermodynamic state variables are measured at locations on the compression wave well behind the front of the wave, as shown in Figure 3.1. Measuring the value of the thermodynamic variables at this location, assures the value is free from any numerical noise, or possibly any non-equilibrium effects, thereby assuring the equilibrium values of the thermodynamic variables are obtained.

3.1   Comparing the Mie-Gruneisen and Sesame EOS in the Uniaxial Impact of Aluminum

3.1.1   Numerical Setup and Procedure for Aluminum Impacts.   The comparison of the Mie-Gruneisen and Sesame EOS compares how the respective EOS model the uniaxial impact of aluminum. The material choice of aluminum is made for two reasons. First, the documentation describing the development of these equations of state is publicly available. The availability of this documentation, specifically the Sesame EOS, is necessary to make sure the Sesame tables are built using the same theories used in the development of the iron EOS. In addition, said documentation is beneficial in the design of the numerical simulation contained in this investigation. The second reason is aluminum, unlike iron, is not polymorphic. This allows for a direct comparison between the Mie-Gruneisen EOS and the Sesame EOS without

47

Table 3.1:	Mie-Gruneisen Coefficients Used in CTH				
Coefficient	ρ_0	C_0	S	Γ_0	C_v
Value	$2.760 \ \frac{kg}{m^3}$	$5330 \ \frac{m}{s}$	1.34	2.16	$900 \ \frac{J}{kg \, K}$
Source	[21]	[29]	[29]	[21]	[4]

Flyer
0.13 mm

Target
3.327 mm

Impact Velocity ⟶

Mesh Cell Size = 0.002 cm
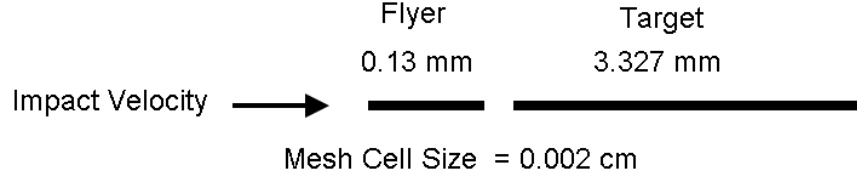
Figure 3.2: CTH Mesh Used to Match the Experimental Setup of Bekinskii and Khristoforov

the need to handle the phase changes occurring in polymorphic materials under high temperatures or pressures.

The form of the Mie-Gruneisen EOS used by CTH is given in Equation (3.1) [7]:

$$\begin{cases} P(\rho, e) & = P_H(\rho) + \Gamma_0 \rho_0 \left[e - e_H(\rho) \right] \\ e(\rho, T) & = e_H(\rho) + C_v \left[T - T_H(\rho) \right] \end{cases} \tag{3.1}$$

Where the H subscript denotes values determined using the Hugoniot and the 0 subscript denotes the original values for Γ and ρ. The CTH EOS package does not contain predefined Mie-Gruneisen coefficients for aluminum, so said inputs need to be given to CTH. Table 3.1.1 contains the Mie-Gruneisen coefficients manually specified inside the CTH input deck in SI units. These coefficients come from several different references, each of which is noted in Table 3.1.1.

To validate these coefficients, they are used in an impact simulation in CTH with an impact velocity of 2020 $\frac{m}{s}$, matching an impact experiment performed by Bekinskii and Khristoforov [16]. The mesh used in this validation attempt is an uniaxial recreation of Bekinskii and Khristoforov's flyer plate geometry and is shown in Figure 3.2. According to Bekinskii and Khristoforov the pressure behind the shock waves should reach a pressure of 18.3 GPa. A tracer point is placed in the center
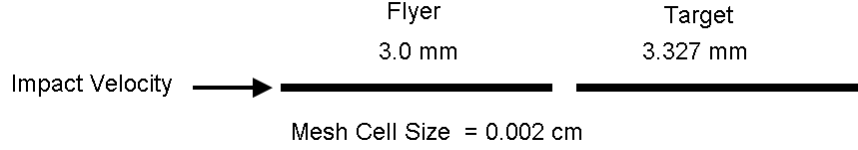
Figure 3.3:   Altered CTH Mesh Used to Match the Experimental Data of Bekinskii
and Khristoforov

of the target and is used to show the history of the pressure wave, which is shown
in Figure 3.4a. Looking at the figure, it is obvious that the numerically generated
pressure of 12.6 GPa is well short of the predicted 18.3 GPa. This inaccurate pressure
is caused by a mixture of the artificial viscosity and wave reflection. The artificial
viscosity spreads the front of the shock wave over several cells, allowing CTH to
handle the discontinuity. However, this also slows the development of the shockwave.
While CTH develops the shock wave front, a rarefaction wave from the flyer passes
through and stops the shock wave from completely forming. To fix this, the width
of the flyer plate is extended to 3.0 mm, producing the final mesh shown in Figure
3.3. Lengthening the flyer plate increases the time it takes for the rarefaction wave
to reach to the location of the tracer point, allowing CTH to fully develop the front
of the shockwave.

The results generated by CTH using this second mesh are located in Figure 3.4b.
The numerical pressure of 18.4 GPa compares favorably with the results of Bekinskii
and Khristoforov. For this reason, the mesh shown in Figure 3.3 is the mesh used in
the numerical simulations.

The Johnson Cook constitutive relationship is used to model the material re-
sponse of aluminum in the impact scenarios. The pre-defined JC coefficients for
aluminum contained within CTH are used.

The comparison of the Mie-Gruneisen and Sesame EOS consists of modeling the
impact of two aluminum bars over a range of impact velocities. The impact velocities
begin at an impact velocity of 500 $\frac{m}{s}$, and are increased in increments of 500 $\frac{m}{s}$ until
a max velocity of 6000 $\frac{m}{s}$ is reached. The maximum velocity of 6000 $\frac{m}{s}$ is set to avoid
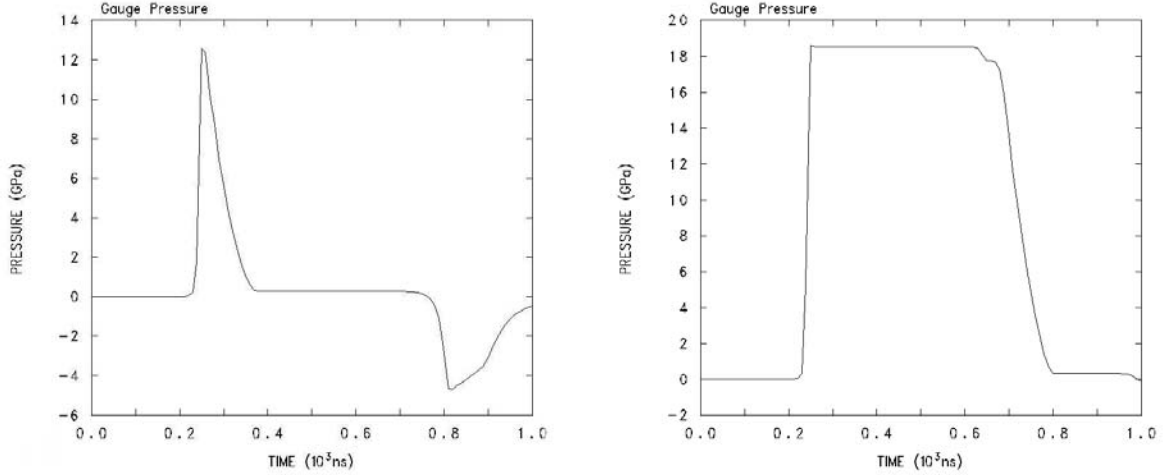
a	b
Flyer Plate Thickness of 0.13 mm	Flyer Plate Thickness of 3.0 mm

Figure 3.4:   Pressures Generated by Aluminum at an Impact Velocity of 2020 m/s Using Different Flyer Plate Lengths

any melting that may occur at the higher impact velocities [21]. Any melting will render the results generated by the Mie-Gruneisen EOS useless, due to the EOS's inability to handle phase transitions on its own. Both EOS will be used to model the impact at each impact velocity value. The results generated for each EOS will then be compared.

3.1.2 Results of Uniaxial Impact Simulations with Aluminum Comparing the Mie-Gruneisen and Sesame EOS.   In this section, the results generated by the uniaxial impacts of Aluminum are presented and analyzed. First, the values of the thermodynamic variables generated are plotted against their respective impact velocities. This compares the ability of the Mie-Gruneisen and Sesame EOS to model impact phenomena. Then the thermodynamic variables are plotted against each other determining how the two EOS handle the thermodynamics of the system.

Figure 3.5 shows how the different thermodynamic variables change with respect to impact velocity. Upon study, Figure 3.5 shows the numerical values of temperature

50

a. Density

b. Temperature

c. Internal Energy
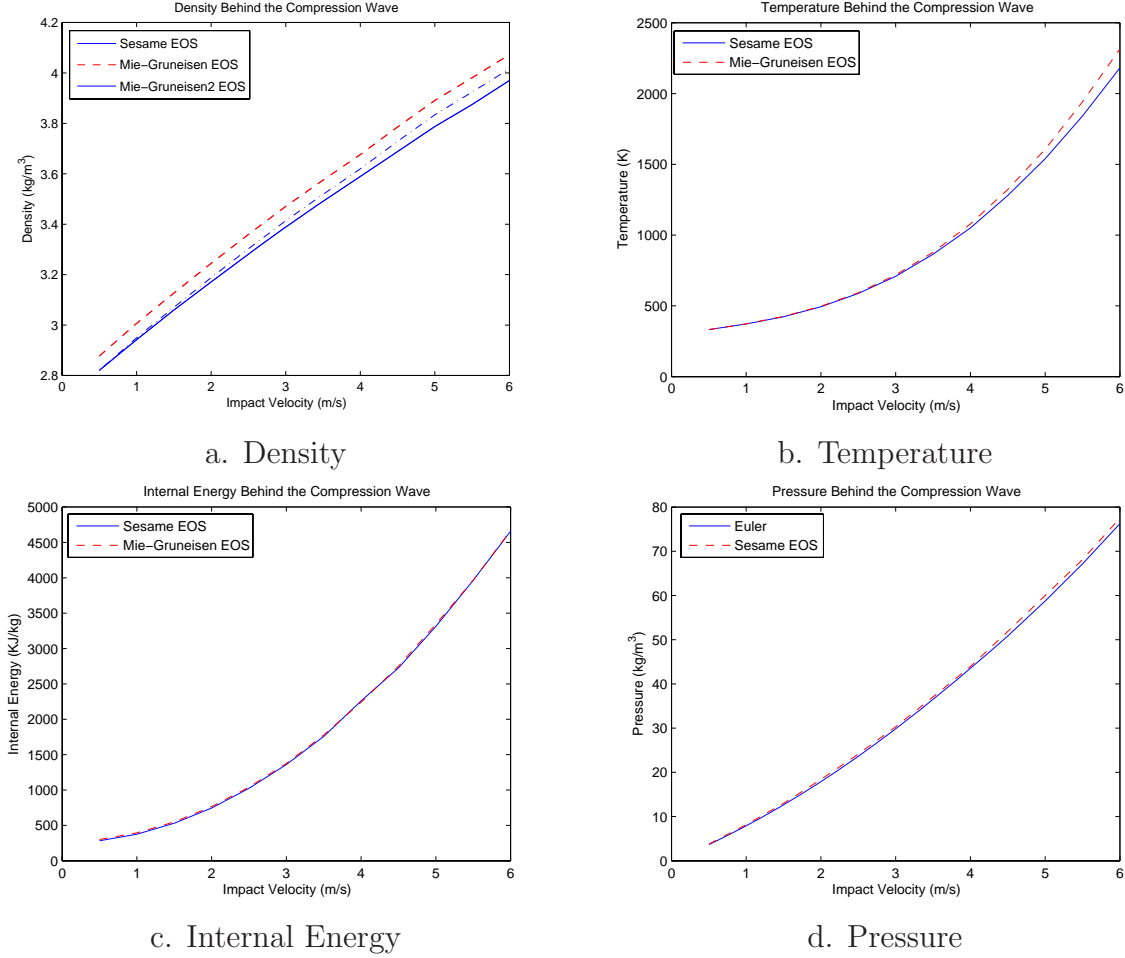
d. Pressure

Figure 3.5:   Comparison of Numerical Values of Density, Temperature, Pressure and Internal Energy Generated by the Sesame and Mie-Gruneisen EOS for Aluminum

and density generated by the Mie-Gruneisen and Sesame EOS diverging as the impact velocity increases. This is in contrast with the generated values of internal energy and pressure, which appear to correlate well over the entire range of impact velocities. This correlation indicates the pressures and internal energies generated for particular impact scenarios will be close in value, regardless of whether the Mie-Gruneisen or Sesame EOS are used.

Figure 3.6 gives the percent difference between the thermodynamic values generated by the Sesame and Mie-Gruneisen EOS over the entire range of impact velocities. The percent difference of temperature is represented by a dashed line, showing as the

impact velocity increases the percent difference between the EOS also increases. This increase in difference between the values generated with the different EOS is reflective of what is seen in Figure 3.5b, meaning the generated temperatures correlate well at impact velocities below 3500 $\frac{m}{s}$ with percent differences of less than 2%, while at higher impact velocities the percent difference increases at a faster rate. The density percent difference curve, represented with a solid line, shows the difference between the values generated using the two EOS remains within remain between 2% and 3%, while showing a steady increase over the entire range of impact velocities. The density curve also reflects what is seen in Figure 3.5a.

The percent differences of internal energy and pressure, represented by the dashed dot line and dotted line respectively, do not appear to reflect what is seen in their respective graphs in Figure 3.5, meaning the graphs in Figure 3.5 appear to follow the same line, while the respective percent differences begin with high values and decrease over the range of the impact velocities. These great percent difference values at the low impact velocities and the low percent difference values at the high impact values is due to the range of internal energy and pressure values generated. For example, the standard deviation, a measure of variability representing the average difference of two sets of data from the mean of said data sets [11], of the difference between the values of internal energy generated with the two equations of state is 13.9 $\frac{kJ}{kg}$. The standard deviation of the difference is 4.4% of the internal energy (283 $\frac{kJ}{kg}$) generated at an impact velocity of 500 $\frac{m}{s}$, but it is 0.3% of the internal energy (4659.1 $\frac{kJ}{kg}$) generated at an impact velocity of 6000 $\frac{m}{s}$. The values of pressure follow a similar pattern, though not as extreme. Bottom line, this all means the two EOS correlate better at high impact velocities than they do at lower ones.

The effects the different EOS have on the temperature generated over the range of impact velocities is now considered. Recall from Section 2.5.0.4, below a certain temperature, T_e, the Sesame EOS of aluminum is made up of two different parts, the zero-Kelvin curve, p_c and the lattice vibration term, p_l. These two partitions are the same partitions that compose the Mie-Gruneisen EOS. This indicates below T_e, the

52
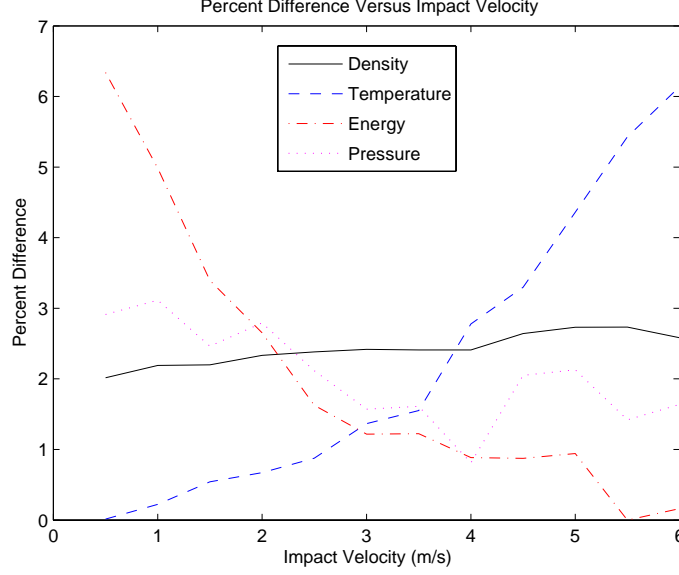
Figure 3.6: Percent Difference in Values Generated with the Sesame and Mie-Gruneisen EOS for Aluminum for Given Impact Velocities

numerical values generated by each EOS should correspond with each other. The numerical answers generated by the two EOS may even match, if particular material values coefficients are used by the Mie-Gruneisen EOS. Above T_e, the Sesame EOS contains a component accounting for the electronic excitation component, p_e. This suggests at temperatures above T_e, the numerical answers generated by the Sesame EOS will diverge from those generated by the Mie-Gruneisen EOS.

For Aluminum, the value of T_e is approximately 940 K [21], which according to Figure 3.5b, occurs between the 3500 $\frac{m}{s}$ and 4000 $\frac{m}{s}$ impact velocities. Figure 3.5b shows, as predicted, at impact velocities below 4000 $\frac{m}{s}$ the answers for the Mie-Gruneisen and Sesame EOS correspond well with each other. It also shows at impact velocities above 4000 $\frac{m}{s}$ the temperatures generated using the Mie-Gruneisen EOS increase at a faster rate than those generated using the Sesame EOS. This trend is also seen in Figure 3.6 where the percent difference between the numerical values of temperature is less than 2% at impact velocities below 4000 $\frac{m}{s}$ while at impact velocities equal to or greater than 4000 $\frac{m}{s}$ the value of percent difference is greater than 2%. Also apparent in Figure 3.6 is an inflection point in the percent difference

53

curve located below the impact velocity of 4000 $\frac{m}{s}$ corresponding to the impact velocity where the electronic excitation contribution to the Sesame EOS begins.

This difference in temperature stems from the electronic excitation term in the Sesame EOS. When the temperature of a material becomes high enough, the electrons become excited and leave their ground states. During this process thermal energy is absorbed, resulting in the lower temperatures produced above T_e when using the Sesame EOS.

Figure 3.5a is used to determine how the densities generated with the different EOS change over the range of impact velocities. In this figure the density generated by the Sesame EOS is represented by a solid line, the densities generated by the Mie-Gruneisen EOS are represented by a dashed line, and a third set of densities represented by the dashed/dotted were generated by translating the Mie-Gruneisen generated densities downward. This third line allows an easier comparison of how the Mie-Gruneisen and Sesame EOS affect the densities generated over the range of impact velocities.

From Figure 3.5a it is apparent that the densities generated begin to diverge from each other right away. To better determine the cause of this, the densities are plotted against the respective temperatures as shown in Figure 3.7. In this figure it is observed that at lower temperatures, values of the densities generated by the different EOS are very close, then at a temperature of just above 420 K the densities begin to diverge. Since 420 K is smaller than the value of T_e for aluminum, it is indicative that the density's divergence is a result of the different theories used to generate the vibrational terms used in the Mie-Gruneisen and Sesame EOS. The density at which this divergence occurs will be referred to as ρ_l and is about 3.2 $\frac{kg}{m^3}$. This density divergence is also apparent in Figure 3.6, showing an inflection point at an impact velocity of about 1500 $\frac{m}{s}$, which produces a density just under ρ_l.

The cause of the divergence at the earlier temperature is explained using Equations (2.69) and (2.70) from Section 2.5.0.4. These equations determine the Debye
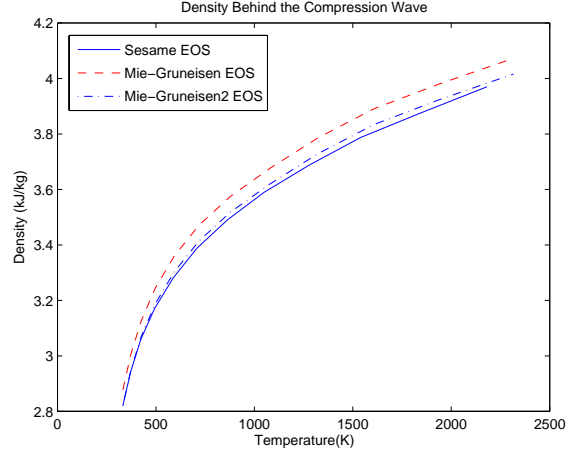
Figure 3.7:   Densities Generated Using the Mie-Gruneisen and Sesame EOS Plotted Against Their Corresponding Temperatures

function and lattice vibration's contribution to the internal energy, respectively . The Debye function is a parameter used in Equation (2.69). The key parameter in the De-bye function is the ratio of the Debye temperature to the absolute temperature, $\frac{\Theta_{ref}}{T}$. When this value is equal to one an inflection point occurs. The Debye temperature for aluminum is 426 K [14], approximately the same temperature where the two EOS begin to diverge. This confirms the divergence is due to the different theories used in development of the lattice vibration contributions and is not numerical.

In CTH internal energy and pressure are state functions of temperature and density, not impact velocity. So, internal energy and pressure need to be plotted against the thermodynamic state parameters of temperature and density before any observations are made about the thermodynamics included in the Sesame or Mie-Gruneisen EOS.

Figure 3.8 shows the values of pressure and internal energy generated with their respective temperatures. Looking at these graphs it is obvious that at a given temperature value, the values of pressure and internal energy generated using the different EOS begin to diverge. In Figure 3.8 it is quite apparent the values of internal energy produced by the two EOS begin to diverge at a temperature of 490 K, the value of T_e for aluminum. For clarification, a heavily dotted line is inserted in Figures

a. Internal Energy   b. Pressure
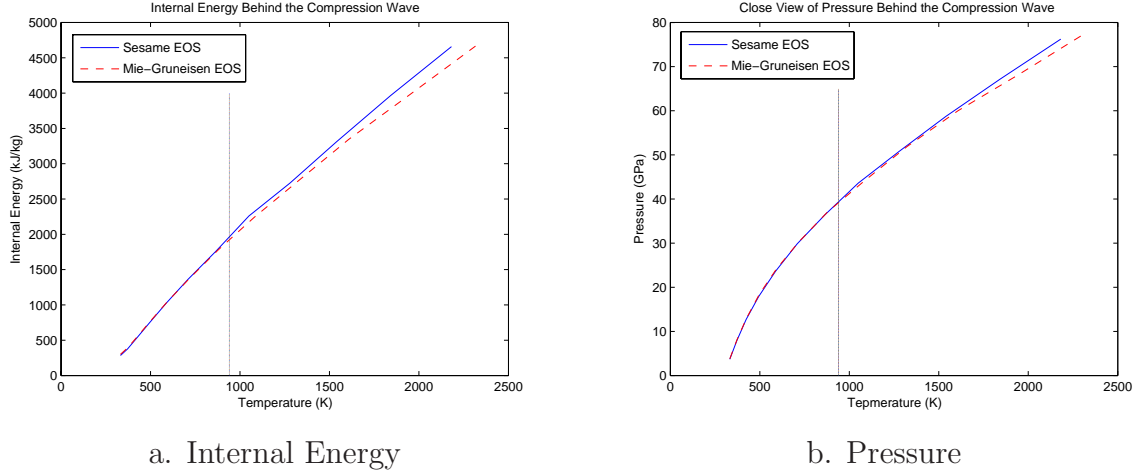
Figure 3.8:   Comparison of Numerical Values of Pressure and Internal Energy Generated by the Sesame and Mie-Gruneisen EOS Graphed with Respect to the Corresponding Temperatures

3.8a and 3.8b at the temperature value of 490 K. However, the temperature where the divergence begins to occur on the pressure graph appears to be greater than the value of 490 K. To determine if this is truly the case, consider Figure 3.9, where it is apparent that up until T_e the values of pressure generated with the different EOS follow the same line, then, as the temperature reaches T_e, the values of the pressures begin to diverge, albeit slowly. This slow rate of divergence would indicate that for temperatures between 940 K and 1400 K the contribution of the electronic excitation term to the Sesame EOS for pressure is minimal and depending on the application, could be assumed negligible when modeling impact phenomena.

Figure 3.10 has the variables of internal energy and pressure graphed against their respective densities to illustrate how the different EOS generate these values over a range of densities. Upon studying Figure 3.10, it is apparent that the values for both internal energy and pressure begin to diverge at the value of ρ_l, and then begin to diverge more at a density of 3.6 $\frac{kg}{m^3}$, which is the density that corresponds to T_e. Again, a heavily dotted line is provided to easily distinguish the position of ρ_l in Figures 3.10a and 3.10b.
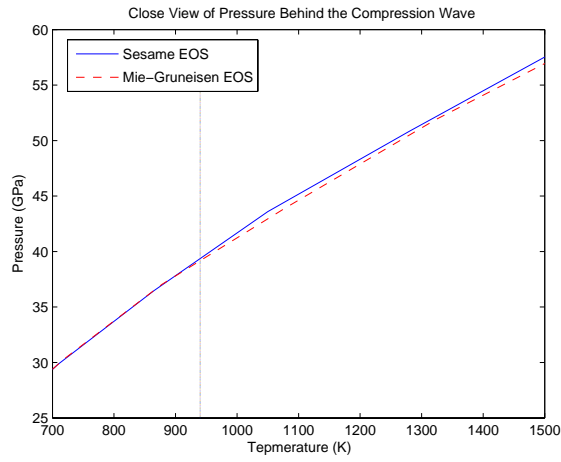
Figure 3.9:   Magnified View of Pressure Versus Temperature for the Results Generated with the Sesame and Mie-Gruneisen EOS

a. Internal Energy   b. Pressure
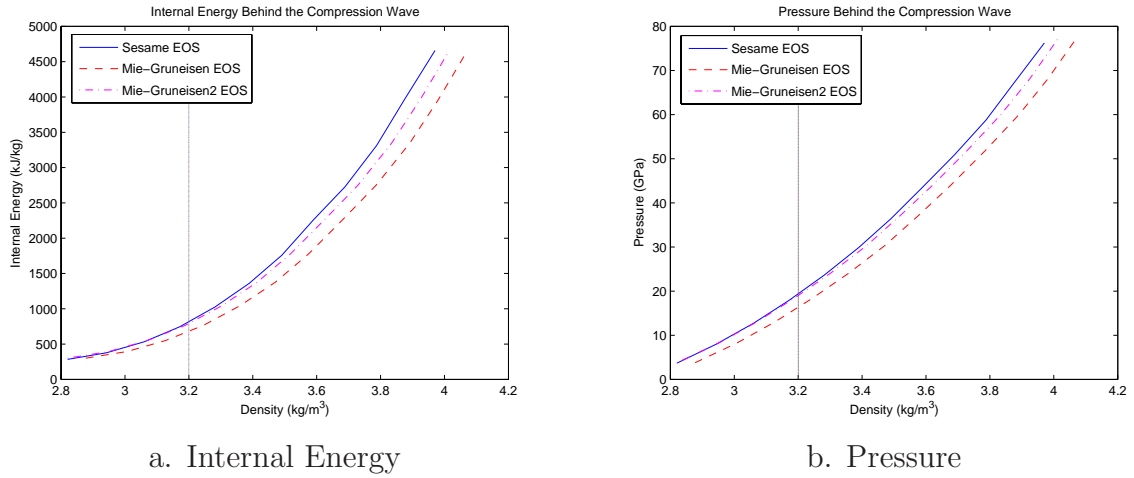
Figure 3.10:   Comparison of Numerical Values of Pressure and Internal Energy Generated by the Sesame and Mie-Gruneisen EOS Graphed with Respect to the Corresponding Densities

It is interesting to note that when compared with respect to temperature as in Figure 3.8, the values of internal energy and pressure do not show the divergence caused by the different lattice vibration theories used in the two EOS. However, this divergence is more obvious when internal energy and pressure are compared using density as is the case in Figure 3.10. This signifies that both the Sesame and Mie-Gruneisen EOS are more sensitive to changes in pressure than they are to changes in temperature.

3.2 Comparison of Sesame and PTRAN EOS Using the Impact of Iron Plates

3.2.1 Procedure and Setup of Iron Impact Simulation. Section 3.1 lays out the method used to compare the Mie-Gruneisen and Sesame EOS for a non-polymorphic material, allowing for a direct comparison between the EOS. Iron, as mentioned in Chapter 2, is a polymorphic material that, when certain pressures are reached, undergoes a solid-solid phase transition from the α iron state to the ϵ iron state. Since the Mie-Gruneisen EOS cannot handle this phase change on its own, the composite EOS, PTRAN, will be compared to the Sesame EOS. Recall, PTRAN uses the α and ϵ Mie-Gruneisen EOS in their respective pressure regions and uses Equation (2.81) (shown here) to solve for the pressure in the region of the phase transition.

$$P(\rho, T, \lambda) = P_T + \beta_T \left(1 - \frac{\rho_T}{\rho}\right) + A_T \left(T - T_0\right) + A_\lambda \lambda$$

Since the purpose of this portion of the investigation is to compare the equilibrium values of the thermodynamic variables generated by the PTRAN EOS, as an equilibrium substitute for the Mie-Gruneisen EOS, the reversible option of the PTRAN EOS is used.

The Sesame and PTRAN EOS will simulate experiments involving the impact of iron, as is detailed in Barker and Hollenbach [5]. Figure 3.11 shows the experimental setup used in their experiments. Figure 3.11 shows the flyer plate on the left,

58
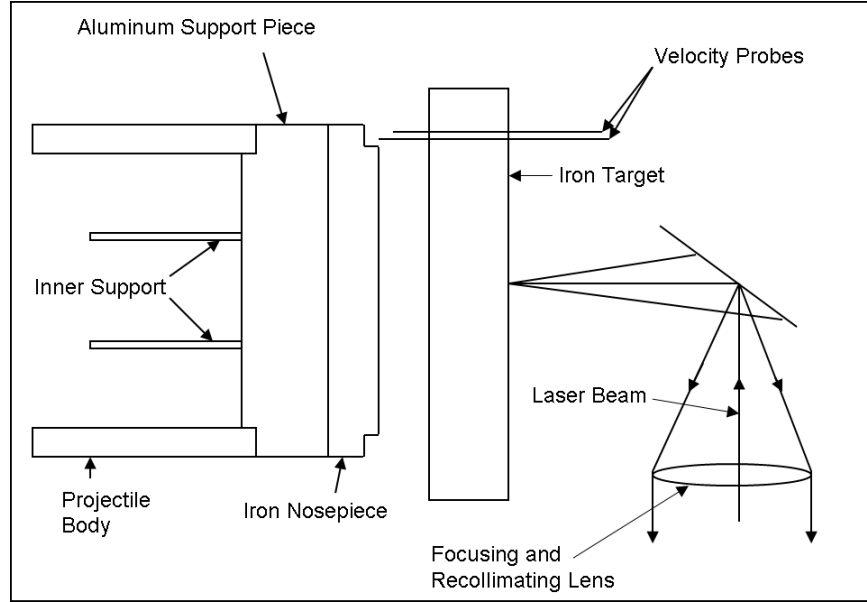
Figure 3.11:   Schematic of Iron Plate Experiment Setup [5]

supported by the projectile body and an aluminum support providing added stability if the thickness of the steel flyer plate is less than 12 mm thick. The target plate is shown on the right along with the velocity probes measuring the the impact velocity protruding from the target plate, and the Velocity Interferometer System for Any Reflector (VISAR) laser system used to measure the peak free surface velocity behind the stress wave. The geometries and impact velocities of the experiments being modeled are given in Table 3.2.

In the experiment, the relatively small thicknesses of the flyer plate and target compared to their diameters, allows the assumption that any effects from the outer surfaces will not affect wave propagation in the centers of the flyer plate and target. This assumption allows the system to be modeled uniaxially. Initially the tracer points used to measure the wave history of the material are placed at the back of the target, matching the experimental setup. However, interference caused by shock waves reflecting off the back of the target stunted the development of the shock waves. To correct this, the location of the tracer point is moved to the center of the target, allowing the compression waves to fully develop.

59

Table 3.2:   Summary of Barker and Hollenbach's Experimental Configurations

Experiment Number	Flyer Thickness (mm)	Target Thickness (mm)	Impact Velocity $(\frac{m}{s})$
1	6.330	6.317	991.6
2	6.350	6.312	1150
3	19.14	15.82	997
4	19.14	15.82	1247
5	6.314	6.314	1292
6	6.337	6.370	1567
7	12.82	19.14	1292
8	12.81	19.13	1557
9	6.337	6.345	1900
10	6.325	6.335	1871
11	6.330	19.07	1887
12	6.327	19.06	1908
13	6.320	6.380	671.1
14	6.335	6.375	612.7
19	19.15	15.76	1396

The geometry and impact velocity of each experiment is numerically simulated in CTH using both the PTRAN and Sesame EOS. The pre-defined Mie-Gruneisen coefficients contained in CTH are used for the modeling of the α and ϵ phases of iron with the PTRAN EOS. The Zerrili-Armstrong constitutive relationship is utilized to model iron's material response to the impacts using the predefined ZA coefficients for iron.

3.2.2   Results Generated by the Numerical Simulation of the Impact of Iron Plates .

3.2.2.1   Comparison of the Equilibrium Values.   In this section CTH results generated using the Sesame and PTRAN EOS, in the numerical simulation of Barker and Hollenbach's experiments are presented and discussed. Then, for further understanding of the differences between the Sesame and PTRAN EOS, additional impact simulations are performed and their results discussed.

Table 3.3:   Barker and Hollenbach's Experimental Results

Impact Velocity $(\frac{m}{s})$	Free Surface Velocity $(\frac{m}{s})$	Specific Volume $(\frac{m^3}{kg})$	Peak Stress (GPa)
612.7	308.35	0.1197	12.1
671.1	337.58	0.1187	13.2
991.6	500.30	0.1123	17.3
997.0	505.83	0.1122	17.3
1150	581.98	0.1108	20.4
1247	633.64	0.1100	22.6
1292	655.17	0.1095	23.6
1292	657.84	0.1096	23.7
1396	711.88	0.1086	26.1
1557	791.56	0.1072	30.1
1567	792.21	0.1071	30.4
1871	949.26	0.1047	38.6
1887	NA	0.1046	39.1
1900	961.54	0.1046	39.6
1908	969.02	0.1045	39.8

Barker and Hollenbach used a VISAR laser to measure the peak free-surface velocity behind the stress wave. Hugoniot relationships were then used to determine the peak stresses and specific volumes behind the stress wave. Table 3.3 [5] contains their measured velocities, calculated stresses and calculated specific volumes. In this section the results in Table 3.3 are compared to numerically generated values using the procedure laid out in Section 3.2.

The numerically generated results using the Sesame and PTRAN EOS are graphed with Barker and Hollenbach's results in Figure 3.12. In Figures 3.12a and 3.12b it is evident that the numerical answers generated with the Sesame and PTRAN EOS both match the free surface velocity and peak stress, which relies heavily on pressure, quite well. However, in Figure 3.12b the values of specific volume generated by the Sesame EOS are lower than those generated by the PTRAN EOS in regions where the impact velocity is high enough to cause the ϵ phase of iron to be present. Since the specific volume is the reciprocal of density, these results indicate the Sesame EOS is

a. Free Surface Velocity

b. Specific Volume
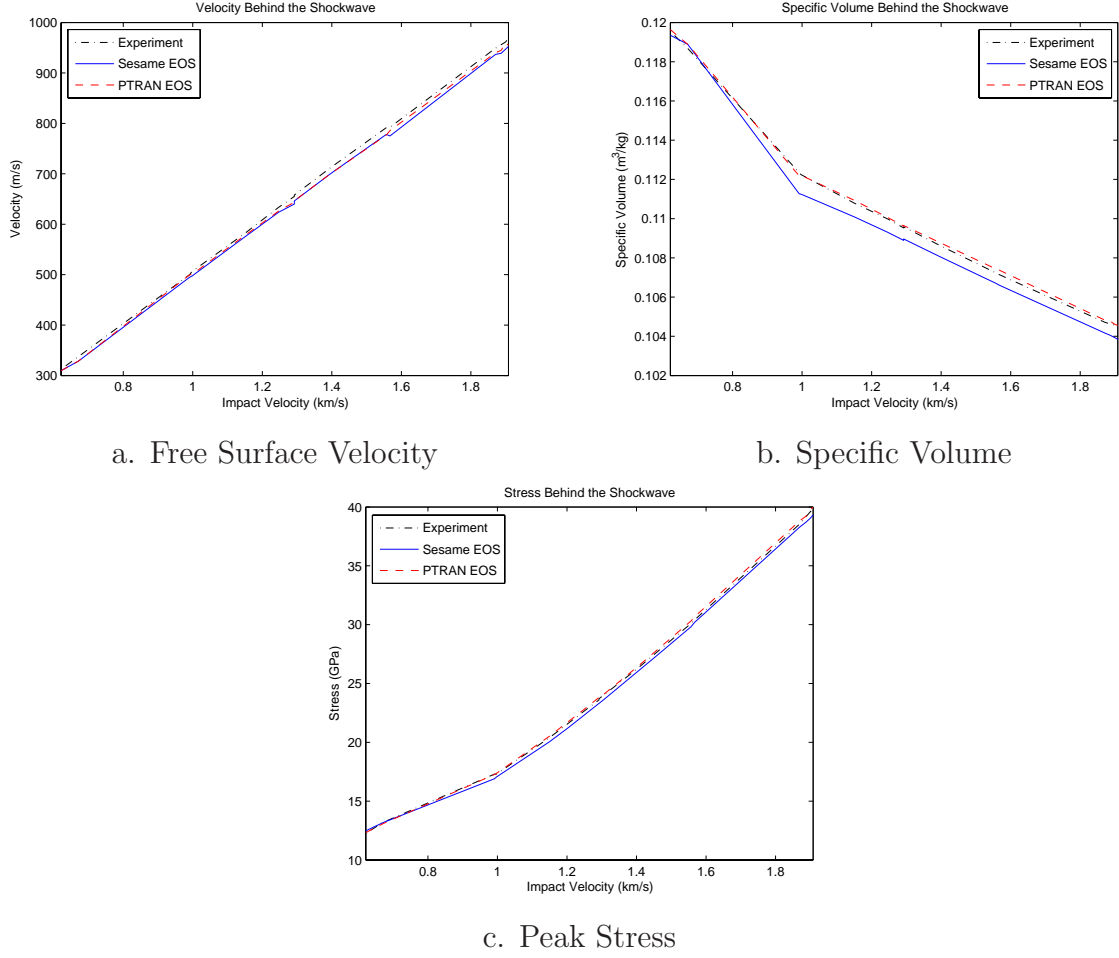
c. Peak Stress

Figure 3.12:   Comparison of Experimental and Numerical Values of Free Surface Velocity, Specific Volume and Peak Stress for Barker and Hollenbach's Impact Experiments with Iron

generating higher values for density than the experimental values and those generated by the ϵ Mie-Gruneisen part of the PTRAN EOS.

Table 3.4 lists the standard deviation of the difference between the experimental results and those generated using the Sesame and PTRAN EOS. The standard deviation of the difference between the Sesame and PTRAN EOS is also included in Table 3.4. By comparing the standard deviations in the table, the ability of the different equations of state to generate answers comparable to experimentally determined values may be determined. From the table it is apparent the particle velocities generated using both EOS compare equally well with the experimentally measured

velocities. However, this is not the case for the numerically generated values of specific volume and stress. According the the table, the values of specific volume and stress generated using the PTRAN EOS are closer to the experimentally determined values than the specific volumes and stresses generated using the Sesame EOS. As previously discussed the large differences in the numerical specific volumes generated occur at impact velocities producing ϵ iron. This is due to different reference densities used by the PTRAN and Sesame EOS for ϵ iron. The difference in the numerical stresses generated are likely caused by the dissimilar ϵ reference densities. Though stress is not a thermodynamic variable and therefore is not found using a thermodynamic state function, the Zerilli-Armstrong constitutive relationship is a function of temperature, which relies on the density for its generation. Thus the numerical stresses rely on a thermodynamic parameter and are affected indirectly by the difference in densities.

Table 3.4: Comparison of the Standard Deviations Between the Experimental Values, Values Generated Using the Sesame and Mie-Gruneisen EOS for the Impact of Iron

State Variable	SD of Sesame EOS & Experiment	SD of PTRAN EOS & Experiment	SD of Sesame EOS & PTRAN EOS
Velocity $\left(\frac{m}{s}\right)$	4.3977	4.6126	4.0316
Volume $\left(\frac{m^3}{kg}\right)$	$3.0105 * 10^{-4}$	$1.0207 * 10^{-4}$	$2.4252 * 10^{-4}$
Stress (GPa)	0.2005	0.1081	0.2504

The numerical values of temperature and internal energy generated by the different EOS can only be compared to each other, because Barker and Hollenbach did not provide experimentally determined values of these variables for comparison. The values of temperature and internal energy are plotted against their respective impact velocities in Figure 3.13. In Figure 3.13a its apparent the values for internal energy generated by different EOS are close in value. However, the temperatures values generated using different EOS in Figure 3.13b are significantly different. Figure 3.13b also appears to show the Sesame EOS generated temperature values starting to diverge from the PTRAN EOS values at the impact velocity of 1557 $\frac{m}{s}$, corresponding to a temperature of 511.2 K. These results agree with the Sesame EOS for iron, which has

a. Internal Energy   b. Temperature
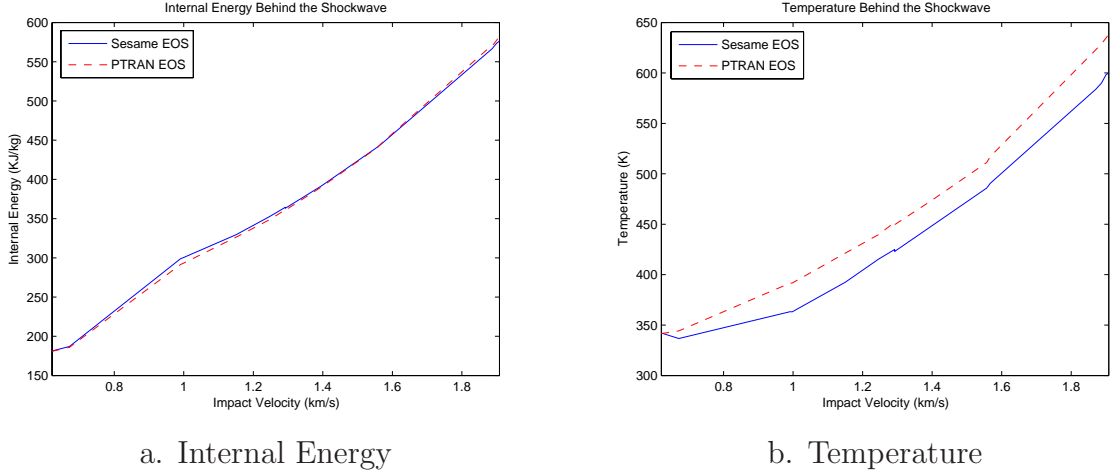
Figure 3.13:   Comparison of Numerical Values of Temperature and Internal Energy
for Barker and Hollenbach's Impact Experiments with Iron

a T_e of 500 K. However it is difficult to determine if this is actually the case, because
the maximum values of the temperatures generated by the PTRAN and Sesame EOS
are 638 K and 600 K, respectively, which are not that much greater than iron's T_e.

Overall the numerical values generated using both the Sesame and PTRAN
EOS compare well with the experimental results. The exception being difference in
the density values generated with the Sesame EOS. The densities produced by CTH
using the Sesame EOS in the aluminum impacts, are different than those generated
using the Mie-Gruneisen or PTRAN EOS. However in both cases the pressures and
internal energies generated by the different EOS are similar. This suggests that the
"more accurate" EOS depends on the application, meaning if the pressures generated
are the important output, either EOS may be used. However, if knowing the density
is important, the selection of EOS is more critical. It also underlines the importance
of validating numerically generated solutions to assure the correct EOS is being used
for the desired application. For example, in the case of the iron experimental impacts,
the values of density generated with the Mie-Gruneisen EOS provide the better match
to the experimental values. This indicates the PTRAN EOS is the EOS of choice for
iron impact simulations at the velocities used by Barker and Hollenbach.

64

In order to determine more about the differences between the PTRAN and Sesame EOS additional data points are needed. To obtain these, additional runs are performed at impact velocities of 400, 500, 2500, 3000, 3500, and 4000 $\frac{m}{s}$. The impact values of 400 and 500 $\frac{m}{s}$ are impact velocities where the pressures generated do not cause the $\alpha \rightarrow \epsilon$ phase transition. These values compliment the experimental impact velocity of 612.7 $\frac{m}{s}$ by providing more data points where only the α phase of iron is present. The geometry used in the 612.7 $\frac{m}{s}$ is used for the impact velocities of 400 $\frac{m}{s}$ and 500 $\frac{m}{s}$. The temperatures produced in the simulation of Barker and Hollenbach's experiments using either EOS are not much higher than iron's T_e value of 500 K. The impact velocities of 2500, 3000, 3500 and 4000 $\frac{m}{s}$ are meant to produce significantly higher temperatures than 500 K, providing clarification of how the different EOS act at temperatures higher than T_e.

Figure 3.14 presents the values of density, temperature, internal energy and pressure generated by the Sesame and PTRAN EOS for the whole range of impact velocities.

There are several observations that can be made while studying Figure 3.14. The first is the similar results generated by each EOS for the values of pressure and internal energy. This is consistent with what is seen when comparing the Mie-Gruneisen and Sesame EOS in aluminum impact tests. In Figure 3.14b it is also apparent that at temperatures above 500 K (corresponding with impact velocities greater than 1557 $\frac{m}{s}$), the temperature values generated by the Sesame and PTRAN EOS begin to diverge. As is the case in the Sesame EOS for aluminum, the lower temperature generated in the Sesame EOS is due to the thermal energy being absorbed as the iron's electrons become excited and leave their ground states. Also apparent in Figure 3.14a is the difference in the densities generated for ϵ iron. This agrees with the results seen in Figure 3.12a, however due to the greater range of density values in Figure 3.14a it appears the density values generated by the different EOS correlate better than originally thought. It may be possible to force the density values generated with the Mie-Gruneisen EOS to match those generated by the Sesame EOS for the ϵ iron
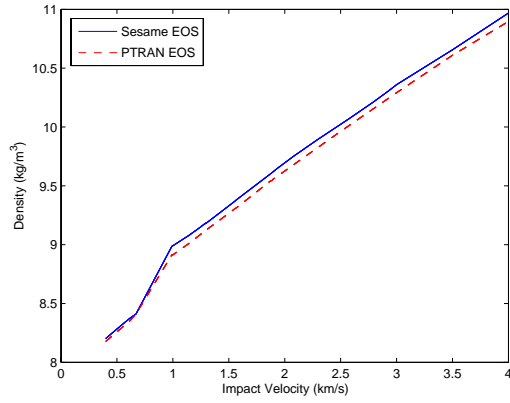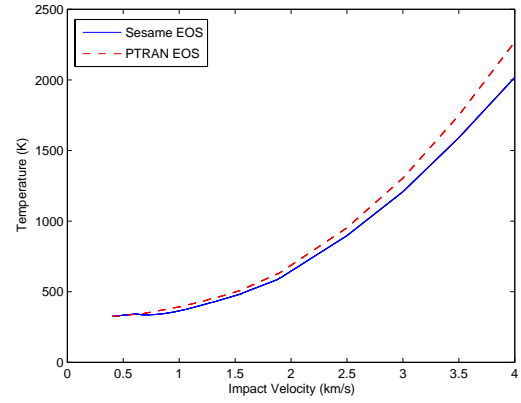
a. Density

b. Temperature
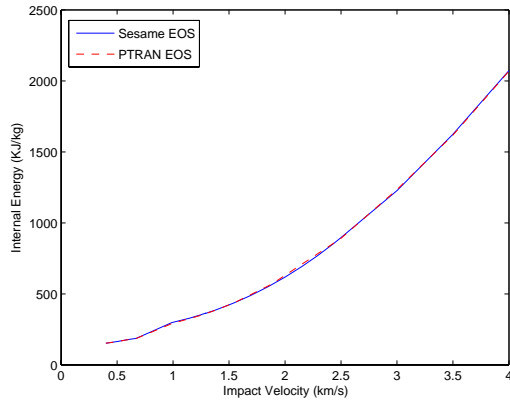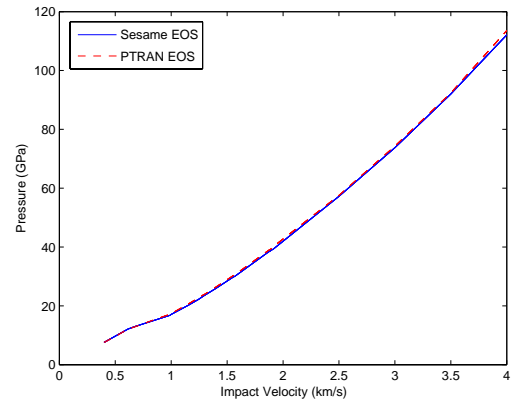
c. Internal Energy

d. Pressure

Figure 3.14: Comparison of Numerical Values of Density, Temperature, Pressure and Internal Energy Generated by the Sesame and PTRAN EOS

producing impact velocities. This however, will cause the Mie-Gruneisen EOS to produce different pressures and internal energies, emphasizing the need to perform validation runs to assure the EOS chosen for use in numerical simulations is the appropriate one.

Figures 3.14a, 3.14c and 3.14d also contain $\alpha \rightarrow \epsilon$ phase transition regions in the curves generated, denoted by regions containing several discontinuities. According to these graphs, the impact velocities causing the phase change lie between 612.7 $\frac{m}{s}$, which is the last impact velocity resulting in the pure α phase, through the first impact velocity resulting in a fully developed ϵ phase at 997 $\frac{m}{s}$.

To provide more information on how well the numerical values of the thermodynamic variables correlate with each other, Figure 3.15 shows the percent difference between the values of the thermodynamic variables generated using the two EOS. Figure 3.15 shows that the values of density, internal energy and pressure generated by the different EOS correlate well with each other throughout the entire range of impact velocities, meaning the percent difference is never greater than 2%. This indicates either the PTRAN or Sesame EOS will produce acceptable value of internal energy, density and pressure when used to model impact phenomena. The percent difference curve for temperature, represented by a dashed line, shows a great difference in the values of the temperatures generated at impact velocities producing ϵ iron. The percent difference then jumps again after iron's T_e value of 500 K is reached at impact velocities greater than 1557 $\frac{m}{s}$. So, if the values of temperatures generated in the simulation of impacts are of great importance, the choice of EOS is critical. If high temperatures are expected to be produced in the impacts, the use of the Sesame EOS is necessary, because it accounts for the thermal effects from the electronic excitation while the Mie-Gruneisen and therefore the PTRAN EOS do not.

Figure 3.16b shows the temperatures generated by both EOS are affected by the phase transition. The figure also illustrates the temperatures generated by the Sesame EOS in the ϵ region are lower than the temperatures generated by the PTRAN EOS.

67
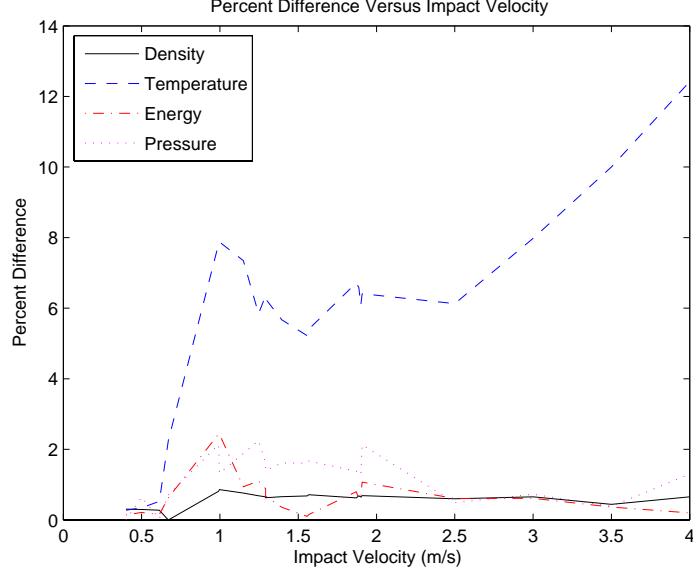
Figure 3.15: Percent Difference in Values Generated with the Sesame and Mie-Gruneisen EOS of Iron for Given Impact Velocities

This agrees well with the percent difference curve for temperature in Figure 3.15. There is no theoretical reason for the dissimilar values of temperature generated by the two EOS for the ϵ phase of iron. This difference is most likely caused by the use of dissimilar material properties values used by the different EOS for the ϵ iron phase.

As previously mentioned, impact velocity is not a thermodynamic state variable, so further investigation of the Sesame and PTRAN EOS requires the relationships between the thermodynamic variables of temperature, density, pressure and internal energy be investigated. Figure 3.17 contains the values of density, pressure, and internal energy generated by the Sesame and PTRAN EOS graphed against the corresponding values of temperature.

Figures 3.17a, 3.17b and 3.17c all show the respective values of density, pressure and internal energy for the different equations of state diverging at the T_e value of 500 K, represented by a heavily dotted line. The electronic excitation term included in the Sesame EOS accounting for the difference. In the density graph (Figure 3.17a), a separate divergence precedes the divergence at T_e, this divergence is due to the dissimilar densities of the ϵ phase of iron used by the two EOS. This differs with
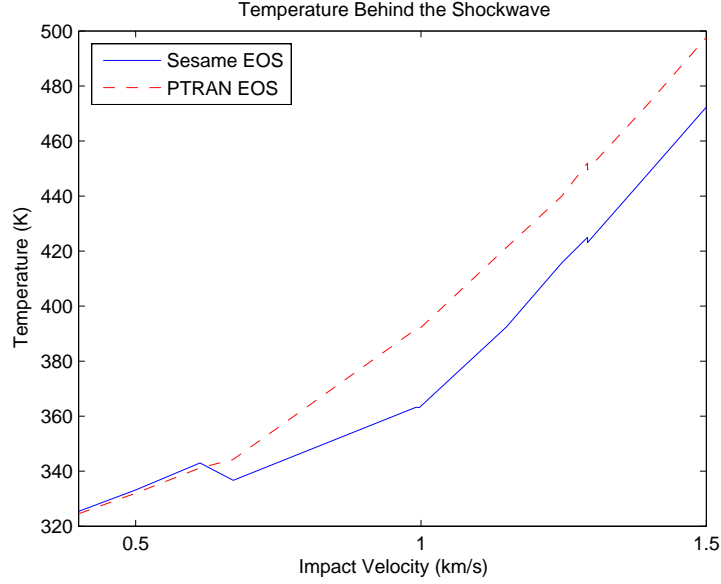
Figure 3.16:   Close-up of Temperature Values Generated by the Sesame and PTRAN EOS Clearly Illustrating the Phase Transition in Iron

the cause of the early divergence of the densities seen in aluminum, which occurs at the Debye temperature, the material property at which, the material lattices are vibrating at the maximum frequency allowed by the Debye Distribution [33]. The Debye temperature does not have an impact on the iron plate impact simulations because neither iron phase ever cross their respective Debye temperatures. The Debye temperature of α iron in the Sesame EOS is 425 K, but the maximum temperature for α iron seen in the impact simulations is 343 K, occurring at an impact velocity of 612.7 $\frac{m}{s}$. This indicates the α iron phase never reaches its Debye temperature. The ϵ phase of iron has a Debye temperature of 385 K, which is reached just as the $\alpha \rightarrow \epsilon$ phase transition is completed. This makes it difficult to determine if reaching the Debye temperature has any impact on the thermodynamic properties generated by the two EOS. If it does have an impact, it is difficult to determine what percentage of the difference is caused by reaching ϵ iron's Debye temperature and what percent of the difference is caused by the different material properties used in the PTRAN and Sesame EOS for ϵ iron.
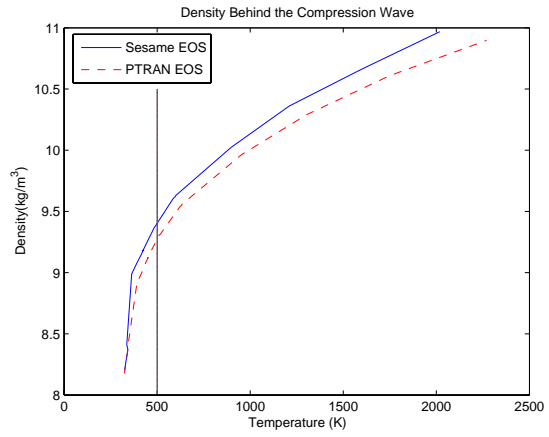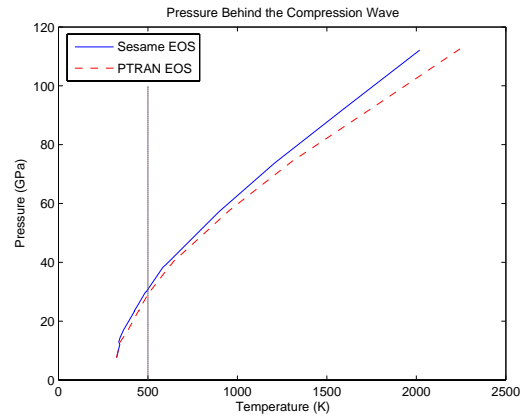
a. Density

b. Pressure
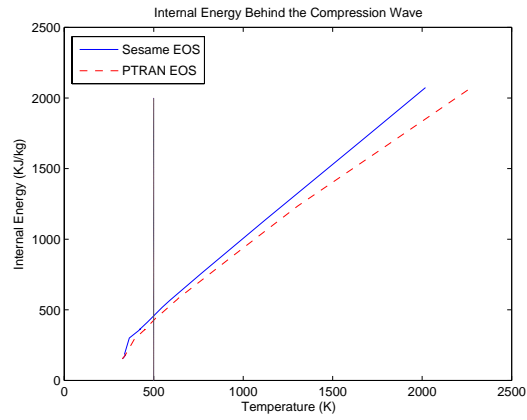
c. Internal Energy

Figure 3.17:   Comparison of Density, Pressure and Internal Energy generated by the PTRAN and Sesame EOS with Respect to Temperature

Internal Energy Behind the Compression Wave

Pressure Behind the Compression Wave

a. Pressure
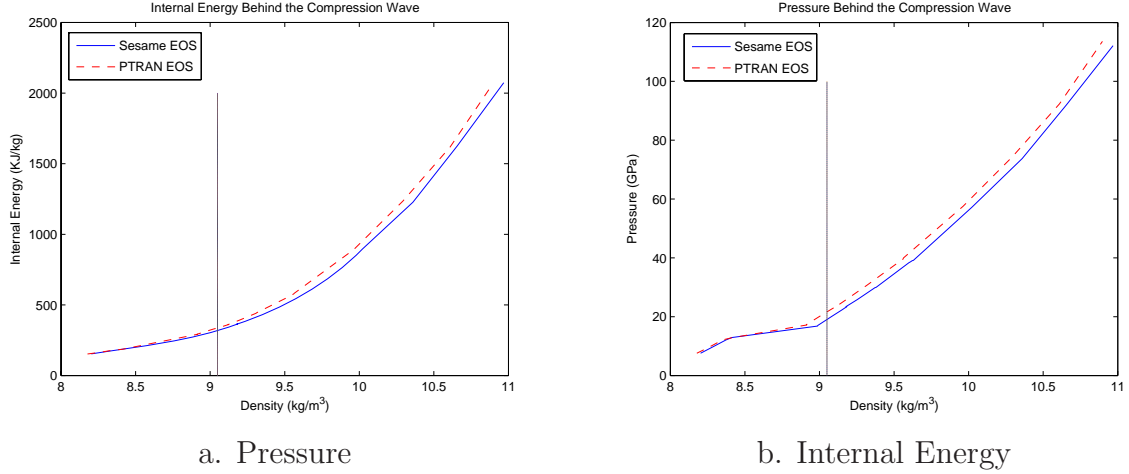
b. Internal Energy

Figure 3.18:   Comparison of Pressure and Internal Energy generated by the PTRAN and Sesame EOS with Respect to Density

Figure 3.18 has the values of internal energy and pressure graphed against the corresponding values of density. This figure shows values generated for internal energy and pressure diverging at density values corresponding with the end of the $\alpha \rightarrow \epsilon$ phase transition. This is consistent with the significant dissimilarities between the densities generated with the different EOS shown in Figures 3.14a and 3.17b. Figures 3.14a also show the density corresponding with the Debye temperature of ϵ iron, illustrating the difficulty in determining if an additional divergence is occurring in this region.

3.3   Irreversible Thermodynamic Effects

In the previous sections the reversible option of PTRAN EOS is utilized to allow for a comparison of the equilibrium thermodynamics included in the Mie-Gruneisen and Sesame EOS. In this section the irreversible option of the PTRAN EOS is used, and the results obtained are compared to those generated by the reversible form of the PTRAN and the Sesame EOS. The purpose of this investigation is to use the irreversible PTRAN EOS to determine if the the Sesame EOS is able to account for any irreversibilities due to phase changes.

3.3.1 Procedure for Determining the Ability of the Sesame EOS to Generate Irreversibilities. The PTRAN EOS with the reversible option is used in the simulation of uniaxial impacts for three different impact velocities , 1557, 2500 and 3500 $\frac{m}{s}$. The impact geometries used are the same as those used in Section 3.2 for the impact scenarios with the corresponding impact velocities. Table 3.5 contains the respective geometries for the different impact velocities. The only difference in these simulations is the use of the irreversible PTRAN option, everything else in the input deck remains the same.

Table 3.5:   Impact Velocities and Geometries for Irreversible PTRAN Investigation

Impact Velocity $\left(\frac{m}{s}\right)$	Flyer Thickness (mm)	Target Thickness (mm)
1292	6.314	6.314
2500	6.327	19.06
2500	6.327	19.06

3.3.2 Analysis of the Determining the Ability of the Sesame EOS to Generate Irreversibilities. Tables 3.6, 3.7 and 3.8 contain the thermodynamic values of pressure, temperature, internal energy and density generated using the irreversible PTRAN EOS, the reversible PTRAN EOS and the Sesame EOS for each of the impact velocities used. These values are measured at a region well behind the front of the compression wave to assure the respective values are equilibrium values. Comparing the thermodynamic values generated behind the shock determines if the irreversibility effects of the irreversible PTRAN EOS affect the equilibrium thermodynamics variables generated by the EOS.

Table 3.6 contains the thermodynamic values generated at an impact velocity of 1292 $\frac{m}{s}$. The values of internal energy and pressure generated by the three EOS are all within 1% of each other, while the pressures generated are all within 2% of each other. The temperatures generated with the different EOS represent the only thermodynamic variable where all the values generated are not within a few percent

72

or each other. This discrepancy is caused by the temperature generated using the irreversible PTRAN EOS, which is 5.8% larger than the temperatures generated using the reversible PTRAN and Sesame EOS.

From Tables 3.7 and 3.8 it is ascertained the values of pressure, internal energy and density are all within 1.1% of each other. Again the temperatures generated at the velocities of 2500 and 3500 $\frac{m}{s}$ are the only thermodynamic variables with a span greater than 2% (8.5% for the impact velocity of 2500 $\frac{m}{s}$ and 10.1% at an impact velocity of 3500 $\frac{m}{s}$). In these cases however, the rouge temperatures are generated by the Sesame EOS and are due to the inclusion of the electronic excitation term included in the Sesame EOS.

Unfortunately the cause of the high temperature generated by the irreversible PTRAN EOS cannot be satisfactorily explained. High temperature value aside, the irreversible PTRAN EOS generates equilibrium thermodynamic values comparable to the reversible PTRAN EOS, and compares well with the Sesame EOS also.

Table 3.6: Thermodynamic Variables Generated by the PTRAN EOS with Reversible and Irreversible Options and Sesame EOS for a Uniaxial Impact with an Impact Velocity of 1292 $\frac{m}{s}$

EOS	Pressure	Temperature	Internal Energy	Density
	(GPa)	(K)	$\left(\frac{kJ}{kg}\right)$	$\left(\frac{kg}{m^3}\right)$
PTRAN irreversible	23.75	451.6	361.96	9.121
PTRAN reversible	23.82	425.2	361.25	9.123
Sesame	23.43	425	364.5	9.183

One of the purposes of this thesis is to determine if the Sesame EOS is capable of modeling any irreversible thermodynamics whatsoever. According to the results generated in the simulations of uniaxial impacts involving aluminum, it is apparent no irreversibilities are included in the Sesame EOS. However, by modeling a polymorphic material, such as iron, an irreversibility is introduced in the phase transition. Looking at the equilibrium values generated by the reversible and irreversible PTRAN EOS and the Sesame EOS, no conclusions about the irreversible nature of the Sesame EOS

Table 3.7: Thermodynamic Variables Generated by the PTRAN EOS with Reversible and Irreversible Options and Sesame EOS for a Uniaxial Impact with an Impact Velocity of 2500 $\frac{m}{s}$

EOS	Pressure	Temperature	Internal Energy	Density
	(GPa)	(K)	$\left(\frac{kJ}{kg}\right)$	$\left(\frac{kg}{m^3}\right)$
PTRAN irreversible	57.69	953.8	900	9.976
PTRAN reversible	57.5	952.4	891.67	9.963
Sesame	57.22	897.4	897.12	10.023

Table 3.8: Thermodynamic Variables Generated by the PTRAN EOS with Reversible and Irreversible Options and Sesame EOS for a Uniaxial Impact with an Impact Velocity of 2500 $\frac{m}{s}$

EOS	Pressure	Temperature	Internal Energy	Density
	(GPa)	(K)	$\left(\frac{kJ}{kg}\right)$	$\left(\frac{kg}{m^3}\right)$
PTRAN irreversible	93	1750	1625	10.611
PTRAN reversible	92.35	1750.4	1619	10.610
Sesame	92	1590	1625	10.656

may be made. So, now the ability of the different EOS to model the history of a compression wave is investigated. Figure 3.19 shows the wave histories generated using the three EOS discussed in this section.

Figures 3.19a and 3.19b show the irreversible and reversible forms of the PTRAN EOS. Comparing these two figures it is noticed the front portion of the compression wave is not affected by the irreversibility option. The back of the compression waves are formed very different, however. The back of the compression wave generated with the irreversible option on shows a rounded portion where the $\epsilon \rightarrow \alpha$ phase change takes place followed by a sloped portion formed by the rarefaction wave. This contrasts with the compression wave generated using the reversible PTRAN EOS showing a flat $\epsilon \rightarrow \alpha$ region and a sharp drop off in the region formed after the phase change formed by a rarefaction wave.
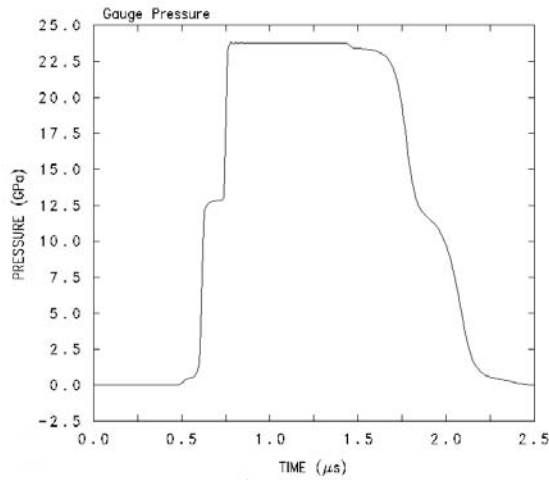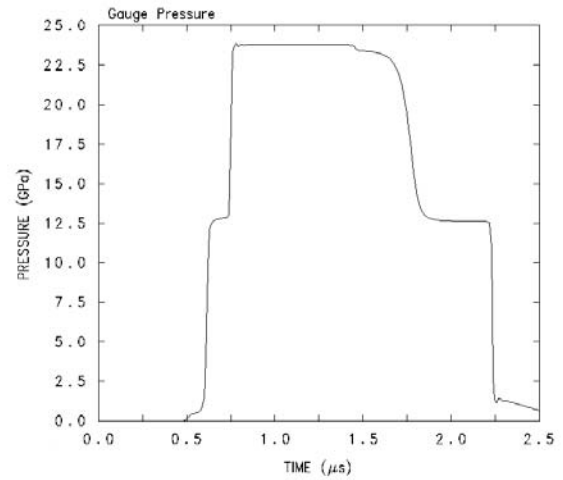
a. Irreversible PTRAN EOS   b. Reversible PTRAN EOS
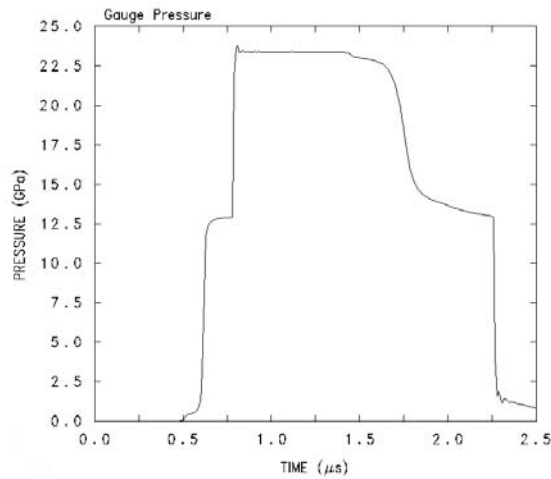
c. Sesame EOS

Figure 3.19:   Comparison of Sesame EOS to Reversible and Irreversible Forms of the PTRAN EOS
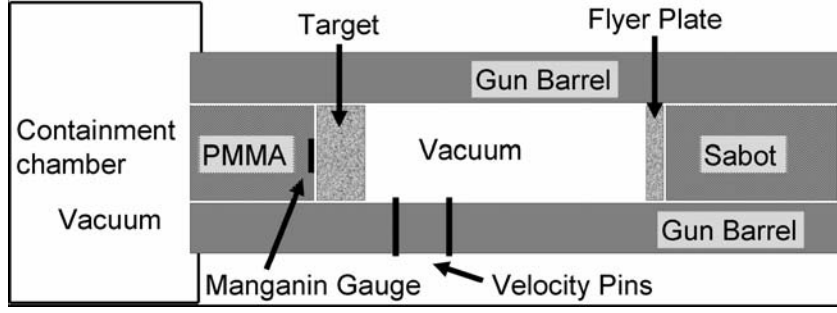
Figure 3.20:   Schematic of Flyer Plate Test Setup

The compression wave history generated with the Sesame EOS has the same drop off in the region behind the $\epsilon \rightarrow \alpha$ phase transition seen on the compression wave generated using the reversible PTRAN EOS. However, in the region of the $\epsilon \rightarrow \alpha$ transition it is rounded, similar to that of the irreversible PTRAN EOS generated compression wave. This signifies that the Sesame EOS, in spite of using an equilibrium approach in determining the thermodynamics of the phase transition region by selecting the phase with the lower Gibbs free energy, is capable of modeling irreversible thermodynamics in the region of a phase change.

3.4   Flyer Plate Experiment

3.4.1   Procedure and Experimental Setup.   While Cinnamon [9] was conducting his research on gouging for the HHSTT, flyer plate tests were performed at the University of Dayton Research Institute (UDRI) to assist in the determination of the Zerrili-Armstrong (ZA) coefficients used to model the material response of 1080 steel. A schematic of the test setup is shown in Figure 3.20, which shows the flyer plate on the right attached to a sabot for support. The target plate is on the left with a stress gauge between it and a layer of PMMA. The impact velocity is measured using velocity pins located just to the right of the target and are shown protruding through the barrel of the gas gun. To determine the correct ZA coefficients for 1080 steel, Cinnamon produced a uniaxial flyer plate model in CTH using the Sesame EOS of iron and manually specifying the ZA coefficients for 1080 steel. He then ran the simu-

lations while modifying the values of the ZA coefficients, until the numerical answers produced by CTH matched the experimental data.

In this investigation, the CTH model used by Cinnamon is run using the α iron Mie-Gruneisen EOS, the reversible and irreversible forms of the PTRAN EOS and the Sesame EOS. For alloy metals such as steel, it is an accepted approximation to model the alloy using the EOS for it's prime constituent, in this case iron [43]. This corresponds to what Cinnamon did in his simulation, and is the method used in this investigation. Due to the relatively low impact velocity, only the α iron Mie-Gruneisen EOS coefficients are used to simulate 1080 steel impacts.

The ZA coefficients for 1080 steel used in this simulation are located in Table 3.9. These are the coefficients determined by Cinnamon to accurately model the reaction of 1080 steel when subjected to high velocity impacts.

Table 3.9:   Zerilli-Armstrong Coefficients for 1080 Steel

Coefficient	A	c_1	c_2	c_3	c_4	c_5	n
Value	0.825	4.0	0	160.0	12.0	0.266	0.089

The different EOS will be used to simulate the impact of 1080 steel at an impact velocity of 891 $\frac{m}{s}$. The results obtained from these simulation will then be compared. The tracer point used to generate the stress wave histories is located in the target 6.25 mm away from the point of impact. To avoid any interference from wave reflections at the iron/PMMA interface, the PMMA will be modeled as iron. This also matches the methodology used by Cinnamon, and is justified because the PMMA is located behind the tracer point and has no effect on the development of the stress wave.

3.4.2   Results of Flyer Plate Experiment.   Figure 3.21 contains the stress waves generated in the CTH simulation of the flyer plate experiments performed by Cinnamon, using the α Mie-Gruneisen, reversible and irreversible PTRAN EOS and the Sesame EOS. The stress wave measured in the lab is located in Figure 3.22,

superimposed on the CTH generation of the stress wave Cinnamon used to determine the correct ZA coefficients for 1080 Steel [9].

Upon study, all the EOS correctly generate the value of the Hugoniot Elastic Limit (HEL) and are able to model the elastic precursor. This, however is the only similarity between the numerical results generated with the Sesame, PTRAN and α Mie-Gruneisen EOS. There are two reasons the single phase Mie-Gruneisen EOS is able to model accurately model the value of the HEL. The first reason is the HEL is a material response modeled by the constitutive equations and therefore is not determined by the EOS. The other reason is the value of the HEL is well within the limits of the α phase of iron.

The differences in the results generated using the Mie-Gruneisen EOS as opposed to those generated by the Sesame and reversible PTRAN EOS will be examined first. The two major differences in the Mie-Gruneisen generated results as opposed to those generated with the Sesame or PTRAN EOS include, the higher value of peak stress generated with the Mie-Gruneisen EOS and the relatively small depth to the stress wave generated.

The lack of depth in the stress wave is caused by a rarefaction wave relieving the stress wave sooner with the Mie-Gruneison generated results than the Sesame or PTRAN results. The velocity of a shock wave propagating through a material is found using the linear equation, Eqn 3.2 [38]:

$$U_s = C_0 + Sv \tag{3.2}$$

where U_s is the shock wave velocity. U_s is linearly related to the velocity of the material particles located behind the shock wave. Table 3.10 gives the values of the peak particle velocity found with each EOS. Table 3.10 shows the peak particle speed generated with the Mie-Gruneisen is approximately 32% higher than those generated with the other EOS. This leads to a higher shock wave velocity causing the rarefaction
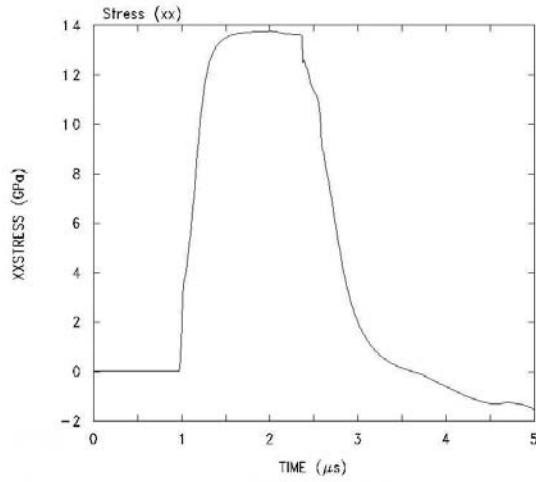
a. Reversible PTRAN EOS
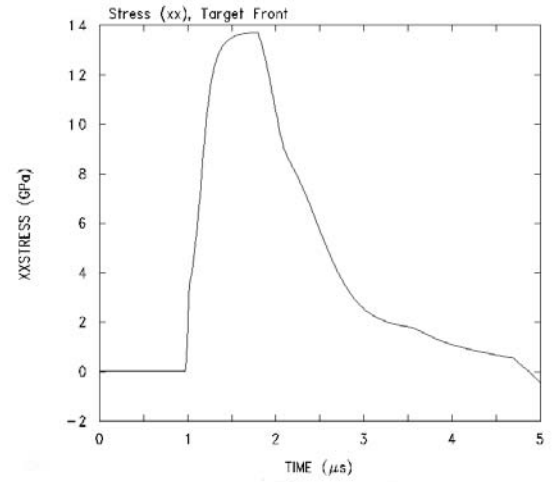
b. Irreversible PTRAN EOS
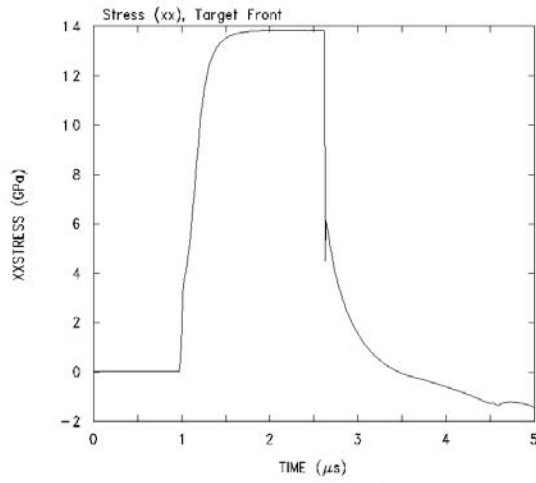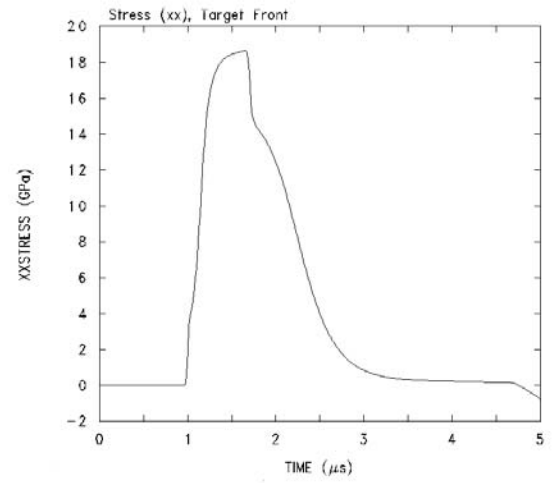
c. Sesame EOS

d. Mie-Gruneisen EOS for the α Iron Phase

Figure 3.21:   Comparison of Stress Waves Generated with the Mie-Gruneisen, PTRAN and Sesame EOS
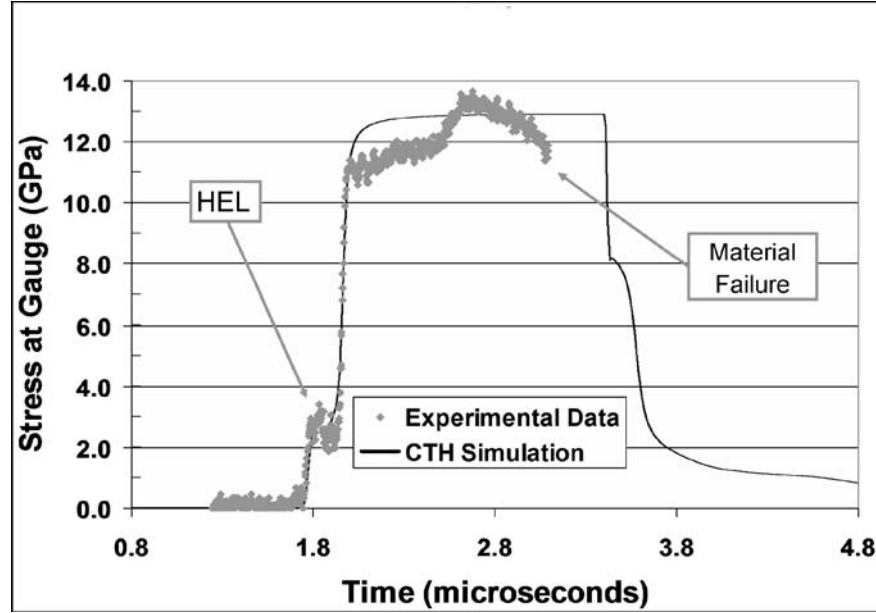
Figure 3.22:   UDRI Results Superimposed on Cinnamon's CTH Generated Stress
Wave

wave to reach the location of the tracer point in less time resulting in the smaller depth
of the Mie-Gruneisen generated stress wave.

Table 3.10:   Peak Particle Velocities Generated by Different EOS

EOS	Velocity ($\frac{m}{s}$)
Mie-Gruneisen	738.5
Sesame	334.4
Reversible PTRAN	331.7
Irreversible PTRAN	329.4

The difference in peak stress value is caused by the inability of the Mie-Gruneisen
EOS to handle the phase change of iron. Equation (2.15) in Section 2.2.2 shows that
the hydrostatic pressure produced in an impact is a major contributor to the overall
value of stress seen by the material. The peak values of the pressures generated with
each EOS are given in Table 3.11. The values given in Table 3.11 show that the
pressures generated with the Sesame and PTRAN EOS are approximately equal to
the transition pressure of iron. The Mie-Gruneisen EOS does not account for iron's

80

phase transition and generates a higher value of peak pressure, resulting in a higher peak stress value.

EOS	Pressure (GPa)
Mie-Gruneisen	17.6
Sesame	12.9
Reversible PTRAN	12.8
Reversible PTRAN	12.7

Table 3.11:   Peak Pressures Generated by Different EOS

Comparing the stress waves generated using the reversible and irreversible forms of the PTRAN EOS shown in Figures 3.21a and 3.21b respectively it is apparent the reversible - irreversible option in the PTRAN EOS may have a major impact on the results generated. The reversible form of the PTRAN EOS generates a stress wave with more depth than the stress wave produced using the irreversible form. Unlike the difference seen between the Mie-Gruneisen and Sesame and reversible PTRAN EOS generated stress waves, there is no obvious physical reason for the different shape of the stress wave generated by the irreversible PTRAN EOS. Meaning the velocities behind the stress waves generated using the different forms of the PTRAN EOS compare very well (331.7 $\frac{m}{s}$ generated with the reversible form compared to 329.4 $\frac{m}{s}$ produced by the irreversible form), so the plastic wave velocities should also compare well by generating stress waves of equal depth. In spite of the different stress wave shapes, the magnitude of the peak stress generated with the irreversible PTRAN EOS is comparable to that generated using the reversible form of the PTRAN EOS, 12.7 and 12.8 GPa respectively. The results generated using the two PTRAN EOS indicate care must be used in the use of the PTRAN EOS in the modeling of impact events causing phase transitions.

Finally, it has been determined the Sesame and reversible PTRAN EOS appear to generate similiar results. To verify this, the results generated using the two EOS are compared to the experimental results in Figure 3.22. Looking at the different results, it is apparent that both the Sesame and reversible PTRAN EOS generate

reasonable stress wave histories, both in peak stress value, just below 13 GPA, and correct wave depth, around 2 μs.

IV. Validation of the Vanderhyde Finite Volume Code (VFVC)

4.1 Validation of VFVC Using Aluminum

4.1.1 Procedure. The validation of the VFVC consists of simulating the impact of aluminum using the VFVC and comparing the answers generated with answers generated by CTH using both the Mie-Gruneisen and Sesame EOS. The simulation consist simulating the same set of impact velocities and geometries used in Section 3.1. A cell width of 0.0018 cm is used in the validation using aluminum. The VFVC also requires additional material properties in order to model aluminum's constitutive response to impact. These additional parameters are given in Table 4.1, where Y is the value of aluminum's yield stress, e_0 is the initial value of the specific internal energy of iron, G is the shear modulus of aluminum and H is the linear work hardening rate.

Table 4.1: Additional Material Parameters Needed by the Eulerian Code

Coefficient	Y	e_0	G	H
Value	34.747 MPa	268125 $\frac{J}{kg}$	25 GPa	120 MPa
Source	[12]	[21]	[4]	[31]

For every simulation, the VFVC produces two output files. One shows what is happening over the region of the entire grid, while the other output file provides the history of a single point over the run time of the simulation. A post processing tool written in Matlab then reads the output files and presents the data in an intelligible manner.

The results generated by the VFVC are then compared to the numerical data generated by CTH using both the Sesame and Mie-Gruneisen EOS.

4.1.2 Validation of the Finite Volume Code with Impacts Between Aluminum Plates. Figure 4.1 shows the thermodynamic properties behind the shockwave generated by the VFVC compared to those generated with the Mie-Gruneisen and Sesame EOS in CTH. Figure 4.1a contains an additional curve that consists of the

a. Density

b. Internal Energy
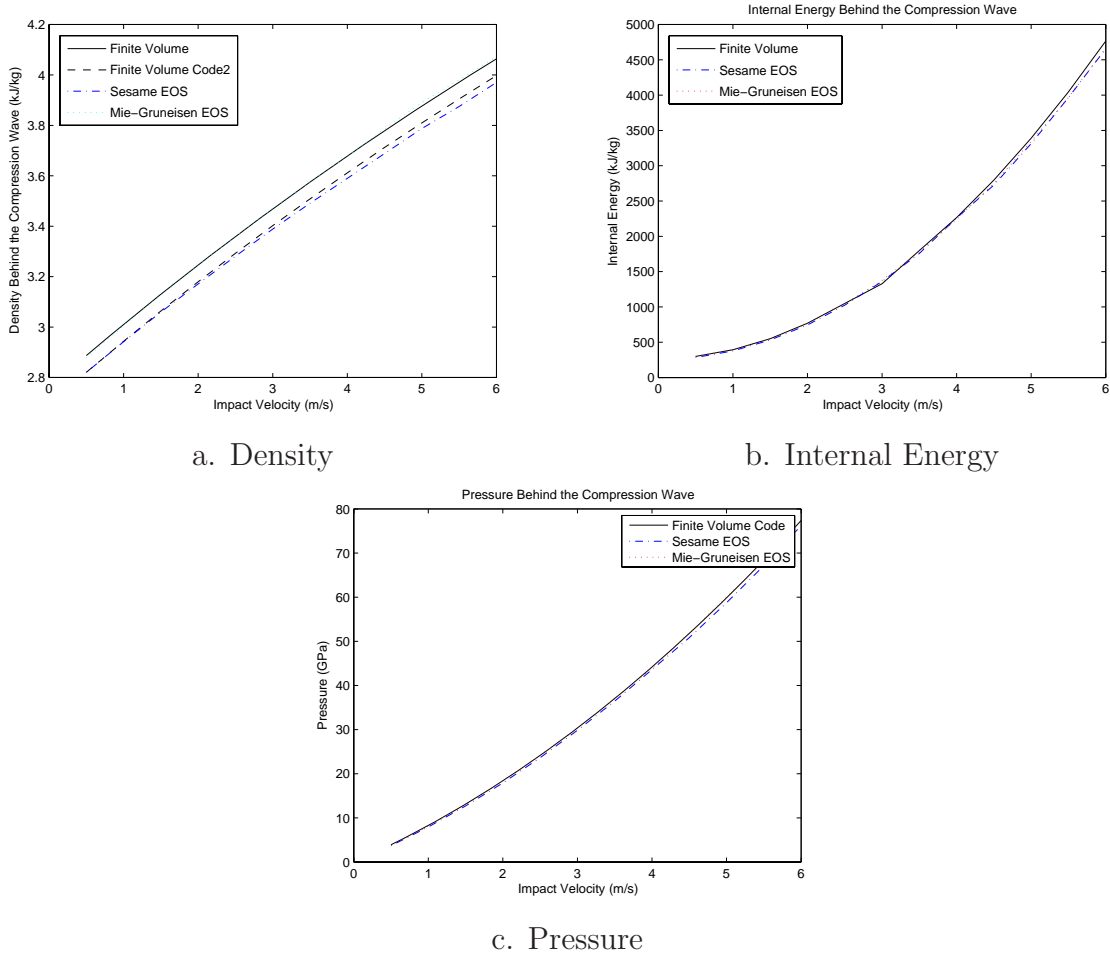
c. Pressure

Figure 4.1:   Comparison of Density, Internal Energy and Pressure generated by the Finite Volume Code and CTH

density values generated by the VFVC translated to the right for an easier comparison the densities generated with the VFVC and CTH, using the Sesame EOS, over the range of impact velocities. Upon examination of Figures 4.1a and 4.1c, it is apparent that the values of density, pressure and internal energy generated by the VFVC match the values produced by CTH quite well.

For a quantitative comparison of how the well the VFVC matches the thermodynamic values generated with the different EOS in CTH, Table 4.2 contains the standard deviations (SD) between the the results generated with the VFVC, Sesame EOS and Mie-Gruneisen EOS in CTH. The SD is a measure of variability representing the average difference of a sets of data from the mean of said data sets [11] making

84

it an ideal value in determining how the values generated by the VFVC and CTH compare. The SD in Table 4.2 of the densities and pressures generated, clearly shows that the VFVC and Mie-Gruneisen EOS match very well with the respective SD of 0.0068 kg/kJ and 0.1471 GPa. The SD of 40.257 kJ/kg for internal energy is also fairly small considering the the orders of magnitude for internal energy are 10^3 and 10^4. Table 4.2 also shows that the SD between the answers generated with the VFVC and CTH using the Sesame EOS are comparable to the ST between the answers generated using the Sesame and Mie-Gruneisen EOS in CTH. The values of the SD between the different data sets generated lead to the conclusion that when modeling a non-polymorphic material the thermodynamic variables generated by the VFVC compare quite well to the values generated by CTH.

Table 4.2: Comparison of the Standard Deviations Between the VFVC, Sesame EOS and Mie-Gruneisen EOS Generated Values

State Variable	SD of VFVC & Sesame EOS	SD of VFVC & Mie-Gruneisen EOS	STD of Sesame & Mie-Gruneisen EOS
Pressure (GPa)	0.3347	0.1471	0.3933
Density $\left(\frac{kg}{m^3}\right)$	0.0102	0.0068	0.0163
Internal $\left(\frac{kJ}{kg}\right)$ Energy	39.191	40.257	44.303

Figure 4.2 shows the different wave profiles generated for pressure at an impact velocity of 500 $\frac{m}{s}$ by CTH using both the Mie-Gruneisen EOS and the Sesame EOS, and the results generated by the VFVC. Upon inspection the firgure shows that the results generated by the VFVC behind the plastic wave are comparable to those generated by CTH. The graphs also show that the VFVC fails to generate an elastic precursor. This failure is caused by the 1st spatial order Lax-Friedrichs flux scheme, which overloads the discontinuity with dissipation causing the compression wave to spread itself out over several cells in the x-direction, thereby smearing out the elastic precursor. Even with the addition of the MUSCL scheme, which produces a 2nd order spatially accurate result is not enough to produce the elastic precursor. To remedy

this problem either a less dissipative 1st order flux scheme needs to be used, or a third order scheme needs to be introduced into the VFVC.

Overall several main observations are made about the similiarities and differences in the Mie-Gruneisen, PTRAN and Sesame EOS. This includes the similar pressures and internal energies generated by the different EOS, allowing them to be used in place of each other if the value of pressure or internal energy is of primary interest. This also signifies the form of the Mie-Gruneisen used in the VFVC will produce usable results. Also, both EOS are more sensitive to changes in density than to changes in pressure. It is also shown that the densities generated with each EOS are different in value, this may be corrected by using different Mie-Gruneisen EOS coefficients, this however, will affect the pressures produced by the Mie-Gruneisen EOS.

4.2   Validation of VFVC for Iron Impacts

4.2.1   Procedure.   The experimental geometries and impact velocities used in Section 3.2 are used in the validation of the Eulerian Code. In its current state the Eulerian code is only capable of handling one phase at a time, meaning it cannot accurately handle the phase change of iron. However the experimental data being used to validate the code only has two impact scenarios that cause the pressures generated to fall in the phase change region, and both of these impact velocities, 671.1 and 991.6 $\frac{m}{s}$, are located near the either beginning or the end of the phase change region. This proximity to these phase change boundaries allows the VFVC code to model these velocities scenarios as single phases, in this case, the α and ϵ phases respectively.

The material coefficients of both the α and ϵ phases used by the Mie-Gruneisen EOS are taken from Boucheron et al. and are located in Table 4.3. The VFVC utilizes a Fortran "if" statement to determine which coefficients to use. This determination uses the magnitude of the pressure generated by the impact. In order to allow the boundary impact scenarios to be modeled as single phases, the VFVC uses a pressure value to 15 GPa to differentiate between the two phases of iron. This is done instead

a. CTH with Mie-Gruneisen EOS   b. CTH with Sesame EOS

c. VFVC
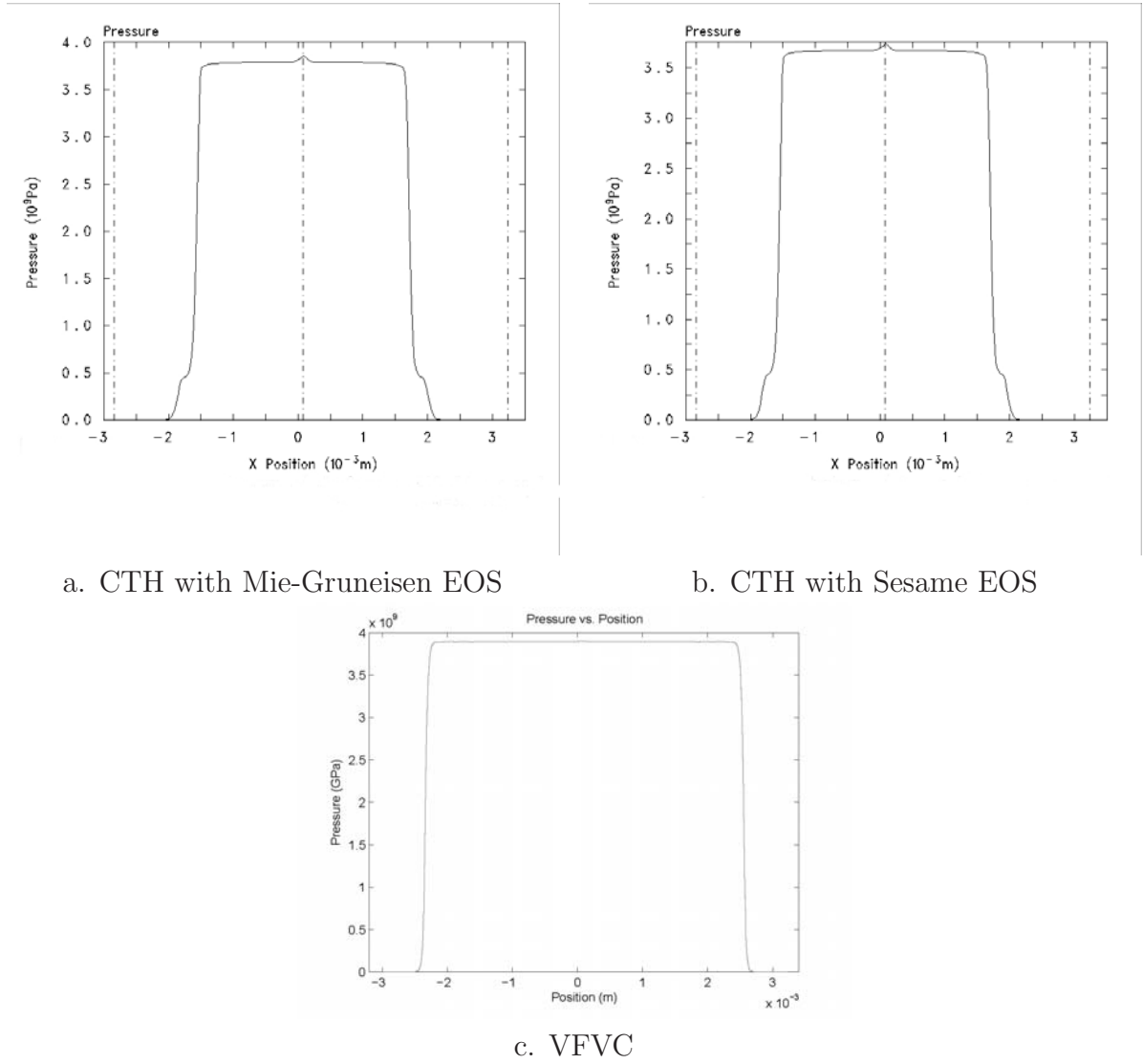
Figure 4.2:   Comparison of Pressure waves generated by the Finite Volume Code and CTH

Table 4.3:   Mie-Gruneisen Coefficients of the α and ϵ Phases of Iron

Coefficient	α	ϵ
C_0	4600 $\frac{m}{s}$	4600 $\frac{m}{s}$
ρ_0	7870 $\frac{g}{m^3}$	8290 $\frac{g}{m^3}$
S	1.46	1.51
Γ_0	1.7	2.4

of beginning the phase transition at a pressure of 13 GPa and completing it around a pressure of 17 GPa, as would be done in a code that can handle two phases.

Material coefficients are also required to describe iron's constitutive response to the impact phenomena. These coefficients are given in Table 4.4.

Table 4.4:   Additional Materials Parameters Needed by the Eulerian Code

Coefficient	Y	e_0	G	H
Value	50.0 MPa	131800 $\frac{J}{kg}$	87.0 GPa	2600 MPa
Source	[4]	[21]	[4]	Extrapolated from [32]

After all the experimental geometries and velocities are completed, the results generated by the VFVC are compared to the results numerically generated by CTH using both the PTRAN and Sesame EOS.

4.2.2   Validation of the Finite Volume Code with Impacts Between Iron Plates.
Figure 4.3 shows the thermodynamic variables of density, internal energy and pressure plotted against the impact velocities producing said thermodynamic variables. The densities generated by the different codes and EOS are located in Figure 4.3a. Upon study, this figure shows the densities generated by the VFVC more closely follow the CTH results produced with the Sesame EOS. This is contrary to the results seen in Section 4.1.2, Figure 4.1a in which the VFVC generated results follow the results produced in CTH using the Mie-Gruneisen EOS. This discrepancy is a result of the Mie-Gruneisen EOS coefficients, which were the same for the VFVC and CTH using the Mie-Gruneisen EOS for the simulation of aluminum impact scenarios. For iron, however, CTH's internal ϵ phase Mie-Gruneisen EOS coefficients are used in the

a. Density

b. Internal Energy
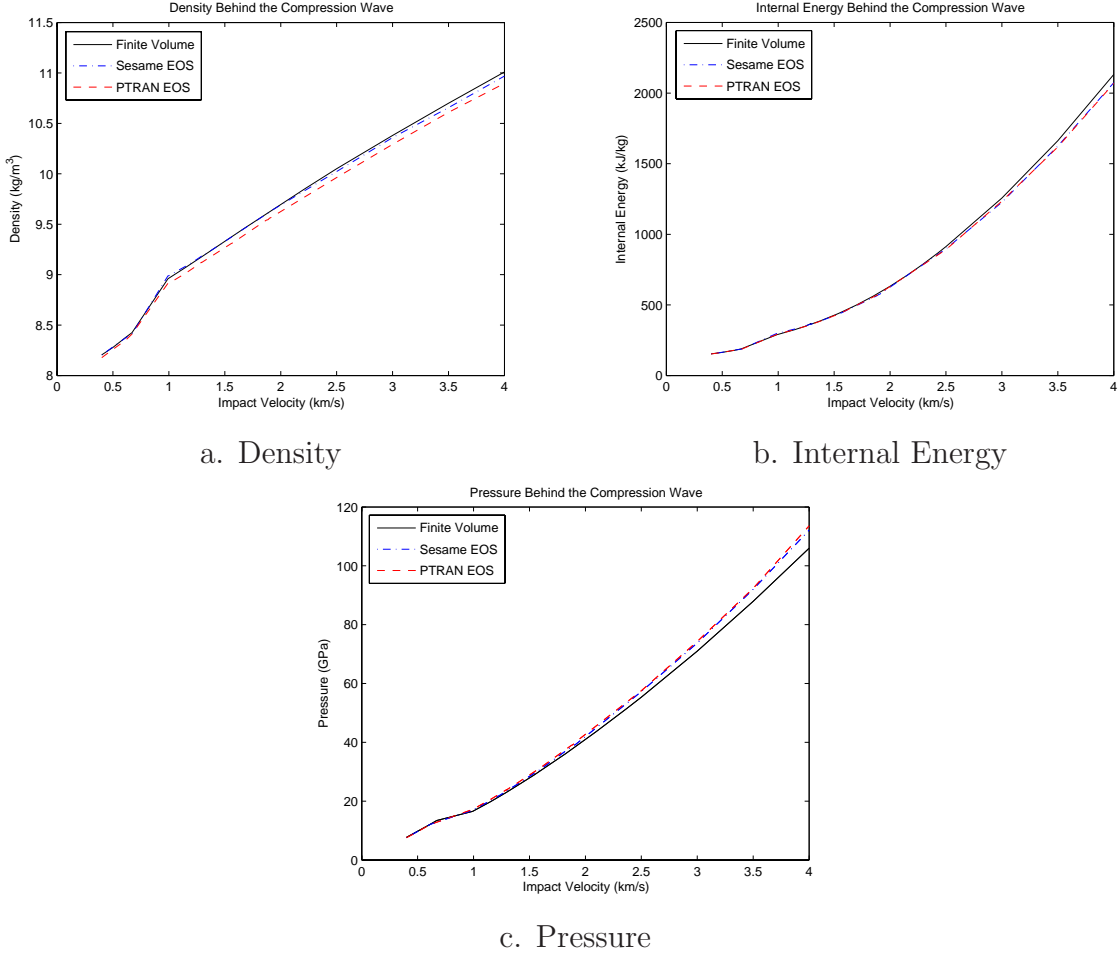
c. Pressure

Figure 4.3:   Comparison of Density, Internal Energy and Pressure generated by the Finite Volume Code and CTH

PTRAN EOS, while the VFVC requires the input of the ϵ Mie-Gruneisen coefficients. In the case of iron, the coefficients input into the VFVC happen to match match the material properties in the Sesame EOS better than they do for the PRTAN EOS. This discrepancy highlights the need for to validate the VFVC with analytical data, experimental data, or numerical data produced by a reliable hydrocode. Figure 4.3b shows the numerical values of internal energy generated by the different codes and EOS, once again are all quite similar. However in 4.3b it is apparent that at impact velocities grater than 2.5 $\frac{km}{s}$ the VFVC generates pressures significantly lower than those generated by CTH using both EOS.

Table 4.5 contains the SD comparing the numerical values produced by the VFVC, and CTH using the Sesame and PTRAN EOS. The SDs of 0.0210 and 0.0268 between the VFVC generated densities and those generated in CTH using the Sesame EOS and PTRAN EOS respectively, are less than one percent of the values of density being generated making this little difference acceptable. The SDs of the differences in internal energies generated between the VFVC and CTH using the Sesame and PTRAN EOS are 18.285 and 17.8018 $\frac{kJ}{kg}$ respectively. These values of SDs maintain percentages on the order of 10^1 for most of the internal energy values generated. As seen in Figure 4.3b it is at the higher impact velocities where the difference between the VFVC and the CTH generated values of internal energy have the greatest differences in value. So depending on the level of accuracy necessary, there exists an impact velocity that will serve as an upper limit for the applicability of the VFVC when modeling impact with iron, in the VFVC's present form. The need for this upper limit becomes quite evident when considering the SD for the values of the numerically generated pressures are 1.5303 and 1.7815 GPa for the difference between the VFVC and CTH values using the Sesame and PTRAN EOS respectively. These SD values are only an order of magnitude smaller than the values of the pressures produced for most of the range of impact velocities, which is a good percentage of the generated values. Looking at Figure 4.3b it is apparent that, similar to the internal energy results, the differences between the VFVC and CTH generated values occur at the higher impact velocities.

Table 4.5:   Comparison of the Standard Deviations Between the VFVC, Sesame EOS and Mie-Gruneisen EOS Generated Values

State Variable	SD of VFVC & Sesame EOS	SD of VFVC & PTRAN EOS	SD of Sesame & PTRAN EOS
Pressure (GPa)	1.5303	1.7815	0.3332
Density $\left(\frac{kg}{m^3}\right)$	0.0210	0.0268	0.0201
Internal $\left(\frac{kJ}{kg}\right)$ Energy	18.267	17.802	4.2016

To determine if the difference in pressure at the high velocities is a result of the Mie-Gruneisen coefficients used, or the codes inability to handle multiple phases, the CTH values for the α and ϵ Mie-Gruneisen coefficients for iron were used in the VFVC for impact velocities of 3500 $\frac{m}{s}$ and 4000 $\frac{m}{s}$. The answers generated are given in Table 4.6. From Table 4.6 it is apparent that the values generated by the VFVC with the Mie-Gruneisen EOS coefficients from CTH are 2.6% and 3.6% lower than the corresponding values generated by CTH for the impact velocities of 3500 and 4000 $\frac{m}{s}$. This indicates the differences in the pressures for generated by VFVC for the impact of iron is caused by its inability to handle multiple material phases, and not by the Mie-Gruneisen coefficients used.

Table 4.6: Comparison of Pressures Generated at Velocities of 3500 $\frac{m}{s}$ and 4000 $\frac{m}{s}$ by CTH using the Sesame and Mie-Gruneisen EOS and the VFVC Using the Mie-Gruneisen Coefficients from Table 4.3 and CTH

Impact Velocity	Sesame EOS	PTRAN EOS	VFVC Origional	VFVC w/CTH values
3500 $\frac{m}{s}$	92 GPa	92.4 GPa	87.9 GPa	89.6 GPa
4000 $\frac{m}{s}$	112.1 GPa	113.6 GPa	106 GPa	108 GPa

Figure 4.4 shows the wave profile resulting from an iron on iron impact with an impact velocity of 612.7 $\frac{m}{s}$ at a time of 1 μs. Again, the added dissipation from the Lax-Friedrich flux routine is smearing out the elastic precursor in the results generated by the VFVC in Figure 4.4c. In Figure 4.4b, the compression waves have reached the outside boundaries an have began to reflect as rarefaction waves. This is evident while looking at two things; the first, is the sharp cutoff of the elastic precursor at the boundaries, second, is the reduction in pressure at the upper "corners" of he compression wave. This lower pressure is due to the beginning of the rarefaction wave relieving the pressure caused by the impact.

Overall, the VFVC appears to give answers quite comparable to those generated by CTH, especially for a non-polymorphic material. The necessity of validating the initial results generated by the VFVC to determine if the proper values of Mie-Gruneisen coefficients are being used, has also been established. The VFVC code

a. CTH with PTRAN EOS

b. CTH with Sesame EOS

c. VFVC
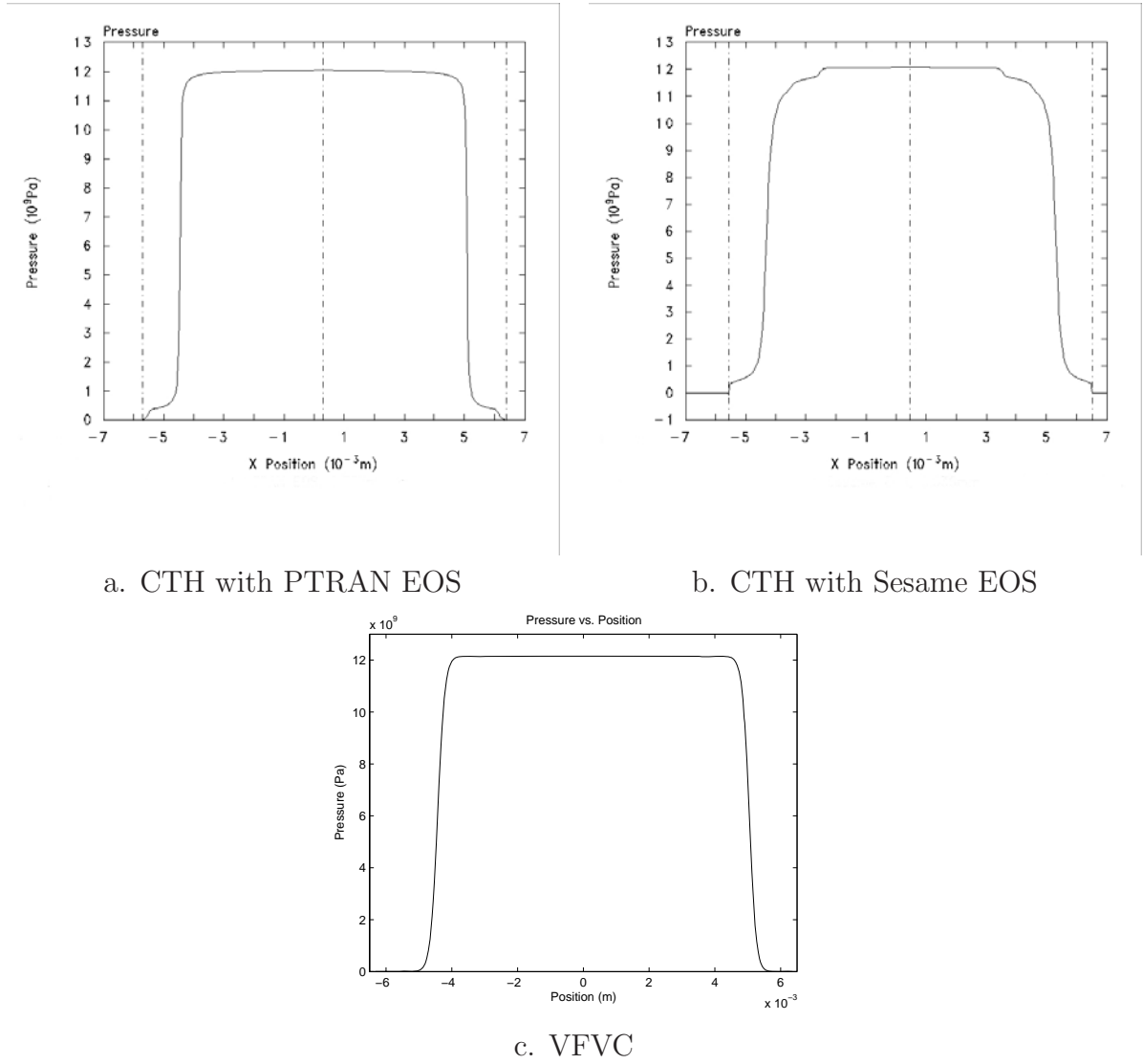
Figure 4.4:   Comparison of Pressure waves generated by the Finite Volume Code and CTH

92

will simulate impact with polymorphic material better if a subroutine capable of handling the phase transition is added. Another desired addition to the VFVC is an improvement to the flux routine.

V.   Comparison of CTH and NET Hydrocode

This part of the investigation consists of comparing the numerical results generated in by Lu and Hanagud in Reference [26] to the results generated by CTH using the Sesame and both PTRAN EOS. The impact scenario being modeled consists of an iron target 1 mm long with a stress load of 50 GPa applied on one side to initiate a stress wave.

In their simulations, Lu and Hanagud are incorporate a slip system into their grid using slip angles, ϕ, of 0° and 45° degrees. The slip system of 0° is parallel to the axis CTH uses when modeling uniaxial impacts, and thus is automatically accounted for by CTH. To introduce a slip system at an angle of 45° the plane strain mesh in Figure 5.1 is utilized. This mesh consists of a layer of PMMA inserted into the target material at a 45° angle. The rigid boundary layers located at the top and bottom of the mesh prohibit mass from flowing out of the mesh limiting any strain from occurring in the vertical direction, effectively creating a uniaxial strain scenario. The layer of PMMA acts as a dampener producing lower stresses in the back of the target than at the front. This requires a higher impact velocity to account for the dampening effect of the PMMA. In the plane strain mesh, each cell measures 0.002 mm by 0.002 mm, this is smaller than the 0.002 cm cell size suggested by Szmerekovsky [35], however it is used to match the cell size used by Lu and Hanagud. The 0.002 mm cell width is also used in the uniaxial case. Overall, the uniaxial mesh is 2 mm long with a 1 mm long target and a 1 mm long flyer plate. The length of the grid is 1000 cells long. The plane strain mesh shares the same overall horizontal dimensions as the uniaxial grid and is 0.2 mm tall, the overall mesh dimensions are 1000 cells in the horizontal direction by 100 cells in the vertical direction.

Lu and Hanagud apply stress to initialize their impact scenario, CTH however, requires a specified impact velocity. This requires the determination of the impact velocity needed to generate 50 GPa of pressure. To do this, the curves in Figure 3.14d are fit with a 6th degree polynomial, which is then used to solve for an initial impact velocity equal to 2255.0 $\frac{m}{s}$. A 6th degree polynomial is used because it came closest

to fitting the curve in the region of interest. This velocity initially produces a stress smaller than the requisite 50 GPa, in both the uniaxial and plane strain cases. To fix this the velocity is then increased incrementally until the correct impact velocities are determined. The final impact velocities are 2265.05 $\frac{m}{s}$ for the uniaxial case and 2280 $\frac{m}{s}$ for the plane strain case.

The 1 mm thick flyer plate is used to initiate the stress wave in the target. To avoid interference from wave reflections at the boundaries, a semi-infinite boundary condition is used at the far left and right boundaries.

CTH is used to reproduce Lu and Hanagud's results, using both the reversible and irreversible PTRAN and Sesame EOS, for the uniaxial and plane strain cases. The results generated by CTH are then compared to those generated by Lu and Hanagud.

5.1 Comparison of CTH to A NET Hydrocode

In this section, the results generated by Lu and Hanagud's NET code are compared to the results generated by CTH using the Sesame and both PTRAN EOS. Then, any similarities or differences between the results generated by the two hydrocodes results will be analyzed.

5.1.1 *Uniaxial Impact with $\sigma_0 = 50GPa$ and $\phi = 0°$.* The first set of results to be compared are the uniaxial impact results where $\sigma_0 = 50GPa$ and $\phi = 0°$. Figure 5.2 contains the CTH results using both PTRAN EOS and the Sesame EOS and the results generated by Lu and Hanagud. The times the wave profiles are captured
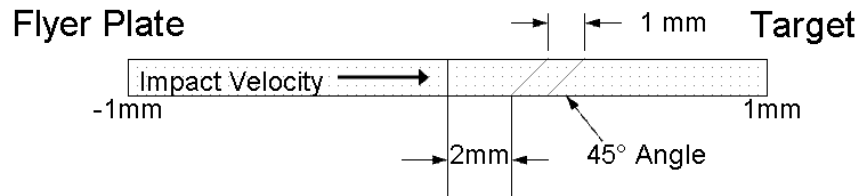
Figure 5.1:   Schematic of Mesh with 45 Degree Slip System

at are $1.1318 * 10^{-7}$, $1.1301 * 10^{-7}$, $1.13097 * 10^{-7}$ and $1.131 * 10^{-7}$ s for Lu and Hanagud's results and those generated by CTH using the Sesame and the reversible and irreversible PTRAN EOS, respectively. Lu and Hanagud use y as the horizontal axis variable, explaining the difference in notation in these results ang those presented for the plane strain case.

Examining the results contained in Figure 5.2, small differences in the results generated using Lu and Hanagud's code and those generated by CTH using the PTRAN and Sesame EOS may be ascertained. First the difference in the results generated using the different codes are presented. The most obvious difference in results generated by the two codes is the amount of dispersion error (oscillations) in Lu and Hanagud's results. This dispersion error is caused by the magnitude of the shockwave developed by their code and may be fixed by increasing the artificial viscosity used in their code. Another difference in the results generated by the two codes is the distance between the beginning of the elastic precursor and the beginning of the plastic wave, of which CTH has the larger distance. This is caused by the difference in plastic wave speed generated by the different codes, made apparent by the extra distance that the plastic wave has covered. The cause of the different plastic wave speed is most likely the use of different material parameters, such as the reference density (ρ_0) of ϵ iron, used by Lu and Hanagud compared to those contained in CTH. The different ϵ iron material properties have more of an effect than the α iron properties because, as is evident in Figure 5.2, the ϵ iron stress wave overtakes α iron wave due to the high value of the stress applied. The only similarity in the results generated by the different codes is the value of the equilibrium stress behind the compression wave.

The results generated by CTH using the different EOS are fairly close. The stress generated using both PTRAN EOS is slightly larger than 50 GPa, but not significantly.
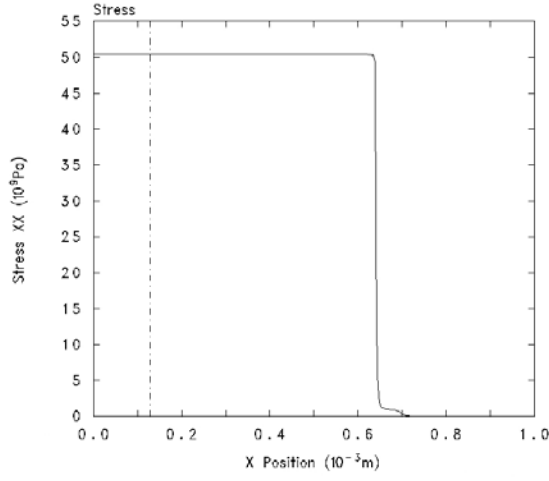
a. CTH with Reversible PTRAN EOS
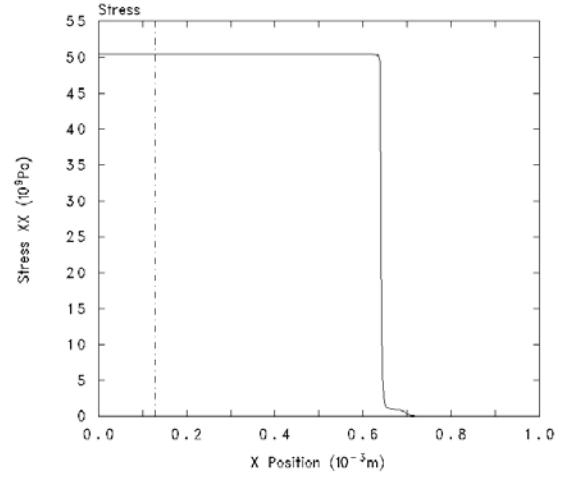
b. CTH with Irreversible PTRAN EOS
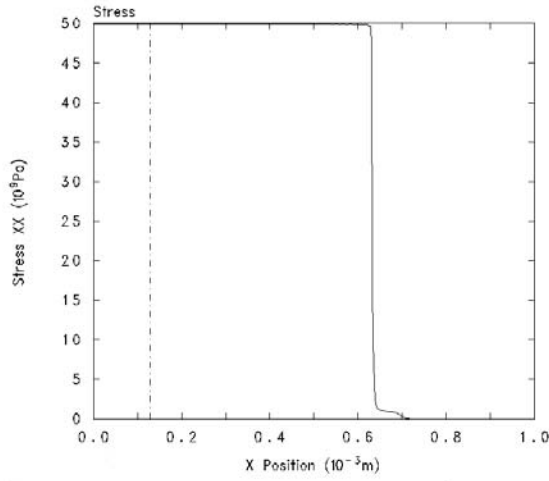
c. CTH with Sesame EOS
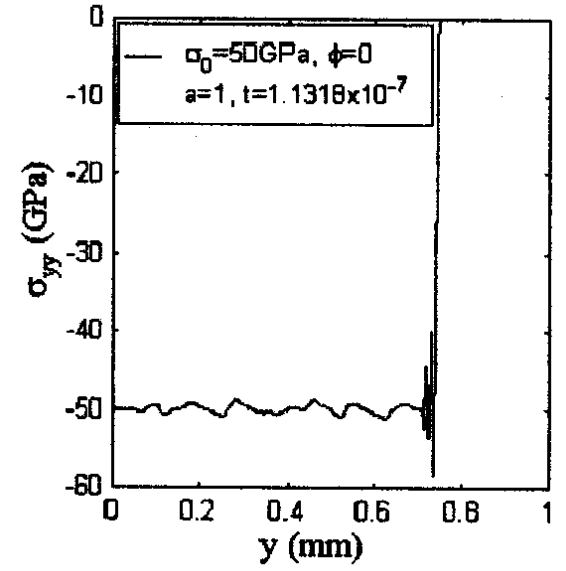
d. Lu and Hanagud

Figure 5.2:   Comparison of CTH and Lu and Hanagud's Results for $\sigma_0 = 50GPa$ and $\phi = 0°$ Uniaxial Impact

Unfortunately, not much can be ascertained from the results generated by the different hydrocodes that may be used in determination of the different codes respective abilities to handle NET.

5.1.2   Uniaxial Impact with $\sigma_0 = 50GPa$ and $\phi = 45°$.   The second set of results to compared are the for the plane strain case where $\sigma_0 = 50GPa$ and $\phi = 45°$. The wave reflections caused by inserting a layer of PMMA contribute to the generation of very busy wave profiles. This necessitate the CTH results be presenting using wave histories instead of profiles. A histogram created by placing a tracer point just behind the layer of PMMA presents the wave information in a manner in which the different waves generated may more easily be distinguished from each other. Figure 5.3 contains the CTH results using the Sesame and both PTRAN EOS and the results generated by Lu and Hanagud. Unlike the previous impact scenario, the stress waves generated in this case consist of two distinguishable waves. As Lu and Hanagud explain the initial wave is a elastic wave produced by the ϵ iron, a plastic wave then follows behind the elastic wave [26]. The different waves are labelled in the graph generated by Lu and Hanagud in Figure 5.3c.

The histograms produced by CTH show several waves. The first of these waves have a peak stress between 10 GPa and 15 GPa. This wave begins at the PMMA/iron boundary and propagates outward beginning at he time of impact. It is a result of the method used to create the 45° slip system in the CTH model, and is not a real solution, thus it can be ignored. The second wave corresponds to the elastic wave in Lu and Hanagud's results. The third wave is the plastic wave covered with oscillations.

The similarities in the compression waves generated using Lu and Hanagud's code and CTH include the production of separate elastic and plastic waves and the production a a 50 GPa equilibrium stress value behind the plastic wave. CTH's production of elastic and plastic waves validates the simulation of a slip system by inserting a layer of softer material in the PMMA at the desired slip angle. The production of multivalent equilibrium stresses behind the plastic waves is expected,
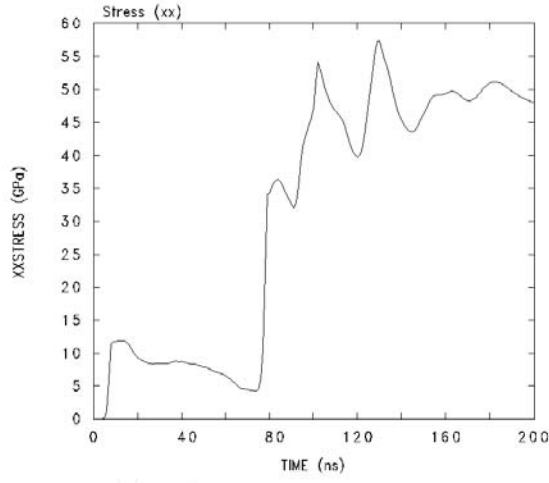
98

a. CTH with Reversible PTRAN EOS
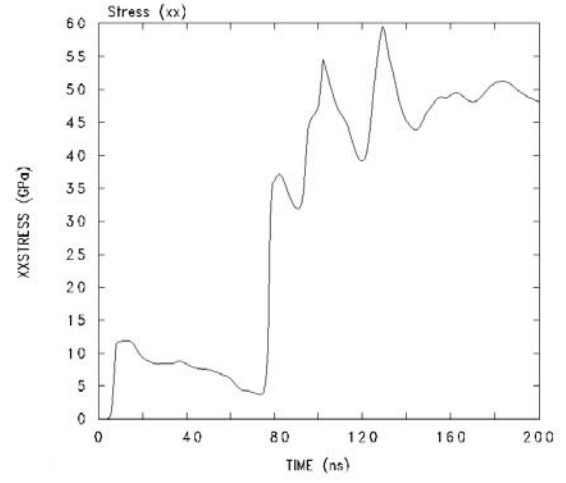
b. CTH with Irreversible PTRAN EOS
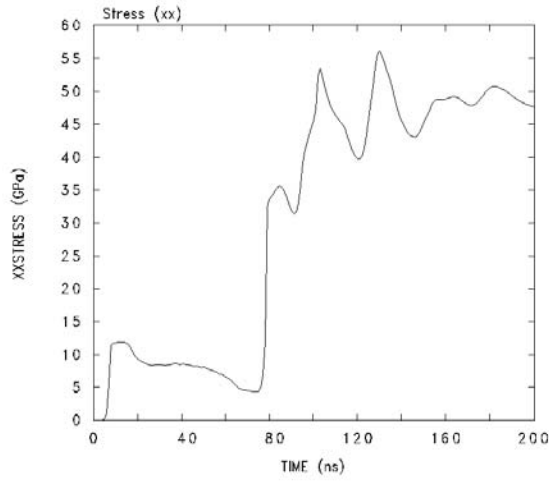
c. CTH with Sesame EOS
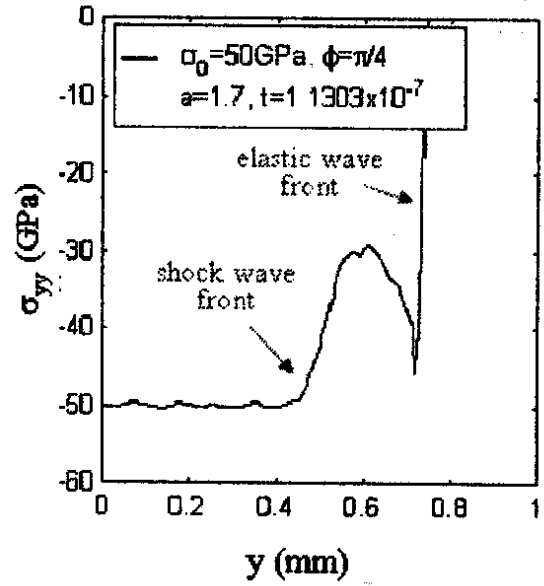
d. Lu and Hanagud

Figure 5.3:   Comparison of CTH and Lu and Hanagud's Results for $\sigma_0 = 50 GPa$ and $\phi = 45°$ Plane Strain Impact

99

because the equilibrium thermodynamics included in both codes should cause them to generate the same equilibrium value of stress.

Another similarity observable in Figures 5.3a and 5.3b are the stress wave histories produced using the Sesame and both PTRAN EOS. This indicates any ability CTH may have in modeling the NET of this scenario are not generated by the EOS and are most likely the product of CTH's ability apply constitutive relationships.

Several differences in the answers generated using the different codes are observed in Figure 5.3. These differences include the shape and magnitude of the elastic wave and oscillations evident in CTH's representation of the plastic wave. The large oscillations are likely caused by excessive interference from wave reflections resulting from inserting a layer of PMMA in the iron to produce the slip system.

Comparing the difference in magnitude and shape of the elastic wave allows for the comparison of the different hydrocodes' abilities to model the NET of an impact system. In Figure 5.3 the elastic wave in Lu and Hanagun's results reaches a peak stress of approximately 46 GPa before sharply relaxing to a stress of just under 30 GPa. This contrasts with the elastic wave generated by CTH peaking at a stress of approximately 37 GPa before relaxing to a stress of 30 GPa. Lu and Hanagud's hydrocode also has a faster relaxation time than seen in the CTH results, indicative of their code's ability to handle the non-equilibrium region immediately behind a shockwave where NET conditions abound.

The difference in peak stress value is a result of Lu and Hanaguds hydrocode to account for a non-equilibrium stress component as seen in Equation (2.93) shown here.

$$\sigma_{ij} = \sigma_{ij}^{e} + \sigma_{ij}^{ne}$$

In Equation (2.93) the total stress tensor is composed of an equilibrium stress and a non-equilibrium stress, $\sigma_{total} = \sigma_{eq} + \sigma_{neq}$. In this case, the 9 GPa difference in the peak stresses is produced by the non-equilibrium stress component, σ_{neq} included in Lu and Hanagud's hydrocode. This stress component is a found using the differential

equation given in Equation (2.89), shown here for convenience.

$$\tau_\nu(\sigma_{ij}^{\ddot{ne}}) = -\sigma_{ij}^{ne} + \eta_{ijkl} V_{kl}^e$$

that includes the strain rate, V_{kl}^e, and the relaxation time of the viscous processes, τ_ν [26]. These results suggest the Lu and Hanafud's hydrocode is capable of modeling system in non-equilibrium states.

While not accounting directly for τ_ν, CTH does use strain rate in the Zerilli-Armstrong constitutive relationship, allowing it to generate the first stress wave and to account for some relaxation of the material after the stress wave passes. This is shown in Figures 5.2a and 5.2b. This indicates, while CTH does not use the irreversible, non-equilibrium variables from the theories of IVT and EIT, it is still capable of accounting for the irreversible effects of material properties including stresses and strains. In addition, CTH is also able to account for the irreversibilities of phase changes.

VI. Conclusions

6.1   Conclusions

This work had three separate objectives. The first objective was to determine the similarities and differences between the tabular Sesame EOS, and the semi-empirical Mie-Gruneisen and PTRAN EOS. This objective provides guidance on the application of the EOS to impact scenarios using both CTH and the FVC. The second objective included validating the FVC by comparing its answers to those generated in CTH using the Sesame and Mie-Gruneisen EOS. This validation is a key step in the development of the FVC, which has the possibility being developed into a hydrocode capable of modeling non-equilibrium thermodynamics. The final objective involved comparing CTH results to those generated by a program capable of handling NET to determine CTH's ability to model NET.

Several conclusions were made in the comparison of the Sesame and Mie-Gruneisen EOS. The first and most important conclusion for the further production of the VFVC, stem from the similar values of internal energy and pressure generated by CTH using either the Sesame or Mie-Gruneisen and PTRAN EOS. These results lead to the conclusion the Mie-Gruneisen EOS produces the similar results to those generated by the Sesame EOS for the same impact velocities. However, the Mie-Gruneisen EOS cannot produce the same results as the Sesame EOS for any value of density, or at temperatures above the T_e in the Sesame EOS for the material being modeled. It was also shown that all the EOS are more sensitive to density then to temperature. Another finding is, the Sesame and Mie-Gruneisen EOS will produce different densities, while producing the similar pressures. This difference may be corrected by changing the Mie-Gruneisen coefficients used, however this will affect the pressures generated. This highlights the need to validate numerically generated answers using experimental data or analytical solutions, to assure generated values for a parameter of interest are correct. Finally, and most importantly in the determination of CTH's ability to model NET, the Sesame EOS is shown to generate irreversibilities in regions of phase changes.

The major conclusion stemming from the second objective is the validation of the FVC using the hydrocode CTH. The FVC produced values of pressure and internal energy similar to the numerical answers generated by CTH using the Sesame and Mie-Gruneisen EOS at the same impact velocities in a non-polymorphic material. For a polymorphic material, however, the pressures and internal energies generated by the FVC were considerably different at high speeds. This indicates the need to add a multi-phase capability to the FVC in order for the code to accurately model impacts involving polymorphic materials. The need for an flux routine that can accurately produce the HEL caused by impacts was also demonstrated.

In the comparison of results generated by CTH to those generated by Lu and Hanagud's NET hydrocode two conclusions were reached. The first, Lu and Hanagud's code is able to model a system outside an equilibrium state using irreversible, non-equilibrium thermodynamics from the taken from theories of IVT and EIT. The second, and maybe more significant, is CTH is able to account for some of the same irreversible parameters including stress, strain and strain rate contained in the constitutive relationship and the phase changes in polymorphic materials contained in the EOS.

6.2   Recommendations

In this investigation the ability of the Mie-Gruneisen and Sesame EOS to model uniaxial impact scenarios was investigated. There are more EOS to be investigated for the possible use in a hydrocode that can handle NET. Another investigation not addressed in this work, is to comparison of EOS for alloys instead of those for pure metals.

The study of NET is currently of great interest and is heavily reported on. To further determine CTH's ability to model NET, more comparisons should be made with the numerical results presented in journals and conferences.

Recommendations for the further development of the FVC include alterations to the flux schemes, validation of the FVC's constitutive model and adding an ability to handle multiple phases. For the flux scheme change it is recommended the Lax-Friedrich's flux scheme be abandoned, then using a different 1st order flux scheme. Another option is including higher order (3rd and 4th order) flux schemes, for example the 4th order essentially non-oscillatory (ENO) scheme detailed in Udaykumar et al. [38]. The constitutive model should be validated allow for accurate plastic flow results. This is a key step in the development of a code that can model NET, because the plastic deformation is a source of irreversible dissipation. Also, if impacts of polymorphic materials are going to be modeled, the code needs to be adopted to handle multi-phase materials.

Appendix A. Conversion of CFD Code into a Hydrocode

This Appendix contains portions of a document written describing the equations and procedure applied to an one dimensional CFD code intended to model the fluid dynamics in a shock tube for the purpose of transforming it into an one dimensional hydrocode capable of modeling uniaxial impacts. The document is intended to be a stand alone document with its own bibliography, albeit a small one. The document also assumes the reader is familiar with computational mechanics. However, after reading this thesis, it should not be difficult to understand.

Conversion of 1-D Shock Tube Code to a 1-D Hydrocode

I. Introduction

This paper describes the conversion of a 1-D Shock Tube CFD code into a 1-D Hydrocode capable of modeling the propagating waves caused by the impact of two metal bars of the same material. In addition to the conservation equations already contained in the shock tube code, constitutive equations accounting for the strength of the material will be included as well as a source term. In effect, the hyperbolic partial differential equation being solved is[2]:

$$\frac{\partial Q}{\partial t} + \frac{\partial F}{\partial x} = S(Q)$$

In addition to the constitutive equations and source terms, an equation of state will be utilized to relate the internal energy and density of the material to its pressure.

II. Theory and Equations

GOVERNING EQUATIONS

The governing equations used in the new code consist of the conservation laws of mass, momentum and energy (equations 1, 2 and 3), and constitutive equations that account for the strength of the material. Equation 4 accounts for the plastic stain seen by the material, while equation 5 accounts for the deviatoric, or shear stress seen by the material[2].

$$(1) \frac{\partial \rho}{\partial t} + \frac{\partial (\rho u)}{\partial x} = 0$$

$$(2) \frac{\partial (\rho u)}{\partial t} + \frac{\partial (\rho u^2 + p)}{\partial x} = \frac{\partial \tau_x}{\partial x}$$

$$(3) \frac{\partial (E)}{\partial t} + \frac{\partial u(E + p)}{\partial x} = \frac{\partial (u\tau_x)}{\partial x}$$

$$(4) \frac{\partial (\rho \bar{\varepsilon})}{\partial t} + \frac{\partial (\rho u \bar{\varepsilon})}{\partial x} = \left[\frac{1}{1 + \frac{\Sigma'}{3G}}\right] \frac{2\rho}{3} \left|\frac{\partial u}{\partial x}\right|$$

$$(5) \frac{\partial (\rho \tau_x)}{\partial t} + \frac{\partial (\rho u \tau_x)}{\partial x} = \left[1 - \frac{1}{1 + \frac{\Sigma'}{3G}}\right] \frac{4\rho}{3} G \frac{\partial u}{\partial x}$$

Though equation 4 is completely uncoupled from the rest of the governing equations, the strain experienced in an impact is of interest, thus explaining its inclusion in this assignment. The vector of conserved variables and the flux vector are determined from the governing equations and are[2]:

106

$$Q = \begin{bmatrix} \rho \\ \rho u \\ E \\ \rho \bar{\varepsilon} \\ \rho \tau_x \end{bmatrix} \qquad\qquad F = \begin{bmatrix} \rho u \\ \rho u^2 + p \\ u(E + p) \\ \rho u \bar{\varepsilon} \\ \rho u \tau_x \end{bmatrix}$$

EQUATIONS OF STATE

As previously mentioned the Mie-Gruneisen EOS is used to relate pressure to the internal energy (e) and the specific volume ($V = 1/\rho$). The form of the Mie-Gruneisen equation used in this code is[2]:

$$p(e,V) = \frac{c_0^2 (V_0 - V)}{[V_0 - s(V_0 - V)]^2} + \frac{\Gamma(V)}{V} \left[e - \frac{1}{2} \left(\frac{c_0 (V_0 - V)}{V_0 - s(V_0 - V)} \right)^2 \right]$$

Where in copper c_0 is the bulk speed of sound at zero pressure, s is the slope of the Hugoniot[1] and Γ is the Gruneisen parameter. As the waves flow through the materials Γ is dependent on the density of the material and is subject to the following relationship[2]:

$$\Gamma = V \left(\frac{\partial p}{\partial e} \right)_V = \frac{\Gamma_0 \rho_0}{\rho}$$

These parameters are also used to calculate the wave speed of the plastic wave moving through the material following the equation[2]:

$$U_P = c_0 + s u_p$$

where u_p denotes the particle velocity. To determine speed of the elastic wave, the following relationship is used[5]:

$$U_e = \sqrt{\frac{K + \frac{4G}{3}}{\rho}}$$

where K is the bulk modulus and is equal to[5]:

$$K = \rho c_0^2$$

When using the Mie-Gruneisen EOS, the speed of sound in the metal is found using the relationship[2]:

$$c^2 = \frac{\rho_0 \Gamma_0}{\rho^2} p + \rho_0 c_0 \frac{\rho + (s - \Gamma_0)(\rho - \rho_0)}{\left[\rho - s(\rho - \rho_0)\right]^3}$$

The value of the total Cauchy stress tensor produced by the elastic and plastic waves is determined with the realationship[2]:

$$\sigma_{ij} = \tau_{ij} + p\delta_{ij}$$

TIME INTEGRATION

In order to integrate the PDE in time, the it is rearranged to resemble[2]:

$$\frac{\partial \overline{Q}}{\partial t} = L(\overline{Q})$$

where

$$L(\overline{Q}) = -\frac{F_i - F_{i+1}}{\Delta x} + D(\overline{Q})$$

and D is the operator designating the source terms. The source term is added to the residuals before integrating through time.

Due to the small time steps made necessary by the high speed of sound in a metal, three different methods of time integration were utilized for this report, the Euler Explicit method used in the previously unaltered code and two Runge Kutta Schemes. The first Runge-Kutta scheme is a three stage, 3rd order TVD Runge-Kuttal Scheme, optimized by Shu and Osher[3] for handling ENO shock capturing schemes and applied by Udaykumar et al. to wave propagation through materials. Though an ENO scheme is not being utilized in this code, the decision was made to include it to determine if it has any advantage in solving this type of problem, thereby improving the numerical solutions generated. This Runge-Kutta scheme takes the following form:

$$u^{(1)} = u^{(0)} + \Delta t L\left(u^{(0)}\right)$$

$$u^{(2)} = \frac{3}{4}u^{(0)} + \frac{1}{4}u^{(1)} + \frac{1}{4}\Delta t L\left(u^{(1)}\right)$$

$$u^{(3)} = \frac{1}{3}u^{(0)} + \frac{2}{3}u^{(2)} + \frac{2}{3}\Delta t L\left(u^{(2)}\right)$$

A four stage, 4th order Runge-Kutta is also utilized[4]:

108

$$u^{(1)} = u^{(0)} + \frac{\Delta t}{2}\left(L^{(0)}\right)$$

$$u^{(2)} = u^{(0)} + \frac{\Delta t}{2}\left(L^{(1)}\right)$$

$$u^{(3)} = u^{(0)} + \Delta t\left(L^{(2)}\right)$$

$$u^{(n+1)} = u^{(0)} + \frac{\Delta t}{6}\left(L^{(0)} + 2L^{(1)} + 2L^{(2)} + L^{(3)}\right)$$

For 1st order spatial integration the Lax-Friedrichs routine in the previously existing code was utilized. In order to get second order spatial results the MUSCL scheme with Min Mod limiters is utilized[4].

III. Implementation

The following is a description of the code changes implemented how some data it stored. A detailed list of the code additions and alterations is located in Appendix A.

The implementation of the code consists of reading in and initializing the material properties of copper, updating the Q vector to handle the additional governing equations and material properties, updating the flux routine, incorporating the source terms into the right hand side module, incorporating the new Runge-Kutta time integration techniques into the solve module, and updating the output module.

The material properties are incorporated into to the input deck, along with a hydrodynamic operator, spatial integration designator and time integration technique designator. These designate the program to be either a pure hydrodynamic code or a code with the ability to handle elastic-plastic conditions in addition to specifying the spatial and time order of accuracy. A maximum time value is used to tell the program when to stop. The material properties, hydrodynamic operator and max time are read in inside the initial module and are stored in the runtime module. The initial module is also used to initialize the material properties and the initial velocities in the grid. In both the hydrodynamic and elastic-plastic settings the plastic strain and deviatoric stresses are initialized to zero.

In addition to the existing governing equations already contained in the Q vector (mass, momentum and energy), the plastic strain (PS) and the deviatoric stress (Sx) have been added. The values of the wave speeds and the total values of the Cauchy stress tensor are also carried in the Q vector for convenience, thought if computing time is an issue, these values may also be calculated at the end of the code. The definitions of the new Q vectors are contained in the constant module, and changes to the Q vector itself are located throughout the code.

The Lax-Friedrich flux routine is utilized to perform the spatial integration. Modifications to the Lax-Friedrichs subroutine include; adding the additional flux terms, implementing the Mie-Gruneisen Equation of state to solve for the pressure, and incorporating the speed of sound through the metal. Since the pressures and speed of sound for each cell is different, these values were treated as primitive values and

109

calculated each time for each cell every time step. For 2nd order spatial results the MUSCL subroutine with the Min-Mod limiter is utilized.

The source terms are included inside the RHS module, where an if statement is utilized to either set the source terms to zero for the hydrodynamic solver, or to use the previously derived source term values in the case of the elastic-plastic solver. The values for the individual cell velocities and deviatoric stress tensors, including the ghost cells, are calculated in an initial do loop and are stored in arrays. The gradients and source terms are then calculated in a separate do loop. At the end of the RHS module, the source term is added to the residual vector, the sum of which is then passed into the solve module where the time integration is performed.

The new Runge-Kutta integration techniques are incorporated into the solve module. Both integration techniques are coded in a series of successive stages since neither really allow themselves to utilize a repeated do loop. For this reason, a right hand side array is allocated to store the residuals for each stage, to be used specifically by the four stage Runge-Kutta. An allocated array is also used to store the original values of the Q vectors (designated Q old). The cells pressures, wave speeds, and total Cauchy stress values are also calculated in the solve module using the equations listed in the theory section of this report. As in the original code, the time step is calculated in each cell with the minimum cell time step designated the global time step. The calculation of the speed of sound used in the time step was updated to calculate the speed of sound for a wave moving through a metal. Then due to the high magnitude of the speed of sound through a metal, the global time stem is divided by 100.

The last major code changes include modifying the output module to output additional desired information to a data (.dat) file.

IV. Bibliography

1- Zukas, Jonas A., _Studies in Applied Mechanics 49 - Introduction to Hydrocodes_, Elsevier, 2004
2- Udaykumar, H. S., Tran, L., Belk, D. M., Vanden, K. J., _An Eulerian Mothod for Computation of Multimaterial Impact with ENO Shock-Capturing and Sharp Interfaces_, Journal of Computational Physics, v. 186 n. 1, p.136-177, 20 March 2003
3- Shu, C.-W., Osher, S., _Efficient Implementation of Essentially Non-Oscillatory shock Capturing Schemes_, Journal of Computational Physics 77, 1988, pg 439-471
4- Tannehill, J. C., Anderson, D. A., Pletcher, R. H., _Computational Fluid Mechanics and Heat Transfer 2nd Edition_, Taylor and Francis, 1997 pg 125
5- Zukas, Jonas A., _High Velocity Impact Dynamics_, Wiley, New York, 1990

Appendix B. CTH Input Deck

This Appendix contains the CTH Input deck used to model the impact of an iron target with a 45° slip system introduced. This is the input deck used to generated the results in Section 5.1.

```
*eor* genin

Flyer Plate Test With 45 Degree Slip System
control
  mmp
  ep
  vpsave
endcontrol

mesh
  block 1  geom=2dr    type=e   *  2dr is two dimensional rectangle plain strain

   x0=-0.1
     x1  n=1000  w=0.2  dxf=0.0002
   endx

   y0=-0.01
     y1  n=100  w=0.02 dyf=0.0002
   endy

  endb
endmesh

insertion of material

  block 1
    package projectile *define projectile
      material 1
      numsub 50
      xvel 2280e2       *  change only the first number, leave 'e2' this converts m/s to cm/s
      insert box
        p1 -0.1, -0.01
        p2 0, 0.01
      endinsert
    endpackage

   package target    * insert target
      material 2
      numsub 50
      insert box
        p1 0, -0.01
          p2  0.04, 0.01
      endinsert
```

```
                delete TRIANGLE
                P1 0.02, -0.01
                P2 0.04, -0.01.
                P3 0.04, 0.01
                ENDdelete
     endpackage
     package PMMA    * Insert Target
       material 3
       numsub 50
          INSERT PARALLELOGRAM
          P1 0.02, -0.01
          P2 0.04, 0.01
          P3 0.03, -0.01
          ENDINSERT
      endpackage
     package back
       material 2
       numsub 50
          insert TRIANGLE
                P1 0.03, -0.01
                P2 0.05, -0.01.
                P3 0.05, 0.01
                ENDinsert
          endpackage
     package back
       material 2
       numsub 50
       insert box
          p1 0.05, -0.01
          p2  0.1, 0.01
       endinsert
     endpackage

  endblock
endinsertion
```

```
edit
  block1
  expanded
  endblock
endedit

tracer              * add tracer points
  add 0.01 0
  add 0.035  0
  add 0.045 0
  add 0.05 0
  add 0.055 0
endt

eos
*  Information for materials
   MAT1 ses iron
   MAT2 ses iron
   MAT3 ses PMMA_RP
endeos

epdata
 mix 3
   matep 1 ZE iron
   matep 2 ZE iron
   matep 3 JO LEXAN
 vpsave
 lstrain
endep
```

```
**************************************************
*eor* cthin

Flyer Plate Test With 45 Degree Slip System
control
  mmp
  tstop = 2.0e-7     * you may need to increase the stop time to reach end of event
endc

Convct
 convection=1
 interface=high_resolution
endc

edit
  shortt
    tim 0.0,   dt = 1.0
  ends
  longt
    tim 0.0,   dt = 1.0
  endl
  plott
    tim 0.0   dt = 1.0e-8      * this sets the time step it plots profile data
  endp
  histt
   tim  0.0,   dt = 0.1e-8       * this sets the time step it plots history data
   htracer all
  endh
ende

boundary
  bhy
    bl 1
     bxb = 1 , bxt = 1   *semi-infinite boundaries at x max and min
     byb = 0,  byt = 0   *rigid boundaries at y max and min
    endb
  endh
endb

cellthermo
 mmp3               *  This was recommended by Eglin and appears
           *  to give good results as well.
 ntbad 5000000
endc
```

Appendix C. CTH Input Deck

This Appendix contains the spreadsheets used to generate the graphs for impact scenarios comparing the Mie-Gruneisen and Sesame EOS using aluminum, the comparison of the PTRAN and Sesame EOS using iron and the validation of the VFVC. The values contained in these spreadsheets were generated using both CTH and the VFVC.

a. Mie-Gruneisen EOS Generated Results

Impact m/s	Stress Gpa	Temp K	Density kg\m^3	Int Energy kJ/kg	Velocity m/s	Pressure Gpa	Strain 10^ -3
500	4.04167	332.188	2.8775	300.938	250	3.78571	21.0714
1000	8.41667	372.75	3.00658	395	500	8.16667	44.1667
1500	13.2857	425.625	3.12692	550	742.875	13	66.25
2000	18.5	497	3.245	765	1000	18.4	86.6667
2500	24.25	592.647	3.35938	1041.67	1250	24.125	104.167
3000	30.3125	718.782	3.47083	1377.78	1500	30.3125	127.5
3500	37.2727	878.125	3.575	1778.57	1750	37.0455	145
4000	43.8889	1079.17	3.67647	2240	2000	43.9474	158.929
4500	51.875	1322.22	3.78571	2750	2250	51.875	175
5000	60	1607.14	3.89091	3343.75	2500	60	178.571
5500	68.0952	1941.67	3.98095	3964.29	2750	68.0952	166.667
6000	77.7	2315.78	4.07292	4666.67	3000	77.5	151.866

b. Sesame EOS Generated Results

Impact m/s	Stress Gpa	Temp K	Density kg\m^3	Int Energy kJ/kg	Velocity m/s	Pressure Gpa	Strain 10^ -3
500	3.92308	332.233	2.82067	283	250	3.67857	21.1234
1000	8.17391	371.923	2.94211	376.25	500	7.92	44.16667
1500	12.8663	423.333	3.05962	531.944	760	12.6875	66.25
2000	18.2105	493.684	3.17105	745.238	1000	17.9	85
2500	23.75	587.5	3.28125	1025	1250	23.625	104.1667
3000	29.8438	709.091	3.38887	1361.2	1500	29.8438	122.5
3500	36.4583	864.706	3.49091	1757.07	1750	36.4583	138.235
4000	43.4783	1050	3.59	2260	2000	43.5938	157.143
4500	51.1111	1280	3.68824	2726.16	2250	50.8333	170.522
5000	58.75	1540	3.7875	3312.5	2500	58.75	181.25
5500	67.1429	1841.67	3.875	3964.29	2750	67.1429	183.75
6000	75.8333	2181.82	3.97037	4659.09	3000	76.25	157.83

c. VFVC Generated Results

Impact m/s	Stress Gpa	Temp K	Density kg\m^3	Int Energy kJ/kg	Velocity m/s	Pressure Gpa	Strain 10^ -3
500	3.922	n/a	2.887	299.6	249.9	3.898	3.001
1000	8.292	n/a	3.01	393.5	500	8.266	5.778
1500	13.12	n/a	3.13	549.4	750	13.1	8.384
2000	18.42	n/a	3.246	768.4	1000	18.39	10.84
2500	24.18	n/a	3.359	1049	1250	24.15	13.17
3000	30.4	n/a	3.469	1329	1500	30.37	15.35
3500	37.08	n/a	3.575	1798	1750	37.05	17.43
4000	44.23	n/a	3.678	2266	2000	44.2	19.5
4500	51.83	n/a	3.779	2797	2250	51.8	21.35
5000	59.91	n/a	3.876	3390	2500	59.78	23.12
5500	68.44	n/a	3.971	4045	2750	68.4	24.88
6000	77.43	n/a	4.064	4766	3000	77.38	26.47

Figure C.1:   Spreadsheets Generated Using Aluminum Impacts

a. PTRAN EOS Generated Results

Impact m/s	Stress Gpa	Temp K	Density kg\m^3	Int Energy kJ/kg	Velocity m/s	Pressure Gpa	Strain
400	7.8333	324.5	8.1775	152.717	200	7.579	0.021667
500	9.875	332.031	8.25882	164.063	250	9.625	0.0272
612.7	12.2	341.19	8.35	180	306.25	12.087	0.033
671.1	13.0909	344.25	8.41154	185.882	328.571	12.8182	0.0345
991.6	17.2727	391.667	8.9142	291.818	500	17.1591	0.075
997	17.3636	391.667	8.91176	292.727	500	17.2727	0.074546
1150	20.5263	421.333	9.01429	326.316	577.778	20.5263	0.082727
1247	22.75	440	9.08667	348.75	626.087	22.75	0.086316
1292	23.8158	452.005	9.12308	361.25	643.75	23.8158	0.088
1292	23.75	449.565	9.12	360.714	646.667	23.75	0.088261
1396	26.25	473	9.19286	390.278	700	26.25	0.091765
1557	30.3125	511.25	9.30769	440.625	776.923	30.3125	0.097619
1567	30.6667	517.105	9.31304	445.313	785.714	30.5	0.096739
1871	38.8636	623.143	9.54	565	940	38.8636	0.1075
1887	39.2	628.846	9.54545	570	945	39.2	0.109091
1900	39.7727	634.615	9.56	577.5	960	39.5455	0.102273
1908	40	638.462	9.56364	582.5	955	40	0.117273
2500	57.5	952.381	9.9625	891.67	1250	57.5	0.12778
3000	74.2857	1304.35	10.2917	1234.78	1500	74.2857	0.145588
3500	92.35294	1750	10.6094	1619.05	1750	92.35294	0.151389
4000	111.7241	2269.231	10.8971	2069.44	2000	113.6	0.134615

b. Sesame EOS Generated Results

Impact m/s	Stress Gpa	Temp K	Density kg\m^3	Int Energy kJ/kg	Velocity m/s	Pressure Gpa	Strain
400	7.88	325.395	8.2026	152.935	200	7.579	0.021786
500	9.875	333.167	8.28333	164.412	250	9.6875	0.0272
612.7	12.3636	343	8.3731	180.278	306.6738	12.09091	0.303
671.1	13.1818	336.667	8.41154	187.059	328.571	12.9091	0.035556
991.6	16.9	363.28	8.9871	299.091	495.24	16.8	0.090625
997	17.0476	363.077	8.9889	300	496.875	17.0476	0.091177
1150	20.05556	392.5	9.08333	329.412	575	20.14706	0.091667
1247	22.2619	415.714	9.14925	352.632	623.8095	22.25	0.091875
1292	23.2813	425	9.18333	364.474	640	23.4375	0.094118
1292	23.3021	423.077	9.17761	363.158	646.154	23.4211	0.091579
1396	25.8333	447.619	9.25385	391.667	700	25.8333	0.09375
1557	29.8214	485.882	9.37143	441.071	778.261	29.8333	0.095263
1567	30.19231	490.588	9.38	444.643	775	30	0.095238
1871	38.3333	583.929	9.6	560.526	936.842	38.3333	0.1
1887	38.6957	590	9.61111	566.667	938.889	38.6957	0.10087
1900	39.0476	598.214	9.62222	573.684	947.368	39.0476	0.101191
1908	39.3182	600	9.63	576.316	952.632	39.1667	0.101667
2500	57.222	897.368	10.0227	897.12	1250	57.222	0.125
3000	73.75	1208	10.3594	1227.27	1500	73.75	0.1417
3500	92.5	1590.91	10.6563	1625	1750	92	0.15333
4000	112.308	2018.52	10.9688	2073.529	2000	112.143	0.13875

c. VFVC Generated Results

Impact m/s	Stress Gpa	Temp K	Density kg\m^3	Int Energy kJ/kg	Velocity m/s	Pressure Gpa	Strain
400	7.733	n/a	8.205	153.4	200	7.683	0.0136
500	9.809	n/a	8278	163.6	250	9.75	0.01686
612.7	12.21	n/a	8378	179.3	306.4	12.14	0.02046
671.1	13.49	n/a	8425	188.7	335.6	13.42	0.0223
991.6	16.63	n/a	8.959	289.8	495.8	16.51	0.0506
997	16.73	n/a	8.963	290.9	498.5	16.615	0.05065
1150	19.9	n/a	9.072	325.4	575	19.78	0.05284
1247	22.05	n/a	9.143	350.5	623.5	21.93	0.05472
1292	23.07	n/a	9.176	367.7	646	22.95	0.5569
1292	23.07	n/a	9.176	362.8	646	22.95	0.05569
1396	25.51	n/a	9.2532	393.1	698	25.38	0.05795
1557	29.44	n/a	9.372	445.9	778.5	29.3	0.06134
1567	29.68	n/a	9.38	450	783.5	29.55	0.06212
1871	37.58	n/a	9.603	571.2	935.5	37.44	0.0676
1887	38.01	n/a	9.614	579.7	943.5	37.87	0.06785
1900	38.36	n/a	9.624	584.9	950	38.22	0.06811
1908	38.58	n/a	9.63	588.6	954	38.43	0.06824
2500	55.51	n/a	10.05	912.8	1250	55.33	0.08296
3000	71.19	n/a	10.38	1257	1500	71	0.09485
3500	88.12	n/a	10.7	1663	1750	87.91	0.106
4000	106.3	n/a	11.01	2132	2000	106	0.1165

Figure C.2:   Spreadsheets Generated Using Iron Impacts

118

Bibliography

1. Anderson, Jr., John D. *Modern Compressible Flow With Historical Perspective*. McGraw-Hill Higher Education, New York, NY, third edition, 2003.

2. Andrews, D.J. "Calculation of Mixed Phases in Continuum Mechanics". *Journal of Computational Physics*, 7:310–326, 1971.

3. Andrews, D.J. "Equation of State of the Alpha and Epsilon Phases of Iron". *Journal of Physics and Chemistry of Solids*, 34:825–840, 1973.

4. Automation Creations, Inc. "www.matweb.com", January 2007.

5. Barker, L.M. and R.E. Hollenback. "Shock Wave Study of the $\alpha \rightleftarrows \epsilon$ Phase Transition in Iron". *Journal of Applied Physics*, 45(11):4872–4887, 1974.

6. Benson, D.J. "Computational Methods in Lagrangian and Eulerian Hydrocodes". *Computer Methods in Applied Mechanics and Engineering*, 99:235–394, 1992.

7. Boucheron, E.A., BrownK.H., K.G. Budge, S.P. Burns, D.E. Carroll, S.K. Carroll, M.A. Christon, Drake R.R., C.G. Garasi, T.A. Haill, J.S. Peery, S.V. Petney, J. Robbins, A.C. Robinson, R. Summers, Voth T.E., and M.K. Wong. *ALEGRA: User Input and Physics Descriptions Version 4.2*. Technical Report SAND2002-2275, Sandia National Laboratories, Sandia National Laboratories, Albuquerque, NM, October 2002.

8. Callen, H.B. *Thermodynamics*. Wiley, New York, 1960.

9. Cinnamon, John D. *Analysis and Simulation of Hypervelocity Gouging Impacts*. Ph.D. dissertation, Graduate School of Engineering, Air Force Institute of Technology (AETC), Wright-Patterson AFB OH, June 2006. AFIT/DS/ENY/06-01.

10. Drumheller, D.S. *Introduction to Wave Propagation in Nonlinear Fluids and Solids*. Cambridge University Press, New York, NY, 1998.

11. of Educational Technology, San Deigo State University Dept. "Encycloprdia of Educational Technology @ http://coe.sdsu.edu/eet/", Febuary 2007. Http://coe.sdsu.edu/eet/.

12. Eugene A. Avallone, Editor and Theodore Bauneister III. *Mark's Standard Handbook for Mechanical Engineers*. McGraw-Hill, New York, NY, 10th edition, 1996.

13. Gasser, Robert P.H. and W. Graham Richards. *An Introduction to Statistical Thermodynamics*. World Scientific Publishing Co. Pte. Ltd., Singapore, 1995.

14. Ghatak, A.K. and L.S. Kothari. *An Introduction to Lattice Dynamics*. Addison-Wesley Publishing Company, Singapore, 1972.

15. Hertel, E.S., R. L. Bell, M. G. Elrick, A. V. Farnsworth, G. I. Kerley, J. M. McGlaun, S. V. Petney, S. A. Silling, P. A. Taylor, and L. Yarrington. "CTH: A

Software Family for Multi-Dimensional Shock Physics Analysid". *Proceedings of the 19th International Symposium on Shock Waves*. July 1993.

16. I.V., Belinskii and B.D. Khristoforov. "Attenuation of Impact-Induced Plane Shock Waves in Aluminum". *Journal of Applied Mechanics and Technical Physics*, 8(3):86–89, May 1967.

17. Johnson, G.R. and W.H. Cook. "Fracture Characteristics of Three Metals Subjected to Various Strains, Strain Rates, Temperatures and Presssures". *Engineering Fracture Mechanics*, 21(1):31–48, 1985.

18. Jou, D., J Casas-Vazquea, and G Lebon. "Extended Irreversible Thermodynamics". *Rep. Prog. Physics*, 51:1105–1179, 1988.

19. Jou, D., J Casas-Vazquea, and G Lebon. "Extended Irreversible Thermodynamics Revisited (1988-89)". *Rep. Prog. Physics*, 62:1035–1142, 1999.

20. Kerley, Gerald I. *Multiphase Equation of State for Iron*. Technical Report SAND93-0027, Sandia National Laboratories, Sandia National Laboratories, Albuquerque, NM, February 1993.

21. Kerley, G.I. "Theoretical Equation of State for Aluminum". *International Journal of Impact Engineering*, 5:441–449, 1987.

22. Kerley, G.I. and J.R. Asay. "The Response of Materials to Dynamic Loading". *International Journal of Impact Engineering*, 5:69–99, 1987.

23. Kerley, G.I., J.M. Hale, and G.A. Mansoori. "Molecular Based Study of Fluids". *American Chemical Society, Washington, DC*, 107–138.

24. Laird, David J. *The Investigation of Hypervelocity Gauging*. Ph.D. dissertation, Graduate School of Engineering, Air Force Institute of Technology (AETC), Wright-Patterson AFB OH, March 2002. AFIT/DS/ENY/02-01.

25. Liberman, D.A. "Self-Consistent Field Model for Condensed Matter". *Physical Review B*, 20(12):4981–4989, December 1979.

26. Lu, X. and S.V. Hanagud. "Dislocation-Based Plasticity for Impact Loading in Solids". *Accepted for publication in the AIAA Journal in 2007.*

27. Lu, X. and S.V. Hanagud. "Dislocation-Based Plasticity at High-Strain-Rates in Solids". *45th AIAA/ASME/ASCE/AHS/ASC Structures, Structural Dynamics and Materials Conference, AIAA 2004-1920.* Palm Springs, California, April 2004.

28. Maugin, G.A. and W Muschik. "Thermodynamics with Internal Variables Part I. General Concepts". *Journal of Non-Equilibrium Thermodynamics*, 19:217–249, 1994.

29. Meyers, M.A. *Dynamic Behavior of Materials*. Wiley, New York, 1994.

30. Palazotto, Anthony N. "Class Notes", October - March 2005. MECH 500 Fundamentals of Solid Mechanics and MECH 600 Elasticity.

31. Puchi-Cabrera, E.S., C. Villalobos-Guitierrea, and G Castro-Farinas. "On the Mechanical Threshold Stress of Aluminum: Effect of the Alloying Content". *Journal of Engineering Materials and Technology*, 123:155–161, April 2001.

32. Rittel, Daniel and Guruswami Ravichandran. "High-Strain-Rate Behavior of α-Iron Under Shear Dominamt Loading Conditions". *15th Technical Meeting DT-MAT, Metz 1-2 June 2004*.

33. Rosenberg, H.M. *The Solid State An Introduction to the Physics of Solids for Students of Physics, Materials Science, and Engineering.* Oxford University Press, New York, NY, 1993.

34. Staniszewski, Szymanik R., B. and and S. Wisniewski. *Thermodynamics of Non-Equilibrium Processes.* PWN-Polish Scientific Publishers, Warszawa, Poland, 1976.

35. Szmerekovsky, Andrew G. *The Physical Understanding of The Use of Coatings to Mitigate Hypervelocity Gouging Considering Real Test Sled Dimensions.* Ph.D. dissertation, Graduate School of Engineering, Air Force Institute of Technology (AETC), Wright-Patterson AFB OH, September 2004. AFIT/DS/ENY/04-06.

36. Tannehill, J.C., D.A. Anderson, and R.H. Pletcher. *Computational Fluid Mechanics and Heat Transfer.* Taylor and Francis, Philadelphia, PA, 2nd edition, 1997.

37. Trangenstein, J.A. and P Colella. "A Higher-Order Godunov Method for Modeling Finite Deformation in Elastic-Plastic Solids". *Communications on Pure and Applied Mathmatics*, 44:41–100, 1991.

38. Udaykumar, H.S., L. Tran, D.M. Belk, and K.J. Vanden. "An Eulerian method for Computation of Multimaterial Impacts with ENO Shock-Capturing and Sharp Imterfaces". *Journal of Computational Physics*, 186:136–177, 2003.

39. Vincenti, Walter G. and Jr. Charles H. Kruger. *Introduction to Physical Gas Dynamics.* Krieger Publishing Co., Malabar, FL, 2002.

40. Yasar, Mustafa. "Gas Detonation Forming Process and Modeling for Efficient Spring-Back Prediction". *Journal of Materials Processing Technology*, 105(1):270–279, 2004.

41. Zerilli, F.J. and R.W. Armstrong. "Dislocation-Mechanics-Based Constitutive Relations for Material Dynamics Calculations". *Journal of Applied Physics*, 61(5):1861–1825, March 1987.

42. Zharkov, V.N. and V.A. Kalinin. *Equations of State for Solids at High Pressures and Temperatures.* Technical report, Academy of Sciences of the USSR, 1968.

43. Zukas, Jonas A. *Introduction to Hydrocodes.* Elsevier Ltd., Oxford, UK, 2004.

REPORT DOCUMENTATION PAGE

1. REPORT DATE (DD–MM–YYYY)	2. REPORT TYPE	3. DATES COVERED (From — To)
22–03–2007	Master's Thesis	Sep 2005 – Mar 2007

4. TITLE AND SUBTITLE

Comparison of Thermodynamic Equilibrium and Non-Equilibrium Representation of Materials

5a. CONTRACT NUMBER

5b. GRANT NUMBER

5c. PROGRAM ELEMENT NUMBER

6. AUTHOR(S)

Vanderhyde, Michael J., Captain, USAF

5d. PROJECT NUMBER

5e. TASK NUMBER

5f. WORK UNIT NUMBER

7. PERFORMING ORGANIZATION NAME(S) AND ADDRESS(ES)

Air Force Institute of Technology
Graduate School of Engineering and Management
2950 Hobson Way
WPAFB OH 45433-7765

8. PERFORMING ORGANIZATION REPORT NUMBER

AFIT/GAE/ENY/07-M25

9. SPONSORING / MONITORING AGENCY NAME(S) AND ADDRESS(ES)

1. AFRL/MNAC
ATTN: Dr. Kirk Vanden
101 W. Eglin Blvd Eglin AFB, Florida 32542-6810 DSN:873-2686
2. Air Force Office of Scientific Research
ATTN: Dr. John Schmissuer -NA, 875 North Randolph Street
Suite 325, Room 3112 Arlington, VA 22203 COMM: 703-696-6962

10. SPONSOR/MONITOR'S ACRONYM(S)

11. SPONSOR/MONITOR'S REPORT NUMBER(S)

12. DISTRIBUTION / AVAILABILITY STATEMENT

Approval for public release; distribution is unlimited.

13. SUPPLEMENTARY NOTES

14. ABSTRACT

Hydrocodes are valuable tools in the modeling of shock wave propagation through solids due to high speed impact phenomena. CTH is a hydrocode built with the ability to use multiple EOSs, including the semi-emperical Mie-Gruneisen EOS and tabular Sesame EOS. Modeling high speed impacts necessitates modeling the non-equilibrium thermodynamic states caused by these impacts. A discussion of the non-equilibrium thermodynamics that may be applied to the region directly behind a shock wave is presented, including details of recent attempts to model non-equilibrium impact phenomena in solids. Also, in order to better determine the applicability of the Mie-Gruneisen EOS anbd the two state PTRAN EOS and the Sesame EOS in situations that include non-equilibrium thermodynamics, the high speed, uniaxial impacts between two iron bars are modeled in CTH. The differences between the Mie-Gruneisen EOS and the Sesame EOS are established. A finite volume uniaxial hydrocode is validated. Finally, CTH is shown to be able to model some irreversibilities occurring in impact phenomena.

15. SUBJECT TERMS

Equilibrium Thermodynamics. Non-Equilibrium Thermodynamics, Equation of State, Hydrocode, Shock wave

16. SECURITY CLASSIFICATION OF:			17. LIMITATION OF ABSTRACT	18. NUMBER OF PAGES	19a. NAME OF RESPONSIBLE PERSON
a. REPORT	b. ABSTRACT	c. THIS PAGE			Dr. Anthony N. Palazotto, (ENY)
U	U	U	UU	135	**19b. TELEPHONE NUMBER** (include area code) (937) 255–6565, ext 4599